Radiation Damage Assessment of Zircaloy and Stainless Steel Cladding materials based on Neutron Flux and Energy Deposition using both Computational Tools and Analytical Solution.

A Thesis Submitted to the Department of NUCLEAR ENGINEERING

COLLEGE OF BASIC AND APPLIED SCIENCES

UNIVERSITY OF GHANA

BY

(Samiru Alhassan, 10507887)

BSc (Kumasi), 2013

In Partial Fulfillment of the Requirements for the Degree of

MASTER OF PHILOSOPHY

In

NUCLEAR ENGINEERING

July 2016

DECLARATION

I hereby declare that with the exception of references to other people's work which have duly been acknowledged, this Thesis is the result of my own research work and no part of it has been presented for another degree in this University or elsewhere.

…… ……

SAMIRU ALHASSAN Date

(Candidate)

We hereby declare that the preparation of this project was supervised in accordance with the guidelines of the supervision of Thesis work laid down by the University of Ghana.

…… ……

Dr. K..A. Danso NANA (Prof.) A. AYENSU GYEABUO I

(PRINCIPAL SUPERVISOR) (CO-SUPERVISOR)

…..…….. ……

Date Date

ABSTRACT

The maintenance of the structural integrity of materials in the nuclear reactor is a crucial issue both in-service and out of service. The cladding which forms an integral part of the fuel assembly isolates and prevents the fuel from contaminating the coolant. Pure Zirconium alloys and Steels have extensive use in the nuclear industry including its usage as clad materials for both Pressurized Water Reactor and Boiling Water Reactor fuels. These materials possess good combination of properties such as low neutron absorption, creep behavior, stress-corrosion cracking resistance, reduced hydrogen uptake, reduced corrosion. However, these structural components are susceptible to defects when exposed to high heat, pressure and irradiation. In this regard, the research focused on the use of computational tools to assess the radiation damage on zircaloy and stainless steel clad materials. In this thesis, a modified Low Enriched Uranium core (LEU) input deck was created with focus on the determination of neutron parameters with the MCNP5 code for a typical MNSR operating at 34KW maximum power using Zircaloy-4 fuel clad. The neutron energy deposition and neutron flux (neutron parameters) were employed in the SRIM-TRIM code and analytical radiation model calculations respectively to ascertain the radiation damage. The MCNP5 results as obtained from running the LEU input deck from the Argonne National Laboratory (USA) registered an average energy of 9.871884MeV in all ten lattice rings. The average fast neutron flux representative of all 344 fuel rods gave 5.29667E+11ncm^{-2}s^{-1} while the average fast neutron flux in the ten lattice rings gave 7.46E+13n/cm^{2}.s. In the SRIM code, the target width was determined as about 2.81μm for neutron interaction and 40.9μm for the radiation interaction. The damage assessment in the TRIM code established Zircaloy-4 as the best cladding material as it recorded the least

number of vacancies sustained, least replacement collisions of 147 and recoiling energy of 0.09 whilst Eurofer-97 suffered the highest vacancies created with stainless steel type-308 experiencing the highest replacement collision. The analytical calculations of the radiation damage on Zircaloy-4 using both the Kinchin-Pease and Norgett-Robinson Torrens models was determined as recording displacement of 17 and 14 atoms from the lattice site after 10,000 collisions respectively for only 30 minutes of operation. The calculation of the radiation damage suggests that the zircaloy-4 clad material shows good resistance to defect formation and propagation hence the displacement per atom after a much longer operation time will still leave the clad intact.

DEDICATION

This research is dedicated to God Almighty the benevolent, the Compassionate, Most Gracious the Most Merciful who saw me through the entire course of this work.

ACKNOWLEDGEMENTS

I believe acknowledgments are in order, my first is to the Almighty Allah, Creator and Controller of the Universe for His Guidance and Protection.

I wish to express my sincerest appreciation to all whose support, tolerance and guidance made this study a stunning success. I am highly indebted to many especially:

My supervisors, Dr. K.A Danso and Nana (Prof.) Ayensu A. Gyeabour I for their stupendous and tremendous hard work, tolerance, words of motivation and advice, empathetic comments and guidance in the preparation of this thesis.

I also want to use this opportunity to thank Dr. Henry Cecil Odoi, the Reactor Manager at the Ghana Atomic Energy Commission (GAEC) for the tremendous support he offered me from the beginning to the end of this thesis work.

My sincere gratitude also goes to my Uncle Naa Yussif Mumuni and Mr. Mahama Zachariah, Mr. Abdul Rahman Usman and Mr. Yussif Nupaya for the overwhelming support, encouragement and guidance in this endeavor and my entire life. Allah reward you all abundantly.

My sincere gratitude and special thanks go to my parents and sisters, whose never ending prayers, encouragement and support helped me to accomplish my goals. I love you so much.

Finally, to all who contributed to this work directly or indirectly, no amount of words or money can explain my appreciation for the help you offered me. God richly bless you.

TABLE OF CONTENTS

LIST OF FIGURES

LIST OF TABLES

NOMENCLATURE

ACRONYM	DEFINITIONS
ACTI	Advanced Computational Technology Initiative
BCA	Binary Collision Approximation
BCC	Body Centered Cubic
CANDU	Canadian Deuterium Uranium reactor
CIAE	China Institute of Atomic Energy
DPA	Displacement per Atom
ENDF	Evaluated Nuclear Data File
FOM	Figure of Merit
HCP	Hexagonal Closed Packing
IAEA	International Atomic Energy Agency
KMC	Kinetic Monte Carlo method
LAMMPS	Large Atomic/Molecular Massively Parallel Simulation
LEU	Low Enriched Uranium
MCNP	Monte Carlo N- Particle
MD	Molecular Dynamics method
MNSR	Miniature Neutron Source Reactor
NRT	Norgett-Robinson Torrens
ORNL	Oak Ridge National Laboratory
PKA	Primary Knock-on Atom
SRIM	Stopping Range of Ions in Matter
TRIM	Transport of Ions in Matter

LIST OF SYMBOLS AND CONSTANTS

SYMBOLS	DEFINITIONS
a_B	Bohr radius
<a>	Burgers vector
Å	Angstrom
C_k	Transformation atom
c	Speed of light
dP	Differential probability
$\sigma_d(E_n)$	Displacement cross-section
σ_e	Elastic cross-section
E_d	Displacement energy
ΔE	Lost energy
$\overline{E_n}$	Neutron flux energy
K_{eff}	Effective criticality
m_e	Mass of electron
$\phi(E)$	Particle flux
$\phi(E_n)$	Flux of neutrons
σ_{pp}	Pair production cross-section

CHAPTER ONE: INTRODUCTION

1.1 Overview

This chapter contains the study background, the area under study, problem statement, relevance and justification of the research, the Aims and objectives, scope, general description of the fuel assembly, definitions of some terms that are relevant to the research work.

1.2 Study Background

Since the demonstration in 1942 of the ability to sustain a nuclear chain reaction, nuclear power has developed into a proven technology. This paved the way for the production of electricity by means of nuclear power plants. To have a nominal appreciation in nuclear power generation, it has to have low cost of production, suitable waste disposal mechanisms and non-proliferation of fuel for other purposes and at the same time maintain its long-standing safety and reliability records (IAEA, 2009). This greatly requires a massive change in its fuel cycle. It is not surprising the increase in demand for nuclear power dwells on various factors which includes the continuous improvement in living conditions, concerns over 'greenhouse' emissions caused by burning fossil fuels, increased population just to mention a few. These major achievements are challenged by irradiation of reactor components as well as exposure of human and environment to radiation doses.

Structural materials sustain damage due to irradiation from fission or fusion processes. High energy radiation such as α, β and γ rays as well as particles such as protons, neutrons and electrons with crystallite structures give rise to defects and imperfections ranging from

vacancies to ionization (Mansur, et al., 1997). The major damaging process is as a result of particle interaction with target nuclei of the material structure causing sputtering and displacement cascades pinning dislocation motions and thus leading to reduction in the materials resistance to indentation. Fast neutrons are regarded as the major source of radiation effects which cause atomic displacement which leads to creep, swelling and embrittlement. Additionally, precipitates (i.e. Cu and P) can be formed leading to precipitation hardening of the material (Hännien, 1990). The resultant of these processes are the irradiation embrittlement of the reactor components materials with the welds.

The maintenance of the integrity of structural materials in the nuclear power plant is a crucial issue both in-service and out of service. The emission of gamma rays together with other elements from the fission reaction processes causes interactions with structural materials. These radiations are absorbed in the form of heat energy. This induced energy causes the dislodgement of zirconium atoms from their lattice sites and then introducing defects to the crystal structure of zirconium cladding material. The subjection of high heat, pressure and irradiation to the cladding material leads to both elastic and plastic deformation. In this research, our focus is on the assessment of radiation induced damage on the zirconium and stainless steel cladding materials.

Zirconium metallurgy is very important to the nuclear industry. It is regarded as a proven structural material as it possess a combination of properties such as good resistance corrosion and capture of thermal (slow) neutrons (Douglass, 1971). Its application is found in both the PWR and BWR as cladding tubes which encases the uranium dioxide fuel pellets. The spacer grids are also made of either zircaloy or high nickel alloy Inconel. In

the CANDU reactor, the fuel-cladding tube, pressurized tubes, sometimes the calandria tubes are all fabricated with zirconium alloys.

Steel is widely known to be composed mainly of iron and carbon in the presence of other trace elements. These trace elements can be added deliberately to improve the property and behaviour of the steel. Stainless steels are steels with about 10 - 12 wt % of chromium in its structure. This gives the steel an enhanced property of high-resistance to corrosion. There are generally three categories of stainless steels namely; ferritic, austenitic and martensitic stainless steels. Stainless steels have a wide array of application in the nuclear industry. Stainless steels of the type 308 and EUROFER 97 are used mostly as cladding materials due to their superior properties in temperature and corrosion resistance (Robert, et al., 1996).

SRIM-TRIM simulation code which stands for stopping and range of ion in matter (SRIM) - transport of ion in matter (TRIM) are a compendium of softwares used in the calculation of energy losses and range of ions distribution in matter. TRIM is a Monte Carlo code embedded in the SRIM code responsible for the computation of the stopping range of ions (10 – 2GeV/amu) into matter. SRIM - TRIM code is used in the simulation of collisions between ions and target atoms. It is a widely used tool by both researchers and students for analyzing a number of parameters relevant to understanding atomistic behaviour during collision (Ziegler, et al., 2010).

1.3 Study Area

The fuel element is considered as the heart of a nuclear reactor. Energy released from fission is converted to thermal energy. This heat is transferred to the coolant that flows through the core. The fuel element is made of a rod containing nuclear materials, cladding, end caps, and spacing parts. Cladding isolates and prevents the fuel from contaminating the coolant. The end caps seal the fuel element and together with the spacing parts fix it in the required position (Olander, 1976). For the fuel element to meet design objectives, they must be able to withstand the power cycle. They therefore meet requirements like sufficient heat transfer, complete retention of fission products, high reactivity, safety under accident conditions and retention of material integrity (Stanislav, et al., 2004).

The Fuel component is constructed by inserting a stack of fissionable material such as UO_2 pellets into a length of cladding. Spring placed on pellet stack for mechanical stability in the plenum region. Zircaloy (Zry) caps welded on the ends of the tube.

The fuel rods encompass a firm framework made from steel and zirconium which has fixed grid supports that tightly grips the rods in their precise lattice positions.

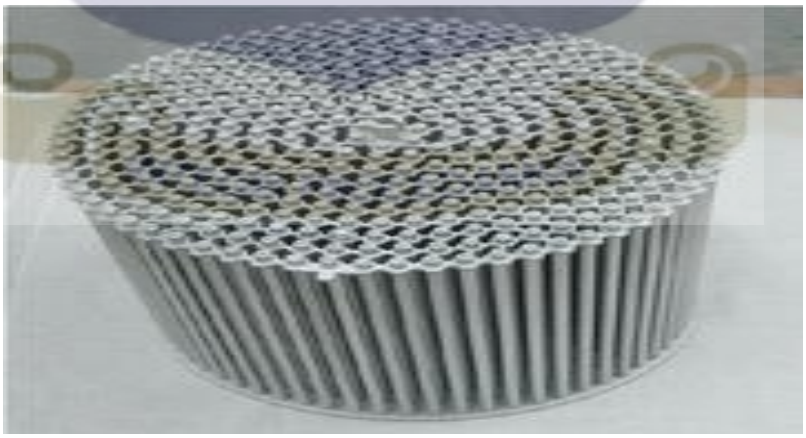

Figure 1.1: A representation of the fuel elements for LEU Core.

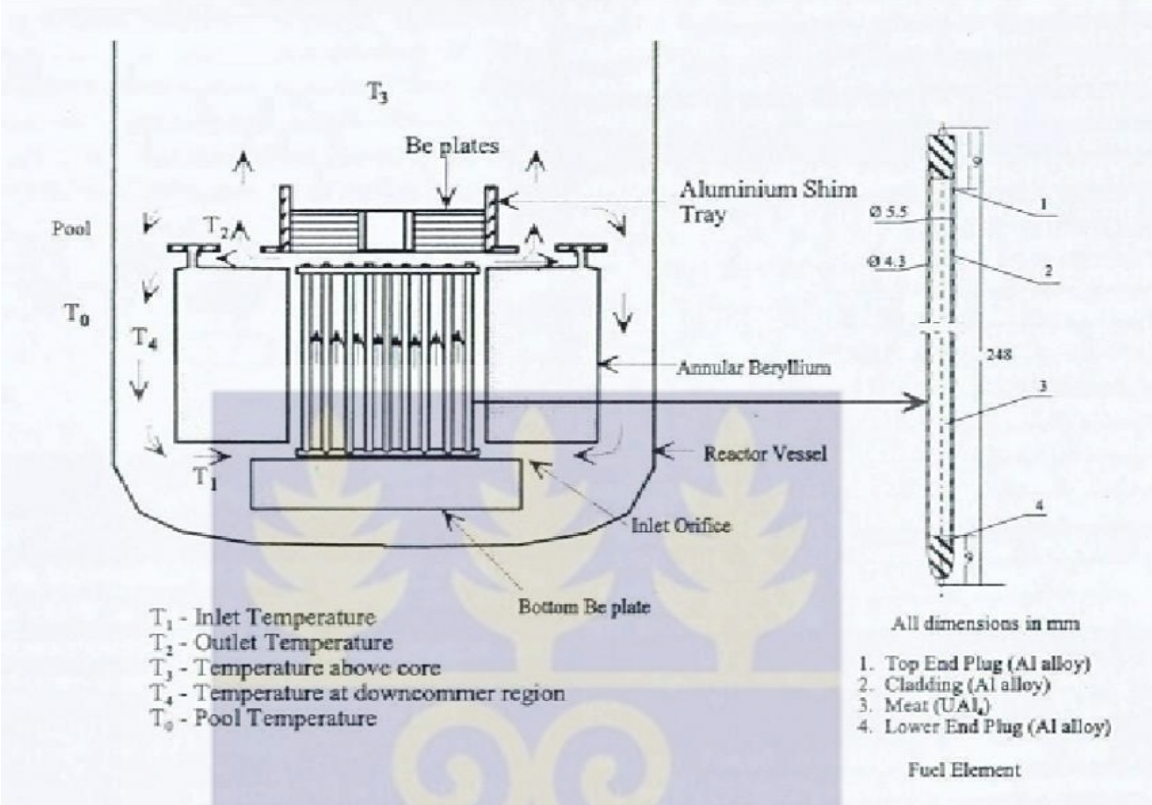

Figure1.2: A schematic view of the LEU fuel element assembly for the GHARR-1.

1.4 Problem Statement

Radiation damage of structural materials is of major concern to the nuclear industry. Structural components exposed to intense radiation from fission or fusion processes leads to radiation damage. The heat generated from this process is dissipated from the fuel to the clad and finally to the coolant by conduction, convection and radiation. Radiation accompanying energy emitted from the fission process induces atomic displacement in the cladding material there by introducing defects (Olander, 1976).

In-service, nuclear power reactor components are subjected to high heat and pressure, and bombardment by radiation. The combination of these stresses causes most of these components to deform elastically and permanently over time. For zirconium-based alloys,

thermal creep, irradiation creep and irradiation growth are the primary modes of deformation (Stanislav, et al., 2004). Creep collapse results in cladding due to unequal pressures from the coolant which is higher compared to the internal pressure between the Helium filled gap and the clad. Also embrittlement due radiation damage or accumulation of corrosion product thus hydrogen will result in a through -wall crack if a rapid power rise ensues.

In this research, emphasis will be given to the processes of formation and growth of radiation-induced defect in cladding material. The natural complexity of zircaloy cladding material which has both metal sub lattice and an oxygen sub lattice makes it much more challenging than in metals. This research will help us understand the radiation damage on zircaloy using the SRIM-TRIM simulation codes since this will help in the fabrication choice of a more suitable structural component as cladding material.

The threshold energy concept which demonstrates that particles of energy greater than a specified value produces damage whilst those below a particular threshold do not produce damage is a crude approximation. The use of Displacement per Atom (DPA) to represent material damage has demonstrated to be a more conservative approach to solving threshold value (McElroy, et al., 2004). Additionally, operational temperatures restores large number of DPA with just small fraction causing residual damage. Its cross-section is accurate for monoatomic crystals but not composites. Therefore, in-depth and precise data are required on structural properties of both fuel and clad material to establish the relevant engineering correlations.

1.5 Relevance and Justification

Structural components of the nuclear power plant need to keep their functional abilities so as to maintain the material integrity of the fuel assembly. This is to prevent the released radioactive substances of fission from getting to the coolant. Improved radiation resistant materials needs to be fabricated for harsher irradiation environments, higher temperatures and support higher burnups. This means the material should maintain integrity at higher Displacement Per Atom (DPA) thus the frequency with which atom are dislodged from their precise lattice site by atomic collision should not affect material property. Typically, Light Water Reactor (LWR) fuel clad, at burn-up of 40 GWd/tU experiences about 20 DPA (ANSI, 2007).

Advancement in technology which has evolved from the manufacture of civil nuclear power such as the magnox to Generation IV reactors and fusion reactors will require radiation resistant core structural components which can withstand imperfections or defects at higher atomic displacements. Expectations on next generation fast reactor systems would be to sustain atomic displacement reaching 150 – 200 DPA (Maisonnier, 2006).

Earlier studies on radiation damage have concentrated mostly on the energy causing this radiation damage. This thesis work however concentrates more on the fluence of this energy. This will in actual fact give a broader assessment of damage on the structural material over specified area and time. Also conversion of the fuel of the MNSR GHARR-1 from high to low enriched uranium with zircaloy cladding makes it an opportune time to assess the effect of the radiation damage on zircaloy. This could be an additional boost for regulatory approval.

Also advancement in reactor design and their core fabrication requires significant experimental and theoretical progress. This challenging advancement demands continuous, coordinated, synergetic efforts, with more intense research in the area of radiation damage of materials. Emphasis must be placed on the transmogrification of structural components at high temperatures and radiation exposures (ORNL, 2004).

There is therefore the need to study radiation damage effects on structural components as this will help in the developments of new techniques relevant to the fabrication of materials to meet the exigency of our time. It will also save cost as computational tool lessens the time and cost of experimentation.

1.6 Aims and Objectives

Principally, the aim of this thesis is to assess radiation damage on the zircaloy, stainless steel type 308 and EUROFER 97 cladding materials of the LEU fuel pins in a Miniature Neutron Source Reactor at 34KW power with Zircaloy cladding by the use of computer simulation program SRIM-TRIM code.

Specifically, this research is aimed at;

1. Understanding the irradiation-induced defects on structural components through simulation efforts.
2. Use Monte Carlo Simulation MCNP5 to generate the neutron parameters.
3. To compare the defects generated on the target materials Zircaloy 2 and 4, stainless steel 308 and EUROFER 97 using SRIM-TRIM code.
4. Determine the Projection range, Lateral and Longitudinal Straggling of the various clad materials using SRIM Code.

5. Compare the Collision Events, Sputtering, Ionization, vacancies generated and Replacement collisions of all four clad materials.

6. Determining the displacement per atom (dpa) due to radiation damage by both the Kinchin-Pease model and Norgett-Robinson Torrens model.

1.7 General Description of MNSR

The MNSR locally known as GHARR-1 is a typical research reactor with its maximum power at 30 kW. It is generally a tank-in-pool type. It has a relatively small size with very high levels of safety. It runs on highly enriched uranium (HEU) as fuel although there are proposals for the conversion of the core to low enriched uranium. Water serves as coolant and moderator, whilst beryllium shims serves as reflector (Nyarko and Debrah, 2012).

The reactor was fabricated and built by CIAE for the purposes of serving universities, hospitals and research institutes. The reactor is designed with maximum flux of $1x10^{12}$ $n/cm^2.s$ and a neutron source. It can boost of 10 irradiation sides; 5 inside and 5 outside the beryllium annulus reflector. This is why; it is precisely used for neutron activation analysis. It also serves the purposes of producing short-lived radioisotopes. However, it's used in training nuclear engineers, nuclear physicists, health physicists and radio-chemists (Quaye, 2012). The MNSR has a vessel which is a cylindrical Aluminium (Al) alloy LT – 21 and 0.6 m in diameter, 5.6 m in length and $9.5x10^{-3}$ m in thickness and a volume of 1.5 m^3. The vessel was built in 2 sections and submerged in a water pool which is protected by a reinforced concrete (Amuasi, et al., 2005). The lower and upper sections are held together by 16 stainless steel tie rods of diameter 0.019 m (Darko, 2013). The rods are 2.48 m long

and extend from the lower section flange to the square container support flange near the top of the upper section.

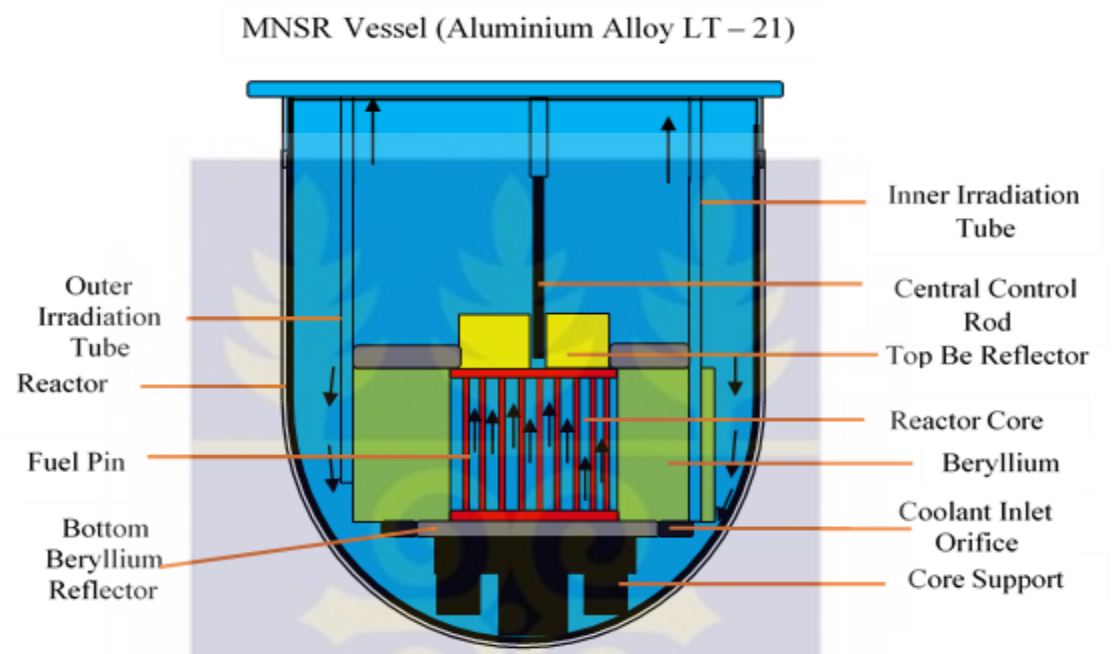

Figure 1.3: Pictorial View of GHARR - 1 Assembly.

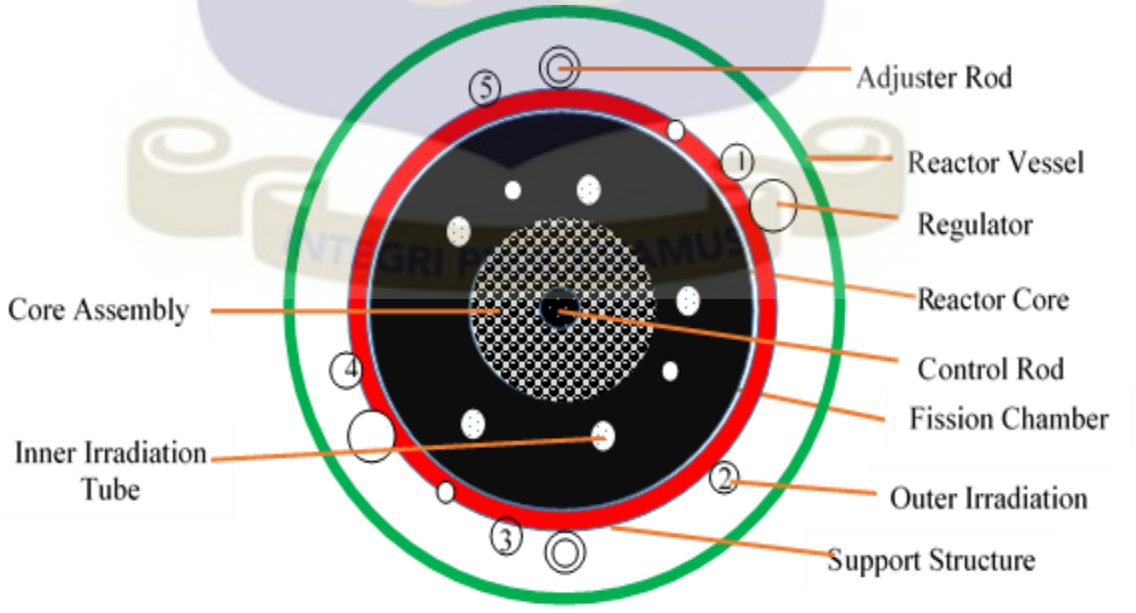

Figure 1.4: Cross Sectional View of GHARR - 1 Core.

Table 1.1 Specifications of GHARR - 1 (Akaho, 2003).

NO.	PARAMETER	DESCRIPTION
1.	Burn up / Cladding Material	~1% / Zr alloy
2.	Continuous operating time at rated power	2.5 hours
3.	Control Rod Absorber, Cladding	Cadmium, Stainless Steel
4.	Control Rod Length, Position	230 mm, Centre of Core
5.	Coolant / Moderator	Deionized H_2O and 995.1 kg/m^3
6.	Coolant Flow Rate	400 L/hr.
7.	Coolant Inlet Pressure and Temperature	101.3 KPa – 1 bar and 303 ^oK
8.	Coolant Temperature	(288 – 333) K
9.	Core Diameter / Core Height	230 mm / 230 mm
10.	Maximum Thermal Neutron Flux	$1.0x10^{12}$ n/cm^2s (rated power)
11.	Number of Control Element	1
12.	Number of Dummy Element	6
13.	Outer Irradiation sites	5 (2 large, 3 small)
14.	Prompt Neutron Lifetime (Λ)	$8.12x10^{-5}s$
15.	Rated Thermal Power / Core shape	34 kW / Cylindrical
16.	Effective delayed Neutron fraction (β_{eff})	$8.08x10^{-3}$ $(\Delta k/k)$
17.	Excess Reactivity – Cold, Clean	4 mk
18.	Fuel Composition	U dispersed in Zr
19.	Fuel Density	3.456 g/cm^3
20.	Fuel Element number in the Core	344
21.	Fuel Element Shape / Fuel Lattice Pitch	Thin rod / 10.95 mm
22.	Fuel Rod Position / Fuel Type	350 / Rod
23.	Inner Irradiation sites	5 (3 large, 2 small)
24.	Reactor cooling mode	Natural convection
25.	Reactor type / Reflector	Tank-in-pool / Beryllium
26.	Temperature coefficient	~ 0.10 $mk/$ ℃
27.	Total number of irradiation sites	10

1.8 Scope

The research work focused on modeling and simulation of radiation damage on cladding materials, specifically zircaloy material and stainless steel of type 308 and EUROFER 97.

The background to the study, area of study, problem statement, the relevance and justification of the study, the aims and objectives of the research are presented in Chapter one.

In chapter two, a review of literature on cladding used as structural components in the nuclear industry and also detailed information on radiation interaction with matter. This chapter throws more light on the mechanism of radiation damage as well, with its growth and propagation into cracks and eventually failure.

Chapter three focuses on the research methodology relevant to the application in radiation damage. Since this research is geared towards the use of computer simulation codes, we apply the codes MCNP5 purposely for neutron parameters (neutron flux and energy deposition) and generating trim.dat file for the TRIM code.

In chapter four, the results obtained from the MCNP5 and SRIM-TRIM code are simultaneously analyzed to ascertain the radiation damage caused by both neutrons and gamma. The assessment of the radiation damage on the cladding material will lead to the selection of the best suited clad material amongst the four cladding materials.

Chapter five will sum up all the finding from the results obtained in the research as provided in the previous chapter. This chapter will include the conclusion and recommendation for future works.

1.9 Definition

Creep: It occurs when a material plastically deforms to a subjected load /stress with respect to time.

Defect: A crystal structure has a defect when it exhibits any deviation in the regularity in the arrangement of atoms in their lattice structure. Depending on the dimension and degree of the defect they are categorized as;

Point defects: They are zero or dimensionless defects. They include; vacancies, interstitials

Line (Linear) defects: These are one dimensional defect. They form from a cluster of point defects close to each other. They include; screw and edge dislocations.

Planar (Surface) defects: They are two-dimensional defects. They are very common at the interfaces of homogeneous materials. They include; grain boundaries, etc.

Volume defects: These are three dimensional defects. They include voids, pores, and cracks.

Deformation: This refers to straining of a material. In elastic deformation, both shape and dimension of the material is maintained. For plastic deformation, there is a permanent change in shape or dimension.

Displacement: This refers to the removal of atom from its lattice site by an energetic incident atom.

Displacement Energy: It refers to the least energy required to displace a particle of atom about one atomic distance from its lattice position.

Displacement per Atom (dpa): This refers to the frequency at which a particle of atom is dislodged from its lattice or interstitial site.

Final Energy (E_{final}): This refers to the minimal amount of energy that brings an atom in motion to a stop. As atoms move, they cause ionization of other particles near-by. They lose energy in this process and eventually come to a stop when their energy is equal or below the final energy.

Interstitial Site: Any area other than the normal lattice site of an atom possible for accommodating an atom is an interstitial site. Any atom in this site is referred to as an interstitial atom.

Irradiation Creep: This refers to plastic deformation caused by the evolution of the varying defects induced by irradiation which is dependent upon their position relative to an applied load.

Irradiation Growth: This refers to a phenomenon in which the dislocation present in a lattice preferentially absorbs the defects causing the dislocation to climb in the absence of applied stress.

Interface Mixing: It refers to the transport of particles from one layer of the interacting ion to a target layer.

Ionization: This refers to the removable of an electron from an atom.

Lattice Binding Energy: This refers to the minimum energy needed to release a particle of an atom from its site.

Primary Knock-on Atom (PKA): It refers to the first target particle ejected from the lattice site by an incident particle.

Radiation Damage: This refers to the disruption of crystallographic nature of a solid structure when particles (ions) with energy traverses through them. This produces

microscopic defects in the crystal structure due to irradiation, by the interactions between incoming ion and target atom causing a Frenkel pairs.

Radiation Effect: Is the physical and mechanical property changes in materials induced by radiation.

Replacement Collision: This is when the incident ion takes the lattice site of the target atom after collision.

Recoil Implantation: This refers to when an incident ion is imbibed into a target atom for the purposes of modification.

Sputtering: Is the opposite of recoil implantation.

Sputtering yield: This refers to the average number of sputted atom per incoming ion.

Surface Binding Energy: This refers to the amount of energy that is needed by an atom in order to escape the surface of the target material. It is different from binding energy as it considers surface roughness etc.

Vacancy: This refers to the vacant site when an atom is ejected from a crystal lattice.

CHAPTER TWO: LITERATURE REVIEW

2.1 Nuclear Cladding Material

Undoubtedly, one of the most extensive and substantial constituent of the fuel rod composition is the all-important cladding tube. The cladding tube prevents the nuclear fuel from making direct contact with the coolant material inside the reactor vessel responsible for the transport of energy in the form of heat. Radioactive isotopes that accompany fission products would have the potential to not only contaminate many different systems throughout the primary loop, but also to be released into the neighboring environment.

The fuel clad acts as the layer of protection around the fuel pin from irradiation, corrosion. It also prevent fuel material from getting throughout to the reactor coolant circuit. This is achieved not only because it serves the purpose of trapping long-lived fission products, but the sealed cladding tubes also contains dangerous gases produced during reactor operations, such as Krypton and Xenon (Barrett, 2012). The existence of these gases in the fuel element coalesces and results in fuel swelling. Cladding therefore provides a great deal of protection in reducing the amount of radioactivity that is released into the primary coolant cycle during operation.

On the contrary, if the design of the cladding tube fails to meet the adequate requirements, there would be a drastic reduction in the amount of heat transferred from the pellets to the coolant material.

2.1.1 Properties of Cladding Material

The material property for a cladding element includes;

- **Low Thermal Neutron Absorption Cross Section:** For every fission process, about 2.5 neutrons are produced to sustain the fission chain reaction. The prompt neutrons are produced instantaneous whilst precursors undergo beta decay to

daughter nuclide which gives off delay neutrons. The cladding material should exhibit low tendency to absorbing neutrons. Zirconium, the current cladding material, has a neutron absorption cross section of 0.18 barns when compared to nickel (4.5 barns) and iron (2.4 barns) (KAERI, 2013).

- **High Thermal Conductivity**

The cladding material must demonstrate the ability to transfer high energy to the coolant to prevent accumulation and subsequent burn-out or melt down. This should be done effectively from the uranium pellet to the primary loop. Zirconium has a thermal conductivity of approximately 22.6 W/m*K (Tritt, 2004).

- **Radiation Resilience**

Nuclear fission products released from fission travel into the cladding (NRC, 2013). These particles do not only displace lattice atoms from the crystal structure but they also activate nearby atoms due to the released energy.

- **Corrosion Resistance**

The material should be capable of creating an inert oxide layer, by a mechanism known as passivation, which protects against corrosion. The zirconium and iron metals possess this quality. The exposure of the cladding material to a large volume of highly volatile water over an extended period of time makes it prone to corrosion. Cladding materials have to have good corrosion resistance. At normal operating reactor temperature (300° C), Zircaloy is an exceptional cladding and is considered to be the standard for fuel rods since the early 1950's (Todreas and Kazimi, 2011). This is usually the operation temperatures of Light or pressurized water reactors.

Table 2.1 Material behavior of reactor at rising temperatures (Ragheb, 2013).

Physical Phenomenon	**Temperature[^{o}C]**
Mean clad temperature during operations	350
Pressure buildup causes clad perforation or swell in volume	800 – 1,450
Release of fission gases thus I, Kr	
Start of chemical reaction between stainless steel and Zircaloy	
Coolant flow could be disrupted by clad ballooning	
Steam reacts with Zircaloy clad producing hydrogen and release of energy higher than the decay heat	1,450 – 1,500
Embrittlement of Zircaloy as a result of oxidation.	
Melting of Steel alloy	
Autocatalytic reaction of Zircaloy and steam occurs, this reaction could only be quenched upon immersing zircaloy in the coolant.	1,550 – 1,650
Melting of Zircaloy	1,900
The release of fission products becomes apparent above temperatures of 2,150 K.	
Melting of Uranium oxide and Zirconium	2,700

Temperature inevitably contributes significantly to the maintenance of the material integrity of the fuel rods. Between 1,450 – 1500 ^{o}C, the steam begins to react with the Zircaloy cladding. The oxidation process begins to produce zirconium hydride which forms region of radiation embrittlement, crack growth and propagation.

2.1.2 Zirconium Metal

Zirconium metal is significantly key in the production of electricity through nuclear power. This metal was first discovered in 1789 by renowned chemist Martin Heinrich Klaproth while studying the makeup of the mineral jargon ($ZrSiO_4$) within a jacinth stone from Sri Lanka (Sepke, H. and Sepke, I., 1986). Early chemists were uninterested in studying the jacinth stone very carefully as most believed that it was another form of aluminum oxide alumina. Klaproth analyzed the mineral jargon by heating it in the presence of a highly reactive compound, sodium hydroxide. It then formed an unknown oxide that turned out to be zirconium oxide. It was named Zirconium from the Arabic word zargun meaning "gold color" (Hoppe, et al., 1987).

For the next three and half decades, the struggle to produce the pure state of the metal continued till a Swedish chemist Jöns Jacob Berzelius a founding father of modern chemistry, succeeds in having a chemical reaction between potassium and potassium zirconium fluoride by 1824 (Binnewies, et al., 2013). This only yielded a black powder of about 93 percent zirconium which was not pure enough to be turned into a pure metal for material characterization of its properties.

It was until 1925 when Anton Eduard van Arkel, Jan Hendrik de Boer, and Phillips Gloei-Lampenfabriken invented the decomposition process for iodine, referred to as the Bar Process. This process was used by researcher to test the material properties of zirconium. The production of zirconium metal was on a small scale and in limited quantities in 1945. This made it very expensive (Krebs, 1998). On-going research on the material characterization then revealed the obvious desirable material properties like good resistance to rust, high melting temperature, and high ultimate tensile strength. This then

boosted the interest to produce zirconium on a large scale. The break-through for commercial production of zirconium metal was after the invention of magnesium reduction method in 1937 (Kroll, 1940). The large scale production of zirconium combined with its desired properties encouraged the wide use of the metal in different fields and industries.

In 1940 during the Manhattan Project, several groups of engineers and scientists exploring different metals and alloys for their application in the nuclear industry particularly for reactor fabrication and design, these scholars came to the realization that the desired properties of the zirconium metal met all the requirements for fuel cladding applications. The concern however, was that early research studies had shown a very strong thermal neutron cross section. This was proven wrong by Dr. Sam Utermeyer and Dr. Albert R. Kaufman of Massachusetts Institute of Technology. They discovered that early research work and measurements taken on the cross section for zirconium with regards to thermal neutron were wrong. This was because the hafnium content which occurred naturally with zirconium in zircon gave it the high neutron absorption cross-section (Weinberg, 1994).

2.1.2.1 Material Properties of Zirconium

At STP, pure Zirconium solidifies out as α phase for the hexagonal close packed (HCP) crystal structure (SSMC, 1989). A study of the phase diagram of zirconium shows that at temperatures of about 288^{o}C, it stays in the α phase. The crystallographic structure for the α phase are reported as; a = 3.2312 Å and c = 5.1477 Å.

The β phase of zirconium is BCC, but starts to develop at the grain boundaries of the α phase crystals as the temperature goes above 866°C (INSC, 1997). The β phase of the crystallographic structure for the zirconium is a = 3.6090 Å (O'Donnell, 1994).

Zirconium exists in its pure form as a glossy, grayish white, ductile metal. It is soft with desirable material properties such as low capture of neutron, high resistance to chemical oxidation.

The need for improvement in the performance of zirconium alloys was initiated in order to have high tensile and yield strength as well as good corrosion resistance.

Below is a representation of zirconium metal properties.

Table 2.2: Physical nature of Zirconium metal (Schweitzer, 2003).

Properties	**Zirconium**
Atomic number	40
Atomic weight	91.22
Density at 20°C	6.510
Melting Point	1845°C
Boiling Point	3577 °C
Thermal conductivity	100 °C, 0,049 cal/s/cm/ °C
Specific heat	0.067 cal/g/ °C
Electrical resistivity	40$\mu\Omega$.cm

Zirconium belongs to a class of elements known as refractory metals. These are metals with extraordinarily high resistance to heat and wear. Refractory metals include elements such as titanium, niobium, molybdenum and tungsten. They exhibit properties including high melting point above 1,850 °C. They are chemically inert with relatively high densities. They are used in high temperature operations since they offer stability against creep

deformation at elevated temperatures and in corrosive environments. Below presents Table 2.3 demonstrating a table that demonstrates the mechanical properties of zirconium metal which makes it preferable for alloying.

Table 2.3: Structural nature of Zirconium metal.

Properties	**Zirconium**
Tensile Stress	379 MPa
Yield Stress	207 MPa
Modulus of shear force	33 GPa
Young's Modulus	68 GPa
Poisson's Ratio	0.35

2.1.2.2 Zirconium Alloys

Zirconium alloy formation first begun with the identification of relevant elements which could improve the corrosion resistance of the Kroll sponge zirconium to a level comparable to a quality Iodine crystal bar. The elements considered included tin, tantalum and niobium respectively. These metals showed decreasing order of effectiveness and avoided the damaging effect of impurities present in the sponge zirconium. With a drop from 5wt% to 2.5wt% of tin, it was realized that after some time in service the alloy begins to yield to rapid continuous corrosion. This led to the subsequent addition of other alloying elements. Presently, the use of zirconium alloy has gained vast applications in various industries. The two foremost series of zirconium alloys have become the major constituents for the development of fuel claddings. They are namely: Zr-Nb and Zr-Sn. These alloying elements play an important role in either strengthening the base solid or improving one or more of the material properties. Tin is mainly used for solid solution hardening to increase

the creep resistance and strength of zirconium alloys (Liu, 2007). Niobium (Nb) increases the strength, ductility, and corrosion resistance when added to zirconium (Crepin, 1995). When oxygen is combined with the elements such as Iron (Fe) or Chromium (Cr) as alloying metals, the resultant alloy tends to have improved plastic deformation resistance since the oxygen tends to fill in empty voids in the lattice structure of the material.

A list of the zirconium cladding alloys used in thermal reactor applications and their chemical compositions are shown in Table 2.4 below. Trace metals in zirconium alloys are typically transition metals (Ni, Cr, Fe) and they are mostly insoluble within the alpha - Zr phase which precipitate out as metallic flakes. These flakes, depending on the size distribution, will have a substantial impact on the corrosion behavior of the alloys.

Table 2.4 Mean Composition of Zirconium alloy by weight percentage (%).

	Mean Composition in Weight %					
Zirconium Alloys	**Sn**	**Fe**	**Cr**	**Ni**	**O**	**Nb**
Zr - Sn Alloys						
Zircaloy-1	2.5	-	-	-	-	-
Zircaloy-2	1.20–1.70	0.07-0.20	0.05-0.15	0.03 – 0.08	-	-
Zricaloy-3	0.25	0.25	-	-	-	-
Zircaloy-4	1.20–1.70	0.18-0.24	0.07-0.13	-	-	-
Zr-Sn-Nb Alloys						
ZIRLO™	1.00	0.10	-	-	-	1.00
Alloy 635	1.20	0.40	-	-	-	1.00
Zr - Nb Alloys						
Zr – 1Nb	-	-	-	-	-	1.00
Alloy M-5	-	-	-	-	0.10	1.00

2.1.3 Steels

They are ferrous materials which are mostly alloys of mainly iron and carbon with other trace elements. Steels are also classified according to the carbon content as mild, medium and high carbon steels. The carbon content of the steels have a direct relationship with the physical characteristics of the metal.

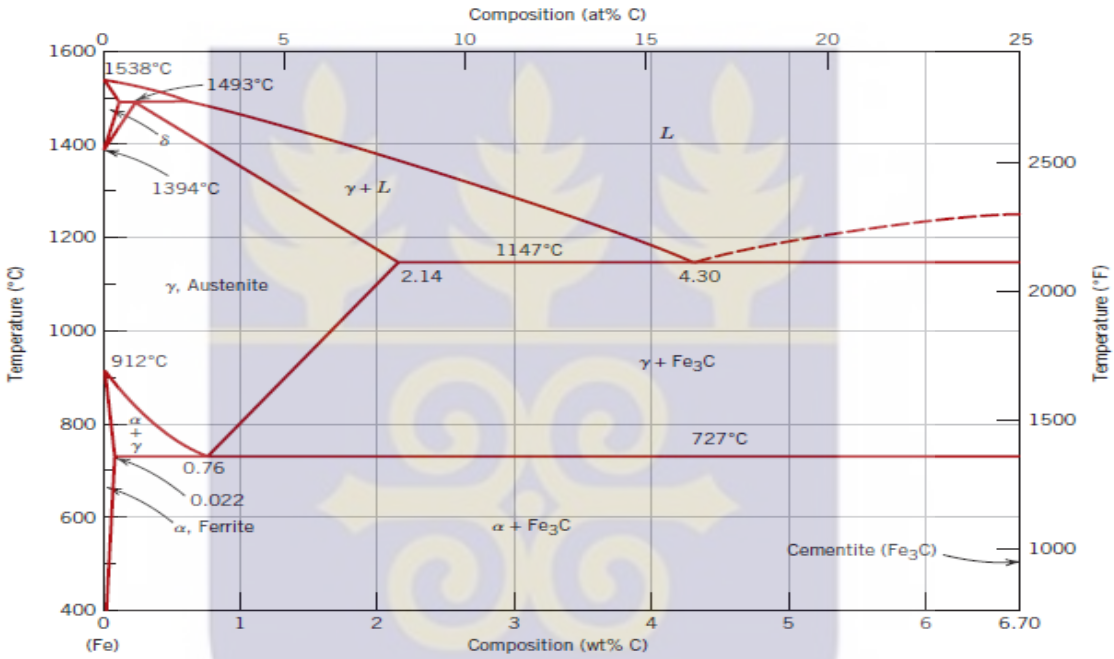

Figure 2.1: Iron-iron carbide phase diagram (Massalski, 1990).

2.1.3.1 Stainless Steels

They are Steels with about 11 wt% of chromium. They exhibit high corrosion resistance. On the basis of microstructure, stainless steels are classified as ferritic, martensitic and austenitic stainless steels. They exhibit high strength and toughness at the extremes of temperature scales (Callister Jr., 2005).

2.1.4 Limitations of Zirconium and Stainless Steel alloys in Nuclear Application

Oxygen is central to the structure of Zirconium and Stainless Steel alloys. Its existence is originally considered as an impurity. Oxygen influences the slip behavior of alloys in proportion to its concentration within the matrix structure. Its interaction on the aqueous environment forms an oxide layer. This layer serves as a protection site for further corrosion. This oxide layer formation however reduces the amount of matrix atom in the clad tube. This reduction in the amount of the matrix material puts more pressure on the cladding tube thereby cracking the protective oxide layer. Eventually, failure occurs as a result of increased localized corrosion. The oxygen atoms which hitherto were responsible for filling the empty voids in the crystal lattice now compete for the oxide layer. They therefore leave behind vacancy-base alloy which changes the microstructure and behaviour of the component. This invariably changes the nature of the alloy. The increase in the number of vacancies increases the paths for diffusion available to free atoms which lead to high rate of failure. Creep occurs which leads to plastic deformation which is undesirable in cladding materials.

2.1.5 Irradiation of cladding

The exposure of structural materials in the nuclear environment to fission products can lead to unique phenomena. A crystal lattice describes atomic nuclei occupying lattice sites with a sea of electrons filling the remaining volume. This crystallographic structure allows for the entrance of alpha, beta and gamma particles as well as high-energy neutrons into the lattice. The alpha particles tend to gather in regions around voids and other defects leading to pockets of helium and alteration of creep behaviour within the crystal.

The high-energy (prompt/fast) neutrons, in the simple terms, act like a billiard ball striking one nucleus and potentially rendering it loose from its lattice site. This now-free atom may interact with other lattice sites or become a self-interstitial. In either case, this potentially raises the energy of the crystal and leads to atomic displacement which contributes to easier corrosion of the lattice.

The injected vacancies from the removal of a metal ion of the cladding element forming the oxide layer have multiple potential paths. The first is in-situ vacancy annihilation at the oxide/alloy interface. If this annihilation does not ensue, then the vacancy may precipitate out to form a dislocation and later a void (Gibbs and Hales, 1977). The voids created, coalesce and grow to affect the corrosion resistance, mechanical, and thermodynamic properties of the alloy. The elevated levels of oxygen beneath the oxide layer leading to reduced ductility and fracture toughness (Chung and Kassner, 1998).

Irradiation of zirconium alloys creates "black-spots", or clusters of irradiation-induced defects, small dislocation loops, short line dislocations, and dislocation entanglements. These three dislocations related defects occur on the prismatic plane with an <a> - type Burgers vector at lower fluence and associated fuel burnup. At higher burnups, there is an increase in oxidation leading to mechanical disturbance, creep, decrease in ductility, growth and increase in brittle-type fracture behavior (Chung and Kassner, 1998).

As the clad is exposed to a flux of high-energy particles, displacement of the lattice atoms create dislocations and other crystalline defects and imperfections. This affects the mechanical and crystalline properties of the alloy. With oxide layer formation, this creates the potential for super saturation of vacancies in the base alloy. The coalescing of vacancies into voids and increasing the oxygen content in the region below the oxide layer, the properties of the alloy greatly changes with increased fuel burnup. The localized corrosion

aggravated by the incident high-energy neutrons, also enables diffusion of hydrogen into the alloy creating embrittlement or diffusion of fission products into the overall system or environment including the welds.

Several processes have been designed to alloy cladding material achieve good texture for the best strength and material properties. These processes include annealing to reduce existing defects and vacancies. Other mechanisms also used include the exploration of different alloying compositions to improve upon corrosion and diffusion. This makes it much easier to achieve the goal of higher burnups for better efficiencies.

2.2 Interactions of Particulate Matter

The interaction of particles such as photon or neutron with matter is dictated by short-range forces. Maxwell's equations describe precisely interactions of long wave-length radiation, which readily yields a wave equation for the electric and magnetic fields of radiant energy (Olander, 2006). Neutrons, which are neutral particles, move in a straight line through a medium, where they are intersperse by occasional "point" interactions, in which the neutral particle is absorbed, scattered or cause some other forms of reaction. Interactions are stochastic in nature, as particles travel between successive collisions within the medium. These collisions are predicted only in some average or expected sense. The interaction of a given type of radiation with matter may be classified according to the type of interaction, the nature and manner with which the interaction takes place. The interaction may take place with an electron, in which case the electron behaves as though it is free. Likewise, interactions of particles may take place with an atomic nucleus, which in many cases behaves as not bound in a molecule or crystal lattice. However, lattice energy of crystalline materials also places an important role in the various forms of interactions. In

most instances, these interactions involve energy transfer from the radiation to the target matter with which it interacts. Matter consists of atomic nuclei and extra nuclear electrons. Radiation may interact with either the atomic nuclei, electrons in the shell or both depending on the energy of the incident particle. The propensity of any particular category of interaction, and consequently the penetrating power of the various radiations, depends on the type and energy of the radiation as well as on the nature of the absorbing medium. The interaction in most cases leads to excitation and ionization of the absorber atoms resulting from their interaction. Energy in the form of heat is dissipated.

2.2.1 Particle - Solid Interactions

Nuclear interactions include the interaction of charged particles with atomic nuclei in a solid medium (Olander, 2006).These nuclear interactions produce permanent atomic displacements within solid. These displacements give rise to vacancies and interstitials which develop into dislocation loops in picoseconds. These are detrimental to the crystal structure as they lead to microstructural evolution. The effect of an external flux of energetic particles in a crystal structure maybe categorized into two components: thus by creation of primary knock-on atoms or the creation of transmuted atoms. This is shown below:

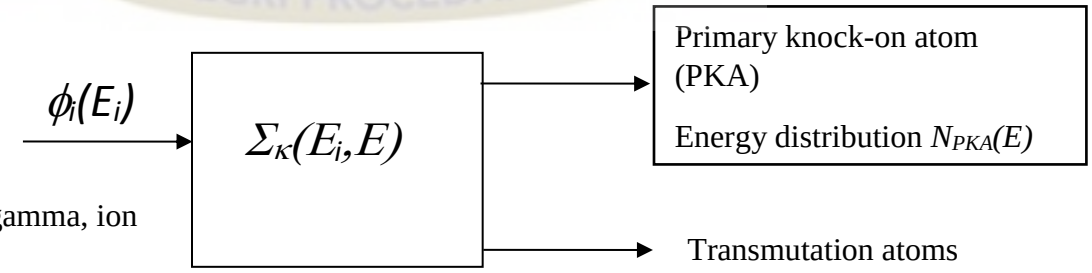

Figure 2.2: Particle interaction in crystal structure (Olander and Arthur, 2015).

$\phi_i(E_i)$ represents all particle fluxes **i** incident on the solid (***i***=neutron, gamma), while $\Sigma_\kappa(E_\iota,E)$ represents the probability of interaction of all relevant particle-solid reactions *k*, transferring energy *E* to the atoms in the solid. The product of interaction of the flux of energetic particles (represented by ϕ) and the atoms in the solid (represented by Σ) is the creation of $N_{PKA}(E)$ self-atom recoils called primary knock-on atoms (PKAs) and a concentration of transmutation atoms C_k, where *k* represents the atomic species created.

2.2.1.1 Cross-Section

The probability of interaction of particles between the atoms in the solid and the incident particle flux is commonly represented as the cross-section for the reaction. The notion of the microscopic cross-section is illustrated in figure 2.3 below. Research shows that reaction rates are influenced by the apparent size of the atoms in the solid. The finer the size, the faster or higher the reaction rates and vice versa. (Olander and Arthur, 2015). Given that, there exists particle flux in a solid of a given atomic density, the probability of reaction increases with the apparent particle size. This is illustrated in figure 2.3 where two types of atoms are present in the solid: atom A has a greater reaction rate for reaction 1 than atom B, and thus these atoms appear as large as when reaction 1 is considered. In contrast, reaction 2 has atom B to have a much larger cross section and consequently these atoms appear bigger for reaction 2.

The differential probability for solid particle interactions is defined as

$$dP = N\sigma(E_i)dx = \Sigma dx \qquad (2.1)$$

Where *d*P = differential Probability; N = target atoms per unit volume; E_i = Energy of incident particle; σ = Microscopic cross-section; dx = Thickness of medium;

$\sum$ = Macroscopic cross-section.

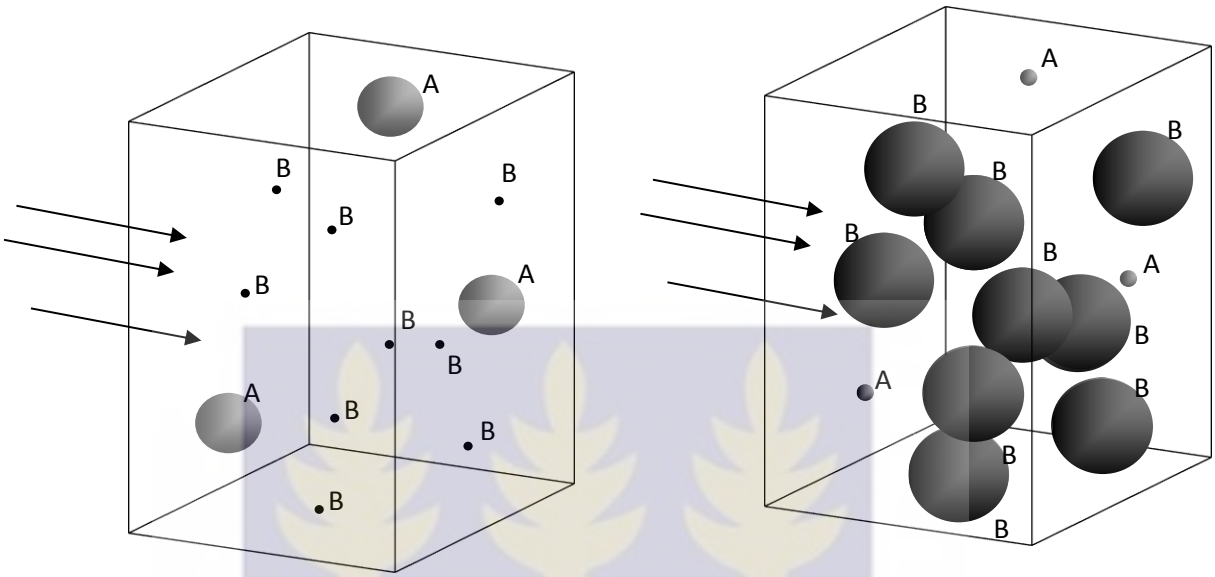

Reaction 1 Reaction 2

Figure 2.3: Schematic representation of the cross-section concept (Olander and Arthur, 2015).

2.2.2 Interaction of γ-radiation with structural components

Primary radiation is represented by γ-radiation entitled by the fission related activities in the reactor core. The photons therefore interact with the lattice atoms of the crystal structure. In these interactions, high energy electrons are produced which travels within the structural components. Electrons are affected by electromagnetic collisions since they are charged. Collision in the "electron cloud" slows down the electrons in their trajectory. While interactions against nuclei are rarer and do not cause a big energy loss, since the electron mass is much smaller than the nucleus mass (Tsegay, 2011) and (Festus, 2014).

It has been shown that, photons do not dissipate energy directly to the atomic nuclei, rather electron are energized by one of the three known interactions of gamma rays with electrons

in the outer orbits of the atom at the range of energies from (0.1MeV < E < 1.5MeV). They are; Photoelectric effect, Pair production and Compton scattering (Knoll, 1989).

These processes lead to displacement cascades in solid as a result of the energetic electrons that are excited. The processes are dominant at different energy ranges.

2.2.2.1 Photoelectric effect

The photoelectric effect is an absorption process which occurs for X-rays due to their low energies. A photon of energy $E_e < 0.1$ MeV is transferred to an inner tightly-bound electron in a K-shell orbital. This gives the electron sufficient energy to escape from the atom. In photoelectric effect, the incident gamma ray interacts with an entire atom where photon is absorbed. The resultant electron is a photoelectron.

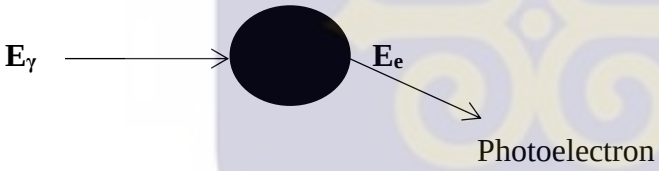

Figure 2.4: Representation of Photoelectric effect.

2.2.2.2 Pair production

This is an electromagnetic interaction which involves the disappearance of a photon for two resultant electrons (positron and negatron). This process is possible only if the gamma ray energy exceeds twice the rest-mass energy of the electron (i.e. 1.02MeV). The cross-section for a pair production σ_{pp}, increases steadily with increasing energy of the photon (Birikorang and Nyarko, 2014). Pair production takes place in the vicinity of the columbic field which enables the motion of the electrons. These electrons lose energy through ionization and excitation in collision. At very low energies the positron slows down and

combines with the electron. After the combination of the two particles they annihilate radiation with energies of 0.511MeV each.

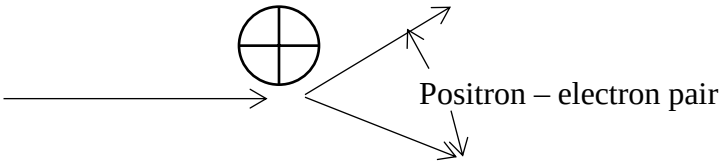

Figure 2.5: Representation of Pair Production.

2.2.2.3 Compton scattering

Compton scattering is the most important of all the three interaction of gamma with electrons. It is essentially an elastic collision process of a high-energy photon with the free electron initially at rest. An incoming photon of high energy (>0.1 MeV) collides with an electron in the valence band, ejecting the electron from the atom. The energy of the ejected or Compton electron can be determined by knowledge of the energies of the incoming and scattered photons.

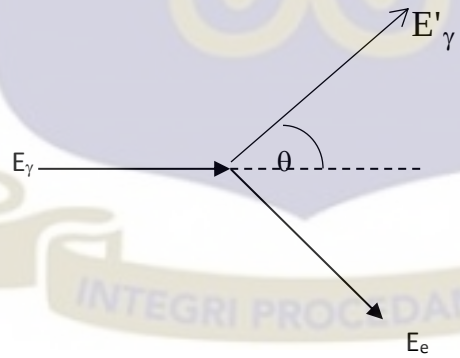

Figure 2.6: Representation of Compton Effect.

The expression that relates the energy transfer and the scattering angle for any given interaction are given below.

$$E_\gamma = E'_\gamma + E_e; \qquad (2.2)$$

Where; $$E'_{\gamma} = \frac{E_{\gamma} \times m_e c^2}{m_e c^2 + E_{\gamma}(1 - \cos\theta)} \quad (2.3)$$

2.2.3 Radiation damage

Radiation damage refers to the localized microscopic defects which occurs in the crystal lattice of a solid when high-energy radiation traverses through it. The end result is the modification of the lattice structure which affects the physical, chemical and mechanical properties of the structural component. Desired material properties such as strength, toughness, ductility, dimensional stability are largely influenced by the nature of the defect structure. Grain size, internal interface, size and density of second phase precipitation, dislocation densities all affect the nature of the defect structure (Stoller, 2011). The microscopic defects that are as a result of the interaction of high-energy subatomic particles and radiation with crystal lattice atoms gives rise to vacancies and interstitials. These point defects coalesce to form dislocation which degenerates into voids. Most radiation damages are caused by neutrons and fission fragments. Some other types of radiation generally have insufficient energy (or are not produced in large enough quantities) to cause major damage.

The main stages or development of radiation damage are composed of distinct processes. These processes occur in the sequence below (Osetsky, 2008):

1. Formation and growth of defect cluster and dislocation loop. This causes matrix hardening.

2. Radiation induced and enhanced diffusion. This second stage is characterized by phase stability changes with segregation and precipitation.

3. Coagulation of voids and gas bubbles which induces swelling of matrix structural component.

4. Anisotropic diffusion due to high degree of randomness of defects in different direction of the crystallographic plane leads to radiation growth.

5. Finally, induced-stresses cause the component to creep.

2.2.3.1 Knock-on atoms and displacement cascades

Atomic displacement may occur in a ballistic manner through kinetic energy transfer or by the transformation of radiation-induced excitation into atom motion by recoil cascade. Charged particles pass through matter causing ionization. The particle energy is dissipated by exciting orbital electrons and by elastic collisions with the material nuclei at relatively low energies. An elastic collision can eject an atom from its normal lattice position. The ejected atom is known as a primary knock-on which may cause a cascade of atomic displacements of secondary knock-on atoms before eventually coming to rest. They create a Frenkel pair of a vacancy and interstitial simultaneously (Olander, 1975).

The PKA interacts with its neighboring atoms causing many collisions and atomic displacements in a localized region. The final damaged state evolves as a result of intra-cascade clustering and recombination, and consists of a distribution of interstitial and vacancy clusters of different sizes. The spatial distribution of the created microscopic defects is non-directional and non-uniform. Because the interstitials require energetic atoms, they form the replacement collision sequences where the incident particles replace the primary knock-on atom.

For every displacement of a lattice atom there exists a displacement threshold energy E_d within the crystal such that the incident particle energy T disperses. Primary knock-on is possibly only feasible if; $T > E_d$. For an isotropic elastic collision, the maximum energy dissipated is represented as

$$T_{max} = \Lambda E_n \qquad \text{Where} \qquad \Lambda = \frac{4A}{(1+A)^2} \tag{2.4}$$

A = atomic mass, E_n = neutron flux energy

The rate of atomic displacement will be represented as the product of the number of atoms N and the displacement cross-section.

$$R_d = N\sigma_d(E_n)\phi(E_n) \tag{2.5}$$

$$dpa = \frac{R_d.t}{N} = t\int_{\frac{Ed}{\Lambda}}^{\alpha} \sigma_d(E_n)\phi(E_n)dE_n \approx t\int_0^{\alpha} \sigma_d(E_n)\phi(E_n)dE_n \tag{2.6}$$

$$\sigma_d(E_n) = \int_{E_d}^{\Lambda E_n} \sigma_n(E_n, E)V(E)dE \tag{2.7}$$

2.2.3.2 Radiation damage model

There are basically three methods known for calculating the displacement per atoms (dpa). They are namely;

a. Kinchin - Pease model method

b. Lindhard model method

c. Norgett - Robinson Torren model method

a. Kinchin - Pease model method

For a PKA with energy E, the total number of displaced PKA can be estimated by the Kinchin-Pease method as follows (BNL, 2006): for a displacement cascade to take place, at time t=0, E >$2E_d$; then displacement of PKA occurs. Assuming an elastic collision, then the number of PKA created (N) PKA have an average energy $\overline{T}$ of

$$\text{N=1}, \overline{T} = \frac{E}{2}; \quad \text{for N=2}, \overline{T} = \frac{E}{4} \text{ and N= n}, \overline{T} = \frac{E}{2^n} \tag{2.8}$$

Displacement cascade ends when $\overline{T} = 2E_d$. If $\overline{T} > E_d$; A single PKA is generated which could lead to the formation of an interstitial atom.

$$v(E) = \begin{cases} \dfrac{E}{2Ed} if .E > E^* \\ \dfrac{E}{2Ed} if .2.Ed < E < E^* \\ 1, if .E_d < E < 2E_d \\ 0. if .E < E_d \end{cases} \tag{2.9}$$

v(E) =Atomic displacement produced by PKA's; E_d = Displacement Energy;

Kinchin-Pease model is based on the following assumption below (Olander, 1975):

i. Only two bodies engage in an elastic collision.

ii. Atomic displacement is triggered only $\overline{T} \geq E_d$

iii. Hard sphere models are preferred to realistic potentials.

iv. Atomic structure has imperfections.

v. No annihilation after collision.

b. Lindhard model

This model is only valid in the nuclear stopping regime. This regime is characterized by E < E^*. It's mostly applicable in realistic potential than in hard sphere. Thomas-Fermi used this model to predict the energy partition between electronic and nuclear stopping (Greenwood, et al., 1985). Assuming nuclear stopping portion of the deposited energy is converted to atomic displacement; the amount of displacement is evaluated as below:

$$V_L = \zeta(E,Z)\frac{E}{2E_d} \qquad (2.10)$$

$$\text{Damage efficiency} = \xi(E,Z) = \frac{1}{1+0.88Z^{\frac{1}{6}}(3.4\varepsilon^{\frac{1}{6}}+0.4\varepsilon^{\frac{3}{4}}+\varepsilon)} \qquad (2.11)$$

Where $\varepsilon = \frac{E}{2Z^2e^2/a}$; Screening radius = a; $a = \frac{\sqrt{2a_B}}{(Z_1^{2/3}+Z_2^{2/3})^{1/2}}$ with a_B as Bohr radius.

c. Norgett - Robinson Torren model method

Norgett-Robinson Torrens (NRT) is a modified model of the Kinchin-Pease model which is valid for all primary knock-on range particularly for Z > 20.The NRT model gives a stable Frenkel pair produced through interaction (Parkin and Coulter, 1981). Norgett-Robinson-Torrens model considers neutron irradiation recoil energy of less than 50keV (Norgett, et al., 1975). The number of displacement is expressed in the form:

$$V_{NRT} = 0.8\frac{E}{2E_d} \qquad (2.12)$$

$$dpa = [\phi(E).t][\sigma(E)] \qquad (2.13)$$

$$dpa = [\phi(E).t]\left[\int_{E_d}^{T_{max}} V_{NRT}.\sigma(E,T)dT\right] \qquad (2.14)$$

It is important to add that both Lindhard and Norgett-Robinson Torrens models have some limitations. These are;

(i). Differences in atomic masses of colliding bodies are not taken into account.

(ii).The variation in displacement energies with regards to crystalline orientation is not considered.

2.2.3.3 Displacements caused by Neutron Irradiation

In nuclear power reactors, neutrons and gamma rays bombard the nuclear fuel and reactor components at a high velocity due to their high energies. Fast neutrons are therefore the major causes of irradiation. To evaluate the displacement rate k in a neutron flux spectrum $\phi(E_n)$, the displacement cross section $\sigma_d(E_n)$ is needed. k in units of dpa/s is given by:

$$k = \int_{\frac{E_d}{\Lambda}}^{\infty} \sigma_d(E_n)\phi(E_n)dE_n \qquad (2.15)$$

The integral expression has as its lower limit the lowest energy for neutrons capable of transferring at least E_d to the atoms in the solid. The displacement cross section is

$$\sigma_d(E_n) = \int_{E_d}^{\Lambda E_n} \sigma_s(E_n, E)\nu(E)dE \qquad (2.16)$$

For equal scattering in all directions, (PKA energies E are equally probable), then $E_d << E_n$

$$\sigma_s(E_n, E) = \frac{\sigma_s(E_n)}{\Lambda E_n} \qquad (2.17)$$

$$\sigma_d(E_n) = \frac{\sigma_s(E_n)}{\Lambda E_n} \int_{E_d}^{\Lambda E_n} \nu(E) dE \tag{2.18}$$

Substituting equation (2.18) into equation (2.15) gives

$$k = \int_{\frac{E_d}{\Lambda}}^{\infty} \phi(E_n) \left[\frac{\sigma_S(E_n)}{\Lambda E_n} \int_0^{\Lambda E_n} \nu(E) dE \right] dE_n \tag{2.19}$$

Using the Norgett-Robinson Torrens

$$\nu_{NRT} = 0.8 \frac{E}{2E_d} \tag{2.20}$$

$$k_{NRT} = \int_{\frac{E_d}{\Lambda}}^{\infty} \phi(E_n) \left[\frac{\sigma_s(E_n)}{\Lambda E_n} \left(\int_0^{\Lambda E_n} \left(\frac{0.8E}{2E_d} \right) dE \right] dE_n \right. \tag{2.21}$$

Solving $\int_0^{\Lambda E_n} \left(\frac{0.8E}{2E_d} \right) d(E)$ gives $\frac{(\Lambda E_n)^2}{5E_d}$ (2.22)

By substitution,

$$k_{NRT} = \int_{\frac{E_d}{\Lambda}}^{\infty} \phi(E_n) \left[\frac{\sigma_s(E_n)}{(\Lambda E_n)} \left(\frac{(\Lambda E_n)^2}{5E_d} \right) \right] dE_n \tag{2.23}$$

Rewriting the equation above gives the generalized equation below;

$$k_{NRT} = \frac{\Lambda}{5E_d} \int_{\frac{E_d}{\Lambda}}^{\infty} \phi(E_n) \sigma_S(E_n) E_n dE_n \tag{2.24}$$

The displacement rate from the known neutron flux can be obtained by integration.

Monochromatic neutron flux approximation is used to derive the magnitude of atomic displacement that have ensued.

The overall average neutron flux is evaluated as given below:

$$\phi(E_n) \cong \delta(E_n - \bar{\bar{E}}_n) \phi_t \tag{2.25}$$

Where $\delta(E_n - \overline{E}_n)$ is the Kronicka delta, ϕ_t is the total damage producing neutron flux given by

$$\phi_t = \int_{\frac{E_d}{\Lambda}}^{\infty} \phi(E_n) dE_n \tag{2.26}$$

$\overline{E}_n$ which is the average neutron energy is given as;

$$\overline{E}_n = \frac{\int_{\frac{E_d}{\Lambda}}^{\infty} \phi(E_n) E_n dE_n}{\phi_t} \tag{2.27}$$

While, for a monochromatic neutron beam of energy $\overline{E}_n$,

$$k_{NRT} \cong \phi_t \frac{\sigma_S(\overline{E}_n)}{5E_d} \Lambda \overline{E}_n \tag{2.28}$$

2.2.3.4 Radiation induced defects

Structural materials occur originally with defects. They are fabricated with imperfections due to the fact that the orderliness in arrangement of lattice atoms is not perfect. The imperfection makes them amenable to mechanical and chemical transformation (Callister Jr., 2005). A point defect created can lead to a cluster of point defects which easily turns into a dislocation in a matter of picoseconds. Figure 2.7 below shows defects susceptible to changing material properties of a lattice structure.

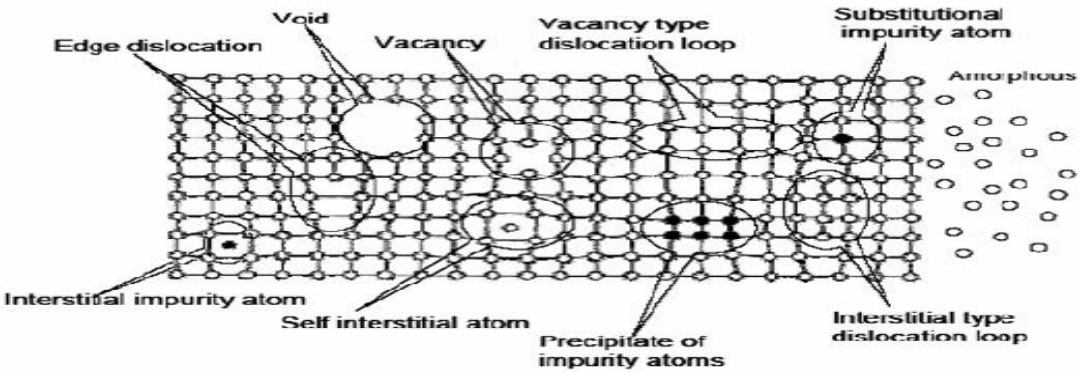

Figure 2.7: Defects susceptible to changing material properties of a lattice structure (IAEA, 2014).

2.3 Radiation effects on structural components

Fission processes in the reactor core occurs as a result of splitting of heavy nuclei ($^{235}_{92}U$) by neutrons into two fragments releasing large amount of energy in the process. The new neutrons can in turn cause new fissions. Each fission reaction releases an average of about 200 MeV. This energy is dissipated in the form of heat. Of the fragments that are formed as fission products in the reactor, some are rare gases which are of special importance, because they have very high absorption cross sections. Their presence has a large influence on the reactivity (Dam, et al., 2005).

Xenon – 135 reactivity effects are dependent on its concentration during operation of the reactor and they buildup some hours after shut down as their half-life is about 9.2h.

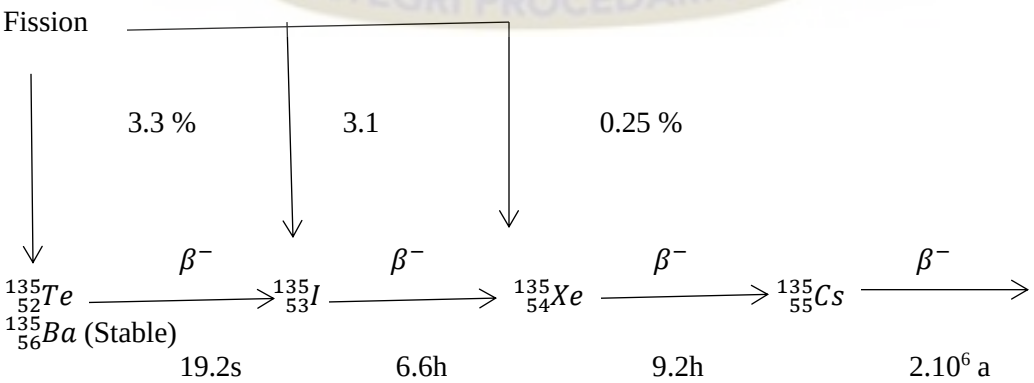

Figure 2.8: Beta decay of Daughter Nuclei born from Fission process.

During irradiation in a nuclear reactor, some of the burnable poisons such as Krypton and Xenon cause the fuel to swell due to their precipitation into bubbles (Matzke and Turos, 1992). Iodine which is a volatile element has the possibility of causing fuel failure by stress-corrosion (Hocking, et al., 2001). The other elements however form solid precipitates in the fuel and with the cladding material (Matzke, et al., 1994). Other gases such as helium are of major concern in fuel technology.

2.3.1 Irradiation cascade

The essential, microscopic events that precede the appearance of visible changes in the solid are termed irradiation damage. When energy transferred to the lattice atom (displacement energy) exceeds the lattice binding energy of the atom in its lattice, the lattice atom is displaced from its original position. The displaced atom (recoil atom) might carry high enough kinetic energy to create series of lattice displacements before it finally comes to rest. The displaced atom ultimately appears in the lattice as an interstitial atom. The empty lattice sites left behind by the displaced atoms become vacancies or are replaced by the incident atom. The collection of point defects as a result of vacancies and interstitials created by a single primary knock-on atom is known as a displacement cascade.

During atomic collision cascades, vacancies and interstitials can be produced so close to each other that clustering of the point defects occurs spontaneously within the short time forming dislocations and voids. Due to the proximity of the clustering point defects, many of the vacancies and interstitials produced by the high-energy collisions obliterate. Just a little as low as 1% of the initially generated defects survives and are capable of producing visible radiation damage (Olander, 1976).

The bombarding particle accelerated at particular projected range transfers energy on the order of ten to hundreds of kilo electron volts for stationary lattice atoms. The energy dissipated by incident ion in the solid is separated into two parts:

(i). Discrete elastic atom - atom collision that is useful reducing the energy of the incident atom and also responsible for lattice displacements.

(ii). A continuous process of electronic excitation contributes to energy loss.

Interaction between the moving atoms or ions with the outer electrons (valency) of the solid constitutes the major energy loss process at high energies. Energy Transfer from a moving atom to an electron does not lead to displacement but excitation. Energy is transferred to the electrons in small increments so closely spaced that the process can be regarded as a continuous loss of energy. Furthermore, displacements are only caused during elastic atom-atom collisions, where a significant portion of the initial kinetic energy possessed by incoming atom is transferred.

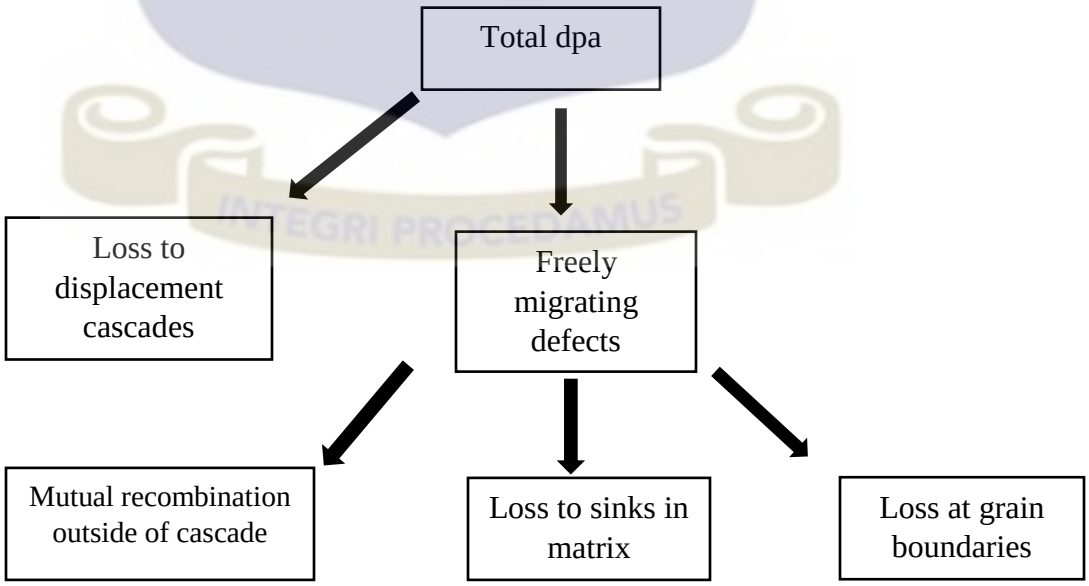

Figure 2.9: Point defect history during avalanche of displacement cascade (Was, 2007).

Recent researches on MD simulations creates the impression that displacement cascades are in two main forms (Diaz de la Rubia, 1989) and (Heinish, 1993). These include the first ballistic stage where several particles are extricated from their lattice sites and then secondly, thermal spike phase where the cascade region attains thermal equilibrium with the immediate environment. The recalculation of the energy of atoms in the dense collision region into temperature (k) with the aid of the equation $E = 3/2.N.k_BT$, gives initial temperatures of the order of 10,000 K. This high temperature region encourages the creation delocalized defects with radius less than 50 Angstrom (Å) inside the solid. This phenomenon is called a "thermal spike".

Thermal spike maybe seen as localized melting of the irradiation affected regions which is followed by fast quenching leading to a change in phase which forms a damaged amorphous structure. Thermal spikes normally cool down to the ambient temperature in 1-100 ps. Some experiments have shown that thermal spike are able to induce a phase transition which requires a very high temperature (Bacon and Diaz de la Rubia, 1994).

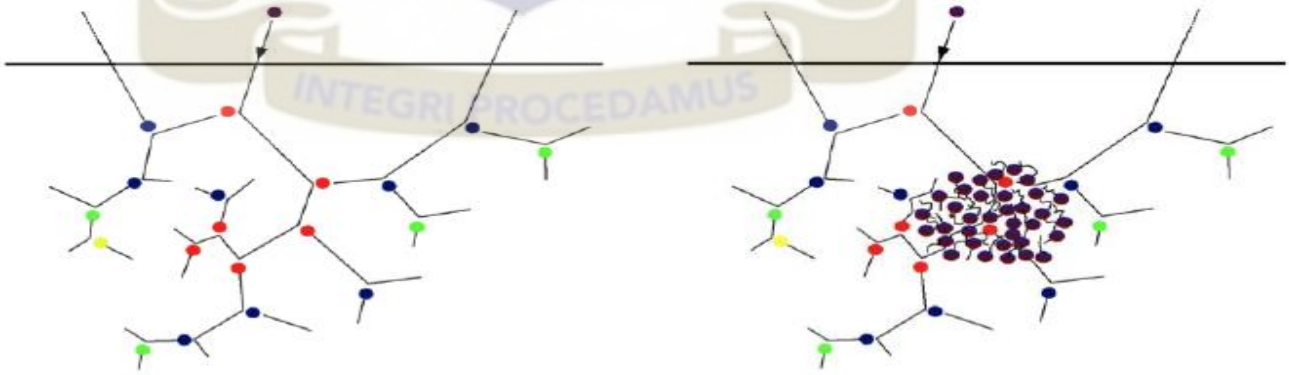

a. linear collision cascade b. thermal spikes

Figure 2.10: Schematic illustrations of linear collision and thermal spikes (Meldrum, 1998).

The cooling of displacement cascade occurs by way of conduction through the lattice and heat conductivity by electronic means. The final stage of a cascade is the relaxation phase, when the defects migrate and possibly recombine; they last for some picoseconds to an infinitely small times, depending on its structure, its defect migration and recombination properties, at ambient temperature.

2.3.2 Radiation effects in nuclear fuels

The main source of energy in nuclear fuel is slowing down of high-energy fission products. It is this slowing down of high-energy that leads to damage by radiation. Fission products passing through reactor materials lose part of their energy to the atoms of these structural components and eject some lattice atoms from their normal positions in the materials, replace or stay as interstitial atoms. The collective result is manifested in drastic modification of the material and structural properties of irradiated materials. These properties include changes in dimensions, strength and hardness, conductivity of heat and electricity, magnetism, resistance to corrosion, resistance to irradiation, toughness and creep just to mention a few. These properties have a direct relationship with service life of most structural components in nuclear application.

It is generally known atomic displacements contribute significantly to the source of radiation effects in nuclear materials (Matzke, 1992). These displacements are predominantly caused by the fission process which occurs in the fuels. Displacements often lead to the localized and delocalized changes in microstructure, composition and stoichiometry. These effects result in the modification of physical properties of core materials. For example, the lattice parameter in UO_2 increases as a function of irradiation

dose. This is due to the variation in the population of defects (interstitials and vacancies) and their clusters.

2.3.3 Radiation Effects in Cladding material

Radiation-induce defects are sustained on the cladding material. These point defects are formed instantaneously within picoseconds. These defects generally results into changes in the mechanical and physical properties of the cladding material. At low homologous temperatures and low radiation dose (0.001- 0.1 dpa), defects lead to matrix hardening when they pin dislocation motion. The pinning of dislocation movement promotes strain-hardening and reduces the ductility of the material especially in body centered cubic (BCC) crystals. At intermediate homologous temperatures $0.4 \leq T \geq 0.6$ and higher radiation doses (1-10 dpa), radiation-induced segregation and radiation-induced precipitation can lead to localized corrosion or mechanical property degradation, such as grain boundary embrittlement (Mansur, et al., 1997).

Radiation-induced segregation and diffusion leads to phase change of the structural material which affects the distribution of alloy elements. Voids created as a result of this phase change leads to swelling when voids get occupied with displaced atoms thereby changing the crystallographic dimensions.

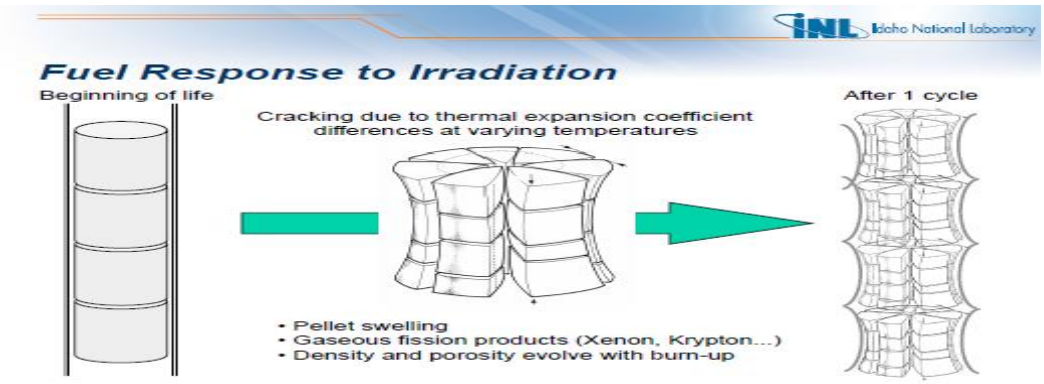

Figure 2.11: Light water Reactor Fuel Performance. (Bouffioux, 2001).

2.3.4 Ion irradiation effects

Energetic beam of ions are bombarded on target surfaces. Ionized particles are emitted from the surface as a result of this interaction. These ions include backscattered ions, secondary ions, and sputtered ions (Nastasi, 2004). Some of the energetic ions penetrate the solid surface experiencing numerous collisions with the target surface before coming to a stop with their final energies. The lost in energy of the incoming distance is expressed as:

$$\Delta E_1 = \left| dE_1 / dl \right| \Delta l \qquad (2.29)$$

The path length is also expressed as:

$$R_t(E_0) = -\int_{E_0}^{0} \frac{dE}{-dE/dl} \qquad (2.30)$$

ΔE_1 = Energy loss along ion path Δl; dE_1/dl = Energy loss per distance; Δl = Path length;

$R_t(E_o)$ = Projected range E_o = Initial energy of ion;

E_1 = Energy of incident particle;

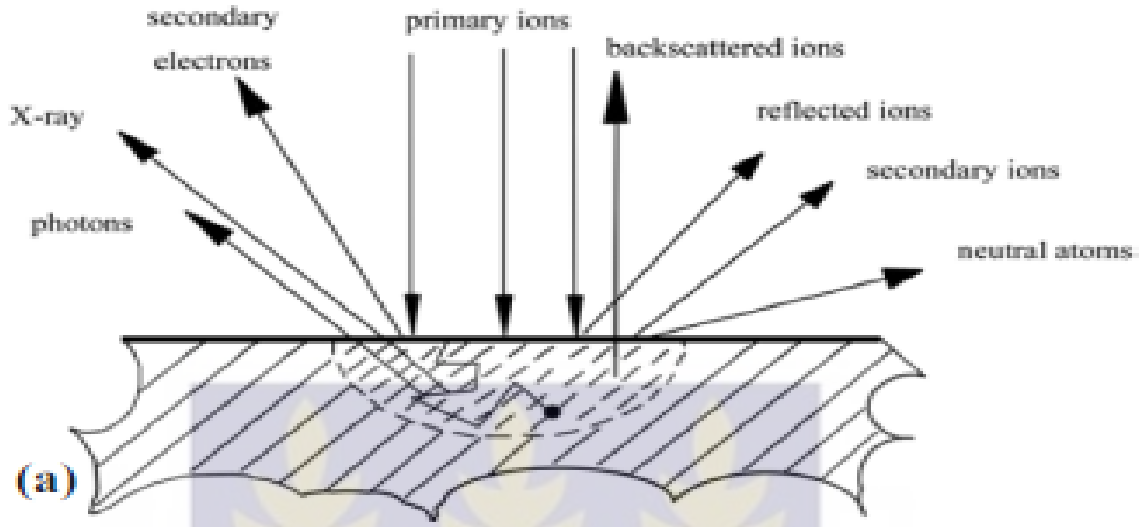

Figure 2.12: Principle of interaction between ions and solid.

Ion irradiation effects are encouraged by sputtering, cascade mixing, and implantation of recoils. These effects develop into 3 – dimensional defects through enhanced diffusion and induced segregation of ions.

2.4 RADIATION DAMAGE SIMULATION

Most commonly used techniques employed in the simulation study of the behaviour of lattice atoms during collision cascades include (Was, 2007):

- Binary Collision Approximation (BCA) method
- Molecular Dynamics (MD) method
- Kinetic Monte Carlo (KMC) method

2.4.1 Binary Collision Approximation (BCA) method

The BCA method is useful in ion irradiation physics. This makes it proficient for computer simulation of defect production and penetration depth of energetic ions by sputtering or ion

implantation in target materials (Robinson, et al., 1974). This method is employed at the collisional stages of recoil cascades in substantial numbers. The BCA method discriminates on other forms of interactions considering only interaction occurring between just two colliding atoms at a specific time. This makes it suited with the Kinchin-Pease model.

The BCA method agrees with the threshold energy theory of discriminating interactions at very high energies, however it considers low energies, ballistic features which includes replacement collision sequence and focused collision. Damage regions are proportionally related to the energies.

The Binary collision approximation methods are categorized into two types according to the degree of orderliness in the atom arrangements. They are namely:

- Binary crystal model
- Monte Carlo model

Binary crystal model (BCM) is of a much ordered crystal structure and employs a deterministic approach in calculation. The later has an amorphous (thus unordered) crystal structure and employs a stochastic method in locating and determining collision parameters. This is achieved by using analytical approach to track particle population in a media.

TRIM code in the SRIM-TRIM code is a typical example of the binary collision approximation code which utilizes Monte Carlo techniques in simulating particle behaviour and associated damage sustained in target solids. It employs maximum impact parameters executed at constant mean free path and specified density for each binary collision (Was, 2007).

2.4.2 Molecular Dynamics (MD) method

The MD simulation method provides detail atomistic processes in microstructural evolution. MD uses algorithms to solve classical motion equations as represented below for as atomic system;

$$m_i \ddot{r}_i = f_i \qquad f_i = -\frac{\partial}{\partial r_i} u \qquad (2.31)$$

m_i = mass of particle i; r_i = position vector of i; fi = force acting on particle i; u = interatomic potential

This equation above requires that the force be evaluated using the interatomic potential of the atom.

Molecular dynamics is categorized into two forms, namely:

- Classical molecular dynamics
- Ab initio molecular dynamics

The first category is useful in treating classical entities for their positions and momentum whilst ab initio molecular dynamics is used separately in resolving electronic and ionic degrees of freedom using wave function distribution for electrons.

Operationally, MD method generates under suitable boundary conditions a projectile path of an atomic system through the integration of the classical motion equations with precise interatomic potential (Cai, et al., 2012).

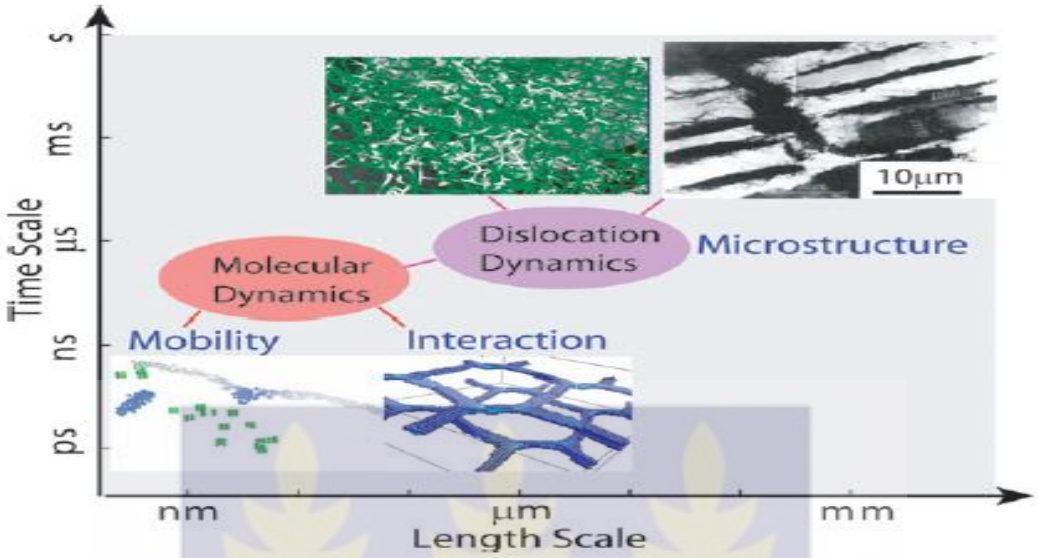

Figure 2.13: MD in the multiscale modeling framework of microstructural evolution (Kopetskii, 1974).

Molecular dynamics is significant in the fact that it gives a unified study of all physical properties. This is achieved by providing structural, mechanical and crystallographic properties of the atomic system. Furthermore, it gives direct link between potential models and physical properties (Cai, et al., 2012).

2.4.3 Kinetic Monte Carlo (KMC) method

The KMC method presents very efficient approach to predicting stochastic behaviour of particles at very relatively infinitesimal scales such as the mesoscale level. The random walk model presents a probabilistic event of tracking particle motion between successive interactions.

The KMC method attempts to subdue the time step of the simulation by exploiting the long processing time of the dynamic system to a state - state diffusive jump. Therefore KCM method neglects the tracing of trajectories from their vibrational periods (Was, 2007).

2.4.4 SRIM – TRIM Code

The SRIM-TRIM code calculates the interactions of energetic ions within the structure of the target media. This code develops a general interatomic potential that is dependent on ionic energy of the interacting atoms. The potential of these ions are of the form demonstrated below:

$$V(r) = \frac{Z_1 Z_2 e^2}{r} \Phi\left(\frac{r}{a}\right) \tag{2.32}$$

Where; Z_1 - Atomic number; Z_2 – Energetic ion; e – Electric charge; r – Interatomic distance; a – Empirical screening length

$$a = \frac{0.8854 a_{Bohr}}{Z_1^{0.23} + Z_2^{0.23}} \tag{2.33}$$

a_{Bohr} is the Bohr radius (the radius of the hydrogen atom, 0.53 Å). Φ is the "universal" screening function determined by precisely fitting of the evaluated interatomic potentials of 521 randomly selected element permutations given by:

$$\Phi\left[\frac{r}{a}\right] = \sum_{i=1}^{4} A_i \exp\left[-B_i\left(\frac{r}{a}\right)\right] \tag{2.34}$$

The "free flight" distance is calculated at the start of the code using the interatomic distance of target media at low energies. At higher energies, a more complex function of the ionic energy and scattering density is applied. With good interaction, the ions undergoes nuclear collision with a particle possessing an impact parameter which randomly selected. For

transferred energy E lower than the displacement energy E_d, the calculation is terminated. Otherwise the code recalculates "free flight" distance original ion and struck atom. This continues until a final energy is reached.

The SRIM-TRIM code keeps record of rate of displacements, percentage of energy lost, vacancies created, replacement collisions, and various other parameters. Nuclear reactions for amorphous structures are not considered (Olander, et al., 2015).

2.4.4.1 TRIM Code

The TRIM is a compendium of software which calculates the stopping and range of ions (between 10 eV- 2GeV/amu) in matter using ion-atom interaction. This calculation is made very easy and efficient by the use of algorithms that allows the ions to make jumps between calculated collisions. The collisions are averaged to get results over the intervening gap. During the collisions, the ion and atom have a screened coulomb collision, this including exchange and correlation interactions between the overlapping electron shells.

2.4.4.2 TRIM Setup Windows

The TRIM setup Windows is a Monte Carlo Transport calculation which is used to run a type of TRIM calculation with the data on the ion and target material. The TRIM Demo is used to familiarize one with the use of the program.

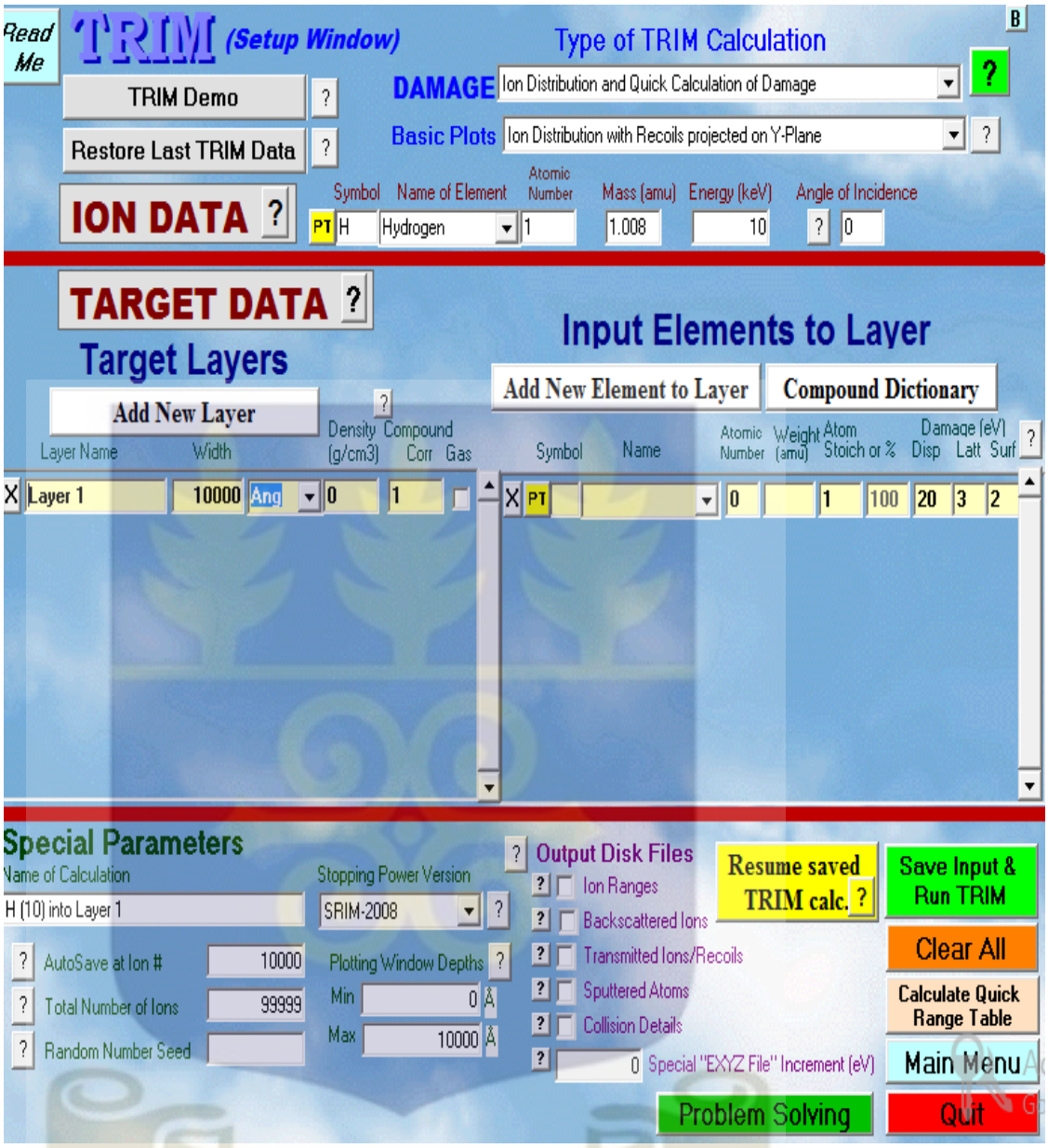

Figure 2.14: Display of TRIM setup Widows.

2.4.4.3 Types of TRIM calculations

2.4.4.3.1 Ion Distribution and Quick Calculation of Damage

This execution of this calculation is employed when the estimation of damage is required in a short time. It is therefore reliable for the evaluation of final distribution of ions in the

target, the Ionization energy loss, Energy transferred to recoil atoms, Backscattering Ions and Transmitted Ions. It is however not suitable for analysis on detailed damage or sputtering.

(Ziegler, et al., 2010).

2.4.4.3.2 Detailed Calculation with full Damage Cascades

This calculation takes into account all collision cascades until the final energy is reached. The program however has a limitation of 8000 atoms collision in a single cascade. TRIM will therefore run out of memory when this limit is reached.

2.4.4.3.3 Surface Sputtering

Surface sputtering is referred to as the removal of atoms from the surface of a target material as a result of collision. It is the opposite of recoil implantation. For sputtering, every near-surface interaction should be considered, and specifying this type of calculation requires TRIM to evaluate every atom collision in detail. The atomic no of the ion should be proportional to the depth of penetration. Therefore heavier ions interaction requires larger depth compared to lighter ions.

2.4.4.3.4 Monolayer Collisions

The execution of this calculation in the TRIM takes into consideration collision in each monolayer of the target material. The result of this calculation includes mean range, ionization and damage cascade.

2.4.4.3.5 - *Neutron / Electron / Photon Cascades*

The particle cascade option has input file, the TRIM.DAT which has the necessary

description of target surface for the initiation of recoil cascades. TRIM code takes these description and calculates the defects sustained on the target from the avalanche of collision. These types of calculations can be run in 3 modes: Full damage cascades; Full damage cascades and monolayer steps and the approximate calculations using the Kinchin-Pease (K-P) model for approximations.

2.4.4.3.6 *Various Ion Energy / Angle / Positions*

Ion energy /Angle /Positions makes evaluation of various energies of the ions with diverse trajectory angles of the target surface possible using the various depths in the target. Its application is vast and considers varying ion parameters such as Ion energy, angle and position of ion.

CHAPTER THREE: RESEARCH METHODOLOGY

The methodology employed in the determination of radiation damage effects by both neutron and gamma radiation on zircaloy-2, zircaloy-4, stainless steel type 308 and Eurofer 97 cladding materials which involved the use of computational codes MCNP5 and SRIM-TRIM codes. These codes are expounded upon in this chapter.

The MCNP5 simulation code was employed in the determination of the necessary neutron parameters such as the neutron flux on each cladding material. This was followed by the simulation of the energy deposited on the cladding materials by the neutron flux. The above milestones were achieved by the modification of the input deck of the GHARR-1 Miniature Neutron Source Reactor which has embedded in its clad structure zircaloy-4.

The average energy deposited on the clad materials from the MCNP5 code was used for the simulation of gamma radiation damage on each cladding material in the SRIM-TRIM code. SRIM was for the estimation of projected range or depth of neutron and gamma penetration in each material. Transport of Ions in Matter (TRIM) was employed in the simulation of gamma radiation damage. This involved the estimation of vacancies created, ion distribution, displacement per atom (dpa) and the estimation of whether radiations lead to changing the material integrity to an amorphous (disordered) crystal structure. Finally, the analytical solution to the radiation damage on Zircaloy-4 clad material using both K-P and NRT models are carried-out in this chapter.

3.1 MCNP5 Simulation

Monte Carlo methods are a set of rules used in the calculation process for analyzing 3-dimensional, time dependent computational challenges using pseudo-random numbers. It is particularly suited for interaction of nuclear particles with materials. This method accommodates algorithms which are large enough to necessitate the use of digital computers. It gives results only specified by the user in the tally cards.

MCNP is a general 3-dimensional combinatorial geometry transport code which is used to evaluate neutron, electron or photon flux, current, charge or energy deposited, reaction rate, heating and so on. For this thesis which deals with neutrons, the energy regime lies between 10^{-11} MeV to 20 MeV (X-5 MCNP, 2003).

The input data created for the MCNP simulation contained the following:

- Definition of geometry
- Material description for choosing cross-sections.
- Specified location and nature of the neutron source.
- Tally specification.

3.2 MCNP Neutronic Calculations

The secret to Monte Carlo codes are largely built upon on the principle of pseudo sampling. There are basically two methods employed in Monte Carlo methods for resolving transport equations.

They are namely; Computer simulation of physical processes and Mathematical methods for numerical integration.

Computer simulation method is most appropriately used for collision physics tracking, tallying for specific outputs, just to mention a few whilst mathematical approach is

appropriate in random sampling techniques, variance reduction, convergence, calculating Eigen value (Booth, 1992). Monte Carlo method is chiefly used in solving integral problems such as the Boltzmann equation. In resolving the integral Boltzmann transport equation, the equation simulates the resultant events such as particle cascade and fission processes. Eigen value is a prerequisite for reactor physics and criticality calculations. The nature of the source models the arrangement of materials (Carter, et al., 1975). The time-dependent linear Boltzmann transport equation is represented below:

$$\psi(r,v) = \int \left[\int \psi(r,v) C(v \to v, r) dv + Q(r,v) \right] T(r \to r, v) dv \tag{3.1}$$

Where

$\psi(r,v) =$ Collision density

$Q(r,v) =$ Source term

$C(v \to v, r) =$ Collision kernel,

$T(r \to r, v) =$ Transport Kernel,

$$\text{Angular Flux} = \frac{\psi(r,v)}{\Sigma(r,v)} \tag{3.2}$$

$$\text{Scalar Flux} = \phi(r,|v|) = \int_{\Omega} \frac{\psi(r,v)}{\Sigma(r,|v|)} d\Omega, v = |v|\Omega \tag{3.3}$$

Source term for the Boltzmann equation

$$Q(r,v) = \begin{Bmatrix} S(r,v) \\ S(r,v) + \int \psi(r,v) F(v \to v, r) dv \\ \frac{1}{k} \int \psi(r,v) F(v \to v, r) dv \end{Bmatrix} \tag{3.4}$$

Where

$S(r,v) =$ Fixed source

$F(v \to v, r) =$ Creation operator (due to fission particle at (r, v) creates particles at (r, v)

$k =$ Eigen value

The Monte Carlo method makes assumptions in the Boltzmann equation.

These assumptions are;

- A homogeneously static medium
- Time-dependent system
- Markovian (thus the next event depends only on the current (r, v, E) event).
- Intra-particle interactions do not exist.
- Relativistic effects are not considered.
- No long range forces (Particles interact in a straight path between events).
- Particle reactions must be independent of material properties.

The particle histories after repeated substitution for ψ_k will give

$$\psi_k(p) = \int \psi_{k-1}(p).R(p \to p)dp \tag{3.5}$$

$$\psi_k(p) = \int \psi_0(p_0).R(p_0 \to p_1).R(p_1 \to p_2)...R(p_{k-1} \to p)dp_0...dp_{k-1} \tag{3.6}$$

Particles normally start from a source by creating a track. The track may then split into two for that one track at collision or the splitting surface where a second track is generated. These two tracks possess half the track weight of the first particle track. When the track attains (n, 2n) reaction, an additional track is created making three tracks. Particle tracks consider the component of the first particle during its history. The length of a track in a cell is useful in determining fluxes, energy fluence and energy deposition. Fluence, flux and pulse-height energy deposition is analyzed using the crossing surfaces. Criticality collision estimators and multiplication are calculated using collisions from the tracks (Foster, 1991).

For a cell with specified composition, the theory below is used in collecting collision along its track (X-5 MCNP, 2003). The occurrence of the first collision between l and $l+dl$ along its flight is given as;

$$p(l)dl = e^{\sum_t l} \sum_t dl \tag{3.7}$$

Where $\sum_t$ the macroscopic total cross section of the medium.

Setting ξ the random number on [0 1] to be

$$\xi = \int_0^1 e^{-\sum_t s} \sum_t ds = 1 - e^{\sum_t l} \tag{3.8}$$

It shows that

$$l = \frac{1}{\sum_t} In(1-\xi) \tag{3.9}$$

But, because the collision particle is distributed in the same manner as 1-ξ. Then, the expression may be expanded to;

$$l = -\frac{1}{\Sigma_t} In(\xi) \tag{3.10}$$

Having gone through the physics of how the code works below is the outline of the methodologies that are employed in the MCNP code.

3.2.1 MCNP (LEU) Input file

The LEU input data file of the Miniature Neutron Source Reactor designed for the Ghana Research Reactor -1 was modified to produce the flux of neutrons generation after 830 cycles at a criticality of 1.004 mk simulating 500000 neutron histories. The other control runs at similar neutron history for 500 and 700 cycles at the same criticality dumping the

first 30 cycles were added. The flux of neutrons on each cladding of the 344 fuel pins where ascertained as well as the flux of the clad in each of the ten concentric rings using the f4 tally at seven energies of $5.8e^{-8}$, $2.5e^{-7}$, $6.25e^{-7}$, $4.0e^{-6}$, $5.53e^{-3}$, $8.21e^{-1}$ and 20MeV respectively. Each fuel pin was sectioned into ten subdivisions: **4 7710 7720 7730 7740 7750 7760 7780 7790 -3** for more accurate results to be achieved.

The energy deposition of the flux of neutrons on the cladding of all fuel pins was determined. The energy deposition on each of the ten concentric rings was also determined. This was possible by using the f7 tally cards at similar energies of flux. A copy of the flux tallies will be found in the Appendix I. The output files of the MCNP5 simulation run in the Femi-lab of the Argonne National Laboratory (ANL, 2016).

3.2.2 Working principle of MCNP Simulation tool

The MCNP program like other computational codes has a specific and particular trait and attribute that serves as requirement for successfully running a problem. These features are necessary in understanding the principle and manner in which the program is executed. Below are elucidations on a number of features used in the MCNP code.

3.2.2.1 Nuclear Data and Reactions

The essential source of data employed in running the MCNP5 program are expressions obtained in the Evaluated Nuclear Data File (ENDF) system, Advanced Computational Technology Initiative (ACTI), data from the Nuclear Physics (T-16) group at Los Alamos (Rose, 1991). Nuclear data libraries are written in a language that is easily understood by

MCNP. This increases the chance of retaining most details from the original evaluations in order to reflect the intent of the user (MacFarlane, 1982).

The Nuclear data libraries are tabulated for interactions of neutron, neutron - photons, particle interactions and thermal scattering (α, β). These data tables accessible to MCNP are cataloged on directory file XSDIR. ZAID is the distinct identification used for finding data. In this thesis work, the neutron data table was specifically used for the cladding materials under study.

Reaction rates can be determined when cross-sections are used as energy-dependent response functions. The Nuclear data also considers reactions involving molecular binding and crystalline effects. This becomes relevant when the neutron's energy get sufficiently low. Nuclear data takes into account information on the type of moderator, reflector materials such as beryllium metal, graphite, and other metals such as beryllium oxide, benzene, polyethylene, zirconium and hydrogen in zirconium hydride at varying temperatures (MacFarlane, 1982).

3.2.2.2 Source Specification

The user is obliged to specify the source of neutron, electron or photon for MCNP program. One has a vast array of choice of source to use. A source variable of energy, time, position, direction may be appropriate for an independent stochastic distribution (X-5 MCNP, 2003). This is also specified for other parameters like starting cells or surfaces. Some built-in functions for fission and fusion energy spectra have been made available.

Source specification allows decoupling of calculations into several regions simultaneously without running the problem for each region separately.

For a fission source, criticality source is used to estimate k_{eff}. The Table 3.1 below shows the description of a fission source.

Table 3.1: Description of Mnemonics used in the Data Card to estimate k_{eff}.

Mnemonics	Descriptions
K_{code}	Card name for criticality calculation.
nsrck	Neutrons per cycle.
rkk	Initial k_{eff}.
ikz	Cycles dumped before accumulating data.
k_{ct}	Cycles to run.
K_{src}	Card name for initial fission source location

3.2.2.3 Tallies and Output

The MCNP output on a large scale depends on the tallies used. These tallies relate to particle current, flux and energy deposition. But for criticality sources, these are tallies normalized for each particle from inception. Current is tallied as dependent on direction across surfaces, segments or sum of surfaces.

Fluxes are taken across surfaces, segments, in the cell, cell segments and sum of surfaces. Fluxes are also taken at assigned detector locations as standard tallies with the F5 cards. Special tally such as the super imposed mesh tally is independent of the geometry to which the user tallies a particle on a mesh. Energy deposition is also specified for particular cells

for the heating and fission. The energy distribution created in the detector by pulses of radiations is provided by the pulse height tally.

The tally results can be presented graphically except for the mesh tallies. These graphical representations could be generated while the code still runs or separately in a post processing mode. Below is Table 3.2 of tally mnemonics with their various descriptions.

Table 3.2: Tally Mnemonics and meanings.

Tally Mnemonic	Description
F1:N/ F1:P/ F1:E	Current of surface
F2:N/ F2:P/ F2:E	Flux of surface
F4:N/ F4:P/ F4:E	Track length
F5a:N/ F5a:P	Flux at a point
F6:N/ F6:P/ F6:N,P	Track length on deposited energy
F7:N	Track length on deposited energy
F8:P/ F8:E/ F8:P,E	Pulse-energy distributed in a detector

3.2.2.4 Estimation of Monte Carlo Errors

The tally and its second moment are the quantities used for error estimation R. This error estimation is evaluated for every complete Monte Carlo history.

The error estimate is expressed as $1/\sqrt{N}$ and N represents the histories. The true results of the simulation could be related to the calculated relative error which is evaluated to give

the confidence intervals of the estimated mean. The confidence statement made based on the results relies entirely on the precision of the Monte Carlo calculations. Table 3.3 shows the error estimation (R) values and their interpretations.

Table 3.3: Guidelines for Interpreting the Relative Error *R*.

Range of R	Quality of Tally
0.5 - 1.0	Unreliable
0.2 - 0.5	Factor of a few
0.1 - 0.2	Doubtful
< 0.10	Reliable
< 0.05	Reliable confidence interval

$$R = S_{\bar{x}} / \bar{x} \tag{3.11}$$

Where $S_{\bar{x}}$ - Standard deviation of the mean, $\bar{x}$ - estimated mean

The Figure of Merit serves as means for quality assurance by the code in ensuring that the output has a good confidence factor. It is printed out in the tally chart found in the output file. *FOM* can be expressed in the form:

$$FOM \equiv 1/(R^2 T) \tag{3.12}$$

Where T - Computer time in minutes; R - Relative Error;

The efficacy of the MCNP calculation is directly proportional to the FOM, which implies the larger the FOM the better the results.

3.2.2.5 Kinchin-Pease Model Evaluation

$$N = \frac{\Lambda \overline{E_n}}{4E_d} \tag{3.13}$$

N = Number of displacement per atom for each collision

E_d = Displacement energy

$\overline{E_n}$ = Interacting energy

$$\text{dpa} = \left[\frac{\dot{N}_d(E) \cdot t}{N}\right] \approx \left[\Phi(E).t\right] \cdot \frac{\sigma_s(E)}{AE_d}E \tag{3.14}$$

3.2.2.6 Norgett-Robinson Torrens model Evaluation

$$V_{NRT} = 0.8\frac{E}{2E_d} \tag{2.12}$$

$$k_{NRT} \cong \phi_t \frac{\sigma_S(\overline{E}_n)}{5E_d}\Lambda\overline{E}_n \tag{2.28}$$

V_{NRT} = Displacement per atom

k_{NRT} = Rate of displacement per atom

3.3 Assessment of Nuclear Parameters

3.3.1. Neutron Fluence

The neutron fluence was evaluated in the MCNP Simulation code using the equation

$$\text{Neutron Fluence} = \iint \phi(r,E,t)dEdt \tag{3.15}$$

$\phi(r,E,t)$ represents the neutrons flux integrated over the entire energy and time. The analysis was carried out considering the fact that neutron fluence represents particle-track lengths per unit volume. Furthermore, $\frac{WT}{V}$ was tallied with a cell for all particle-tracks within the stipulated energy and time range. W is the particle weight, T is the track length taken as the product of the time taken and velocity and V is the volume of the cell (Ziegler, et al., 2008).

3.3.2 Normalization factor

The conversion factor used was

$$\left(\frac{1J/s}{W}\right)\left(\frac{1MeV}{1.60205E-1}\right)\left(\frac{fission}{180.88MeV}\right) = 3.450908E+10\frac{fission}{Ws} \tag{3.16}$$

The source strength of the reactor is evaluated using the factor 3.450908E+10P (W) where, P represents reactor power in Watts. At steady state, the number of neutrons/fission (ν) is estimated as 2.4. The flux tallies were normalized with the expression below (Odoi, et al., 2011).

$$\frac{3.450908E+10*P(W)(\nu)*tally}{volume} \tag{3.17}$$

3.3.3. Energy deposition

The neutron heating value represents the total energy deposition within the volume of a cell in MeV/g. F7 gives an estimation of the heat of fissionable materials, that is only achievable in a physical experiment with no photons while those generated from fission are immediately captured. Actual heating could be estimated as a sum of the neutron and photons in the F6 tallies. F6 estimates the energy of materials considered as light in an experiment when photons are captured from the structure in a neutron-problem.

The relation below was used for the estimation of fission energy deposition in each cell in the MCNP5 code with the help of F7 tally:

$$F7 = \frac{\rho a}{\rho g V} \iiint Q(E)\sigma(E)\phi(r,E,t)dEdtdV \qquad (3.18)$$

Where V = volume,

σ (E) = microscopic cross-section,

Q (E) = fission Q-value and

ϕ (r, E, t) = neutron flux

All parameters undergo triple integration under the limits of energy and time. F7 scores fission energy deposition was expressed as $W\,T1Q\,\sigma_f(E)\frac{\rho a}{\rho g V}$ and was therefore available for neutrons.

In the MCNP5 neutron simulation, F7 energy deposition is delivered locally with photons from fission captured instantaneously. For F6 gamma heating was delivered somewhere and the photons were traced. Afterwards the actual heating is determined by merging neutron and photon tallies in a coupled neutron/photon calculation, the F6: N and Photon tally (Ziegler, et al., 2008).

3.4 Damage assessment by SRIM – TRIM CODE

3.4.1 Input data for stopping range of ion in matter (SRIM)

Gamma radiations are emitted at high energies during fission. These energies propel them from the fuel meat to interactions with the cladding materials. For each cladding material, SRIM was used to evaluate the energy required for atomic displacement by the gamma radiation using Cobalt-60 which is a gamma source. Table 3.4 represents the ion data parameters for the gamma source.

Table 3.4: Ion data input parameters used in the SRIM Code.

Ion Data	**Details**
Incident Ion name	Cobalt
Symbol for the incident ion	Co
Atomic number	27
Atomic mass	58.93 amu
Density	8.9 g/cm^3
Ion lower energy	10 keV
Ion higher energy	10,000 keV

The Ion data table above describes the details of the incident particle: Cobalt-60. The following tables below represent the target data parameters for each cladding material under study. Cobalt-60 serves as Ion data parameter of gamma radiation for all cladding materials used in the SRIM code.

Table 3.5: Target data parameters for **Zircaloy-4** used in the SRIM Code.

Target data	**Details**
Target description	Co in Zr-Sn-Fe-O- Cr
Target density	6.498 g/cm^3
Zirconium	91.22 amu
Tin	118.71 amu
Iron	55.847 amu
Oxygen	15.999 amu
Chromium	51.996 amu

Table 3.6: Target data parameters for **Zircaloy-2** used in the SRIM Code.

Target data	**Details**
Target description	Co in Zr-Sn-Fe-O-Cr-Ni
Target density	6.49951 g/cm^3
Zirconium	91.22 amu
Tin	118.71 amu
Iron	55.847 amu
Oxygen	15.999 amu
Chromium	51.996 amu
Nickel	58.69 amu

Table 3.7: Target data parameters for **Stainless steel type 308** used in the SRIM Code.

Target data	**Details**
Target description	Co in Fe-Cr-W-Mn-V-Ta-C
Target density	7.933 g/cm^3
Iron	55.847 amu
Chromium	51.996 amu
Tungsten	183.85 amu
Manganese	54.938 amu
Vanadium	50.942 amu
Tantalum	180.95 amu
Carbon	12.011 amu

Table 3.8: Target data parameters for **Eurofer 97** used in the SRIM Code.

Target data	**Details**
Target description	Co in Fe-Cr-Ni-Mn-Si-C-P-S
Target density	7.8296 g/cm^3
Iron	55.847 amu
Chromium	51.996 amu
Nickel	58.69 amu
Manganese	54.938 amu
Silicon	28.086 amu
Carbon	12.011 amu
Phosphorus	30.974 amu
Sulfur	32.066 amu

3.4.2 Input Data Parameter Window for SRIM

Figure 3.1: Data window for Cobalt- Zircaloy- 2 & 4 in SRIM Code.

Figure 3.2: Data window for Cobalt-Stainless Steel materials in the SRIM code.

Replicating the same analysis this time with the point of interest being neutrons represented as Helium atom. Below is Table 3.9 of the input parameter of He used in the SRIM Code.

Table 3.9: Ion data input parameters used in the SRIM Code.

Ion Data	**Details**
Incident Ion name	Helium
Symbol for the incident ion	He
Atomic number	4
Atomic mass	4.003 amu
Density	0.1259 g/cm^3
Ion lower energy	10 keV
Ion higher energy	10,000 keV

Figure 3.3: Data window for Helium-Zircaloy materials in the SRIM code.

Figure 3.4: Data window for Helium-Steel materials in the SRIM code.

The energy range of interest for this thesis work is between **0.9 - 10 MeV** for an appreciable projection range to revile much details. The results of the projection range determined from the SRIM code used are found in chapter four.

3.4.3 Transport of Ions in Matter (TRIM) Simulation Code

The TRIM code is used specifically to analyze the damage cascade into details on the cladding materials using the energy derived from the MCNP5 code. The energy is possessed by both neutrons and gamma radiation for the purposes of the study of radiation damage caused by either of the two. Therefore energy possessed by either neutron independently or gamma radiation independently is directed to the crystal structure of zircaloy-4 which is the material clad used in the MNSR (GHARR-1) reactor of the country. This is aimed at accessing the radiation damage for the purposes of boosting the approval

of the core convention from HEU with Aluminium cladding to LEU with zircaloy-4 cladding. Also, similar independent neutron and gamma radiation interaction with zircaloy-2, stainless steel type 308 and Eurofer 97 are estimated to ascertain their performance in relation or comparison to zircaloy-4 cladding material.

A full detailed calculation with the Full Damage Cascades option was selected as the damage type, to compute the defects created within the target atoms thus cladding materials in a total of 100 ions at energy of 9871.9KeV.

Every primary knock-on atom created as a result of the collision cascade ignited in the cladding materials were detected by the SRIM code and followed till it losses all its energy. Input data parameters used for the TRIM simulation exercise for ion data and target data for all cladding materials are indicated in the Tables 3.10 – 3.15 below.

Table 3.10: Ion (He) data input parameters used in the TRIM Code.

Ion Data	**Details**
Incident Ion name	Helium
Symbol for the incident ion	He
Atomic number	4
Atomic mass	4.003 amu
Density	0.1259 g/cm^3
Energy	9871.9KeV
Damage Type	Full Damage Cascades
Angle of incident	0

Table 3.11: Ion (Co) data and input parameters used in the TRIM Code.

Ion Data	**Details**
Incident Ion name	Cobalt
Symbol for the incident ion	Co
Atomic number	27
Atomic mass	58.93 amu
Density	8.9 g/cm^3
Energy	9871.9KeV
Damage Type	Full Damage Cascades
Angle of incident	0

Table 3.12: Target data (Zr-4) and input parameters used in the TRIM Code.

Ion Data	**Name/Value**
Layer name	Zircaloy-4
Symbol for the Target atom	Zr-Sn-Fe-Cr-O
Width	2.81μm /40.9 μm
Atomic Density	4.2824E+22 atom/cm^3
Displacement energy	25 eV
Lattice energy	3 eV
Surface binding energy	4.12 eV
Calculated Ions	100

Table 3.13: Target data (Zr-2) and input parameters used in the TRIM Code.

Ion Data	**Name/Value**
Layer name	Zircaloy-2
Symbol for the Target atom	Zr-Sn-Fe-Cr-O-Ni
Width	2.81μm /40.88 μm
Atomic Density	4.2854E+22 atom/cm^3
Displacement energy	25 eV
Lattice energy	3 eV
Surface binding energy	4.12 eV
Calculated Ions	100

Table 3.14: Target data (Fe-308) and input parameters used in the TRIM Code.

Ion Data	**Name/Value**
Layer name	Stainless Steel type 308
Symbol for the Target atom	Fe-Cr-W-Mn-V-Ta-C
Width	2.11μm /26.99 μm
Atomic Density	8.3775E+22 atom/cm^3
Displacement energy	25 eV
Lattice energy	3 eV
Surface binding energy	4.46 eV
Calculated Ions	100

Table 3.15: Target data (Eurofer-97) and input parameters used in the TRIM Code.

Ion Data	**Name/Value**
Layer name	Eurofer-97
Symbol for the Target atom	Fe-Cr-Ni-Mn-Si-C-P-S
Width	2.07µm /26.89 µm
Atomic Density	8.52775E+22 atom/cm^3
Displacement energy	25 eV
Lattice energy	3 eV
Surface binding energy	4.34 eV
Calculated Ions	100

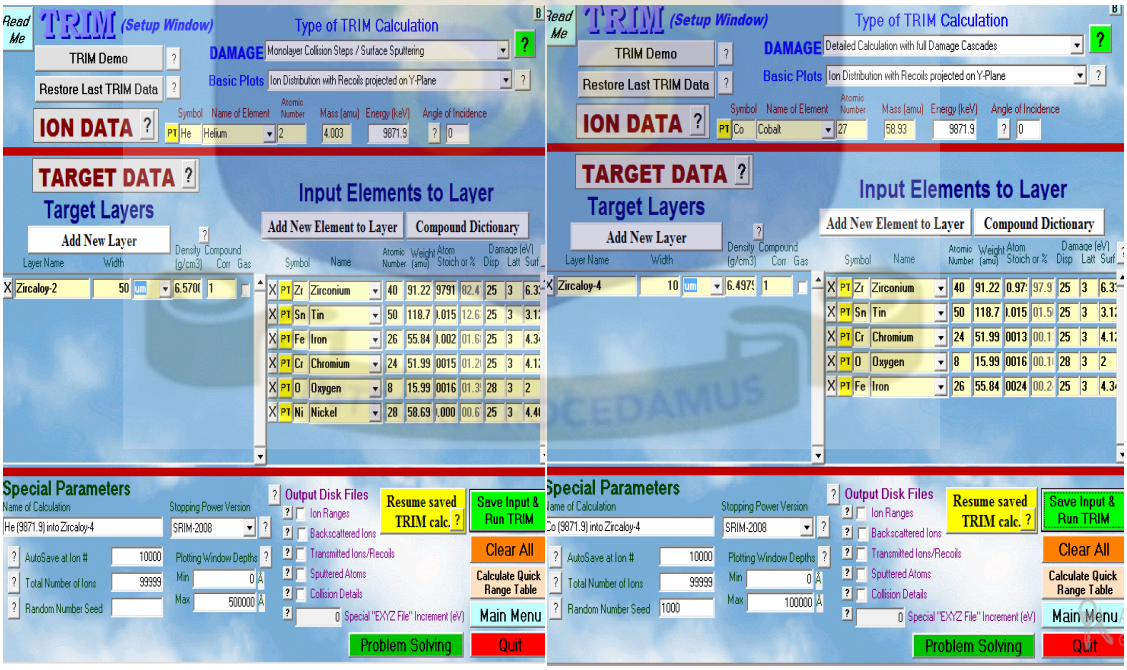

Figure 3.5: Data Windows for Zircaloy 2 & 4 in TRIM Code.

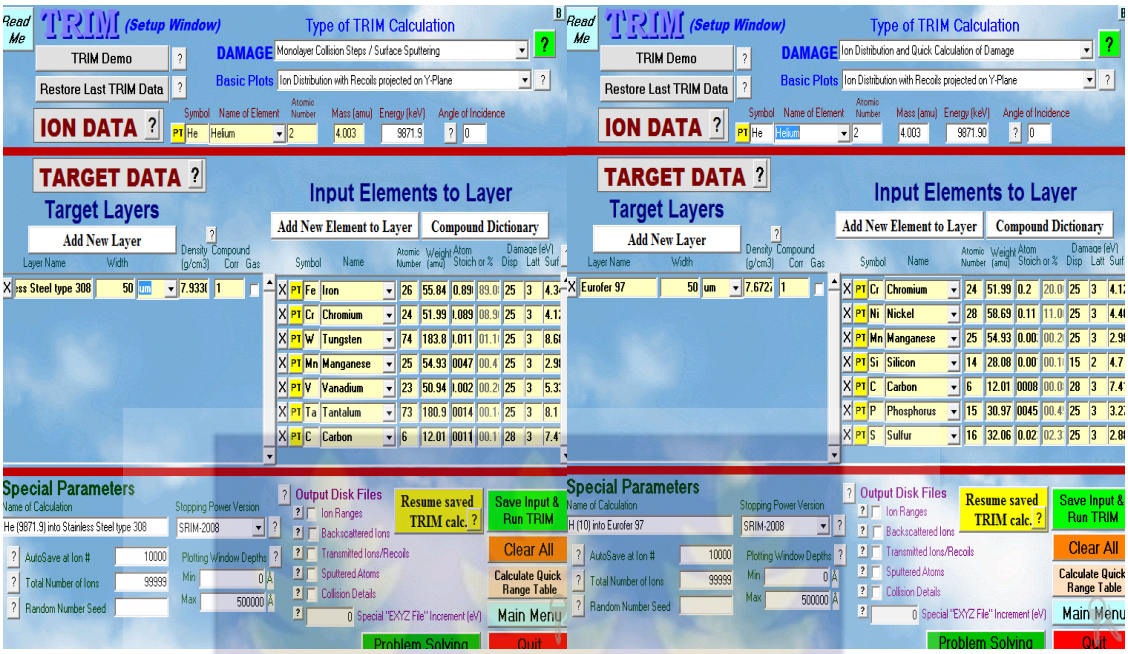

Figure 3.6: Data Windows for Stainless Steels & Eurofer 97 in TRIM Code.

After the simulations, using SRIM – TRIM Code, a number of output files on radiation damage as described in were produced. The result has been presented in Chapter Four.

3.5 Displacement Cascade Assessment

The SRIM-TRIM software evaluates the displacement cascade using the Kinchin – Pease (K - P) model. Where only binary collisions are considered but in actual sense a multitude of collision occur haphazardly with no regards to binary collision. The analytical approach used in this thesis considers the evaluation of the displacement cascade with the Kinchin – Pease (K - P) and Norgett – Robinson Torrens models. Therefore the K-P model is calculated again using the analytical approach. Additionally, the Norgett-Robinson Torrens model was also used to analytically calculate the displacement cascade.

The analytical solution for zircaloy-4 using Kinchin Pease and Norgett-Robinson Torrens models is carried-out concurrently. The solution considers collisions on the zircaloy-4 clad material which lasted averagely about 30 minutes from the TRIM analysis.

3.5.1 Kinchin-Pease Model

Zr [A= 90], E_n= 9.87188MeV, σ_{el} = 3b, ϕ (E_n) = 7.46 x 10^{13}n/cm^2.s, t = 1800s

E_d = 25eV

Where;

A = Mass number, E_n= Neutron Energy, σ_{el} = Elastic cross section, ϕ (E_n) = Neutron flux

E_d = Displacement Energy, R_d = Rate of atomic displacement, dpa = Displacement per atom.

$$\Lambda = \frac{4A}{(A+1)^2} = \frac{4x90}{(90+1)^2} = 0.04347$$

$$R_d = \frac{N\Lambda\sigma_{el}(\overline{E_n}).\phi(\overline{E_n})}{4xE_d}, \qquad \text{dpa} = \frac{R_d.t}{N} = \frac{N\Lambda\sigma_{el}(\overline{E_n}).\phi(\overline{E_n}).t}{(4xE_d)xN} = \frac{\Lambda\sigma_{el}(\overline{E_n}).\phi(\overline{E_n}).t}{(4xE_d)}$$

$$\textbf{dpa} = \frac{(0.04347)(3x10^{-24}cm^2)(9.87188x10^6eV)(7.46x10^{13}\,n/cm^2.s)(1800s)}{4x25eV}$$

dpa = 0.00172870980411024

$$\frac{\Lambda\overline{E_n}}{4.E_d} = \frac{(0.04347x9.87188x10^6eV)}{4X\,25eV} = 4291.306236 \text{ dpa per neutron collision}$$

3.5.2 Norgett-Robinson Torrens Model

$$NRT = \frac{0.8\overline{E_n}}{2E_d} = \frac{0.8x(9.87188x10^6 eV)}{2x25eV} = 157950$$

The displacement per atom using the NRT Model is computed as follows;

$$V_{NRT} = \frac{\Lambda\overline{E_n}\sigma_{el}(\overline{E_n}).\phi(\overline{E_n}).t}{5xE_d} = \frac{(0.04347)(3x10^{-24}cm^2)(9.87188x10^6 eV)(7.46x10^{13}\, n/cm^2.s)(1800s)}{5x25}$$

V_{NRT}= 0.00138296784328819**2** displacement per atom

CHAPTER FOUR: RESULTS AND DISCUSSIONS

The results obtained from the Argonne National Laboratory (USA) on the MCNP5 simulation of the (LEU) input deck of GHARR-1 research reactor is expounded upon in Section 4.1. Similarly, the outcome of the energy deposition (f7) is employed in the SRIM-TRIM code for the radiation damage assessment in all four clad materials. This elaboration is conspicuous in Section 4.2.

The output data from the MCNP5 simulation regarding the flux distribution on all 344 fuel pins are presented in the Appendix I. Thus, flux distribution for the three levels of energy on each clad. Also the output for the SRIM simulations are presented for energies between (**10KeV- 10MeV**) showing their respective projected range, longitudinal and lateral straggling.

4.1 Neutron Flux distributions

The neutron flux distribution over the Zircaloy-4 cladding material of all 344 fuel pins sectioned into **4 7710 7720 7730 7740 7750 7760 7780 7790 -3** for all three energy groups gave the following results.

Table 4.1: Average Normalized Neutron Flux in Zircaloy-4 at 34KW Power.

Energy group	Average Neutron Flux ($ncm^{-2}s^{-1}$)
Thermal	4.0896E+11
Epithermal	9.02759E+11
Fast	5.29667E+11
Total	1.84139E+12

The outcome of the MCNP5 simulation of the axial thermal, epithermal, fast and total normalized neutron fluxes for the 12.6% Low Enriched Uranium (LEU) UO_2 is shown in Table 4.1 above. The epithermal neutron flux showed a much higher flux compared to the fast and thermal neutron fluxes respectively. The total neutron flux gave the highest flux values. This behaviour of flux distribution is generally the trend in most simulations where the epithermal fluxes are higher than the fast and thermal respectively. Comparing the normalized average thermal flux achieved to that estimated by other works using the High Enriched Uranium at a data description of 500000 1.004 100 500 gave a flux of **3.179E+11** (Boafo, 2012). The 22% increment in neutron flux is attributable to the fact that the Low Enriched Uranium (LEU) core generates more thermal neutrons that undergo decay to produce more daughter nuclei for interactions. It is attributed to the fact that the zircaloy clad material has better conditions to sustaining more neutrons. It is also due to the fact that the flux of neutrons generated in this thesis work is after 830 cycles which is higher than that which was used in the HEU simulation.

4.1.1 Neutron flux distribution for the Lattice Rings

The Zircaloy-4 cladding material engulfs all the 344 fuel pins at the reactor core. The power house of the reactor (control rod) is conspicuously located at the center of the concentric rings with its stainless steel clad. The rest of the ten lattice positions left, serve other purposes which are not under study in this work.

The core has ten (10) concentric rings of fuel pins arranged in it. These concentric rings have in the center a control rod which controls neutron population upon its introduction or withdrawal. These ten lattice rings have a varying number of fuel pins in the order of **6 12 19 26 32 39 45 48 58 59**.

Table 4.2 below shows the output of the MCNP5 simulation representing the normalized average flux of neutrons in all the ten lattice rings. Normalized fluxes refers to flux values that have been normalized with the generally known normalization factor $\left(\frac{1J/s}{W}\right)\left(\frac{1MeV}{1.60205E-1}\right)\left(\frac{fission}{180.88MeV}\right) = 3.450908E+10\frac{fission}{Ws}$

Whereas the Average normalized flux refers to the average of the normalized flux for each lattice which has a specific number of fuel element.

Table 4.2: Normalized and Average Normalized Neutron Flux in Ten Lattice Ring.

Thermal flux	Average	Epithermal Flux	Average	Fast flux	Average
9.24E+11	1.54E+11	2.45E+12	4.08E+11	1.32E+12	2.20E+11
1.79E+12	1.49E+11	5.57E+12	4.64E+11	3.13E+12	2.61E+11
2.94E+12	1.55E+11	9.51E+12	5.01E+11	5.41E+12	2.85E+11
4.23E+12	1.63E+11	1.40E+13	5.38E+11	7.93E+12	3.05E+11
4.81E+12	1.50E+11	1.58E+13	4.94E+11	8.97E+12	2.80E+11
5.75E+12	1.47E+11	1.88E+13	4.82E+11	1.06E+13	2.72E+11
6.10E+12	1.36E+11	1.95E+13	4.33E+11	1.09E+13	2.42E+11
5.72E+12	1.19E+11	1.78E+13	3.71E+11	9.76E+12	2.03E+11
6.11E+12	1.05E+11	1.71E+13	2.95E+11	9.32E+12	1.61E+11
7.86E+12	1.27E+11	1.36E+13	2.19E+11	7.24E+12	1.17E+11

From Table 4.2, it is obvious that the normalized flux in all three energy group recorded higher neutron flux values than the average normalized neutron flux estimated for each fuel pin. This observation is attributable to the fact that Normalized flux values are

representative of the whole ring or lattice whilst the Average normalized flux values are representative of each fuel element in the lattice or ring.

There is a general increase in the flux values for the three energy groups from the first lattice ring to the last lattice ring. However, there appears to be a decline in the average normalized neutron flux for all the three energy groups in varying ways. The normalized average fast neutron flux shows a more continuous decline in flux. This is followed by the normalized average epithermal neutron flux and lastly the normalized average thermal neutron flux registering a more distorted decline.

The graph below demonstrates the variation in the normalized flux distribution for the three energy groups (levels) in the ten concentric lattice rings.

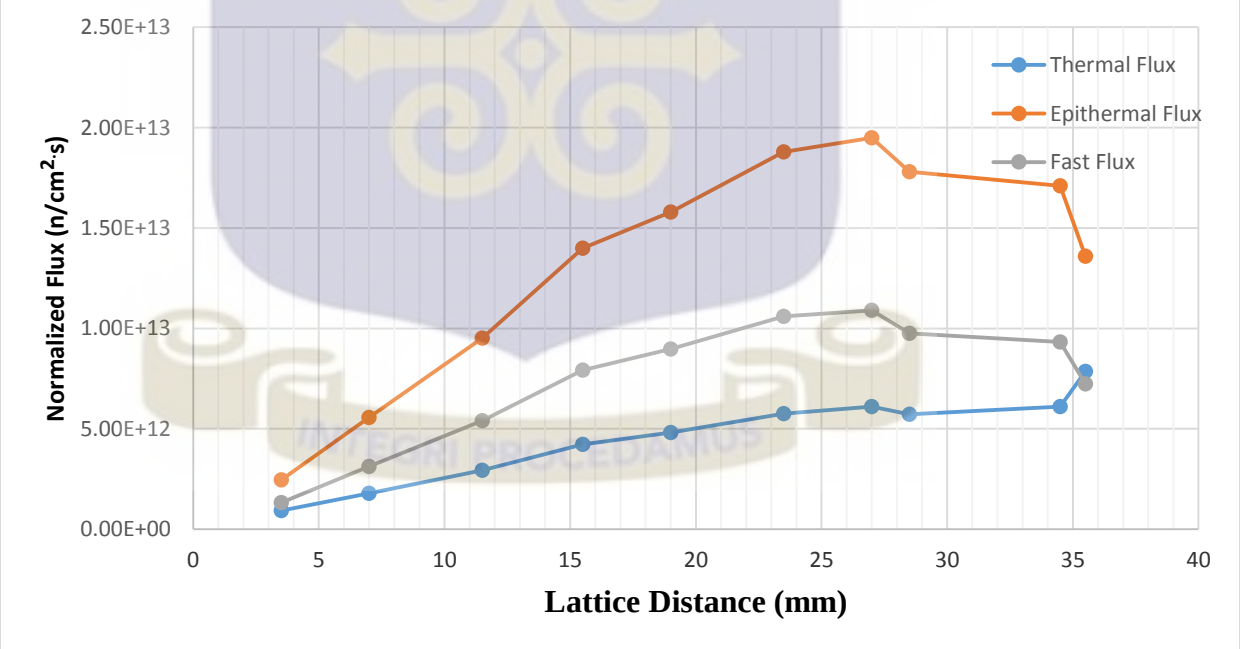

figure 4.1: A graph of Normalized neutron flux against Lattice distance.

For a true reflection of neutron flux in the individual lattice rings, the graph in figure 4.2 exhibits the normalized average neutron flux distribution for all the three energy levels (groups). The specific number of fuel pins in each ring were taken into consideration.

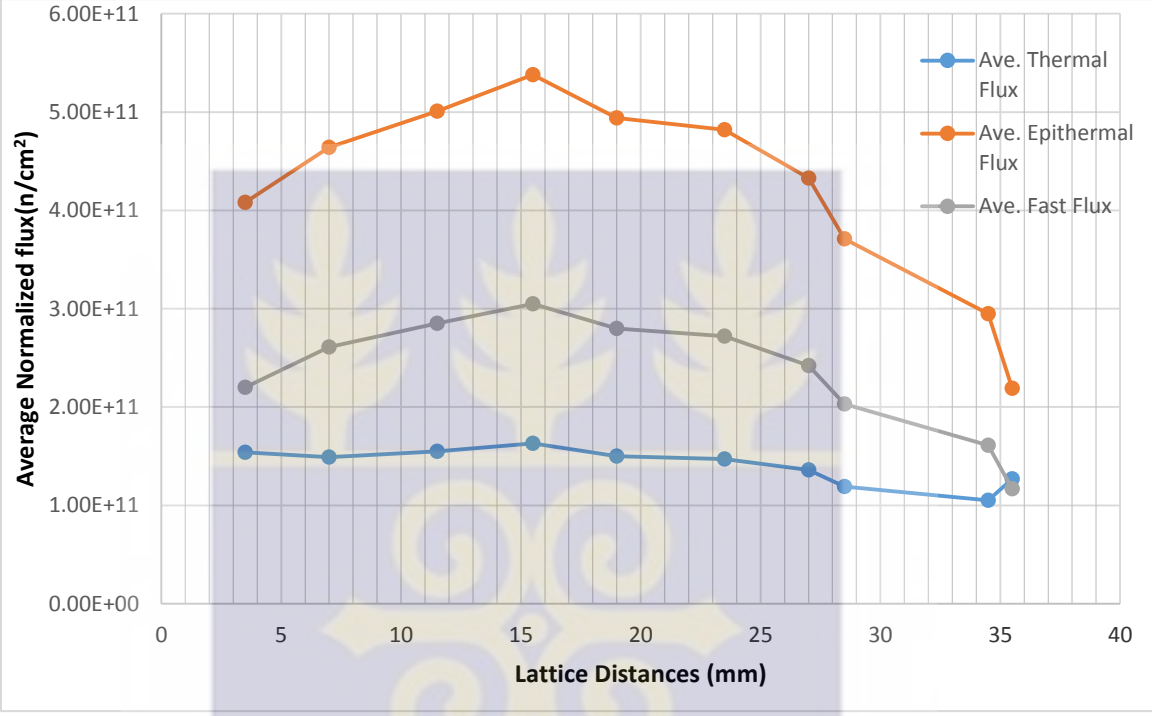

figure 4.2: A graph of Normalized average neutron flux against Lattice distance.

For the purposes of this thesis work, the fast neutron energy group is known from literature to be responsible for causing majority of radiation damage in materials. For this reason, the normalized fast neuton flux of **7.46E+13n/cm^2.s** in all ten concentric rings is employed for the radiation assessment. Comparing the normalized thermal neuton flux of **1.41E+12 n/cm^2.s** from this thesis to **(9.8±0.0017)E+11 n/cm^2.s** of thermal neutron flux from the inner irradition channel using the same code shows good trend (Odoi, et al., 2011).

4.1.2 Neutron Energy deposition

The neutron heating value from the MCNP5 output represented with the F7 tally card in the input deck is given in Table 4.3. The energy deposition is estimated for each lattice ring.

Table 4.3: Neutron energy deposition in Lattice rings.

Lattice Ring	Lattice distance (mm)	Energy(MeV)
A	3.5	1.83932
B	7	3.67863
C	11.5	5.8245
D	15.5	8.27692
E	19	9.50313
F	23.5	7.31204
G	27	13.7949
H	28.5	14.7145
I	34.5	13.0047
J	35.5	20.7702
		9.871884

It is observed that, a general increase in the energy deposition is recorded as the position of the ring is moved further from the control rod. This increase is as a result of the increase

in neutron flux as was stated above. Neutron flux is directly proportional to the energy deposition.

The figure 4.3 below is a graph of energy deposition on the zircaloy clad in each concentric ring.

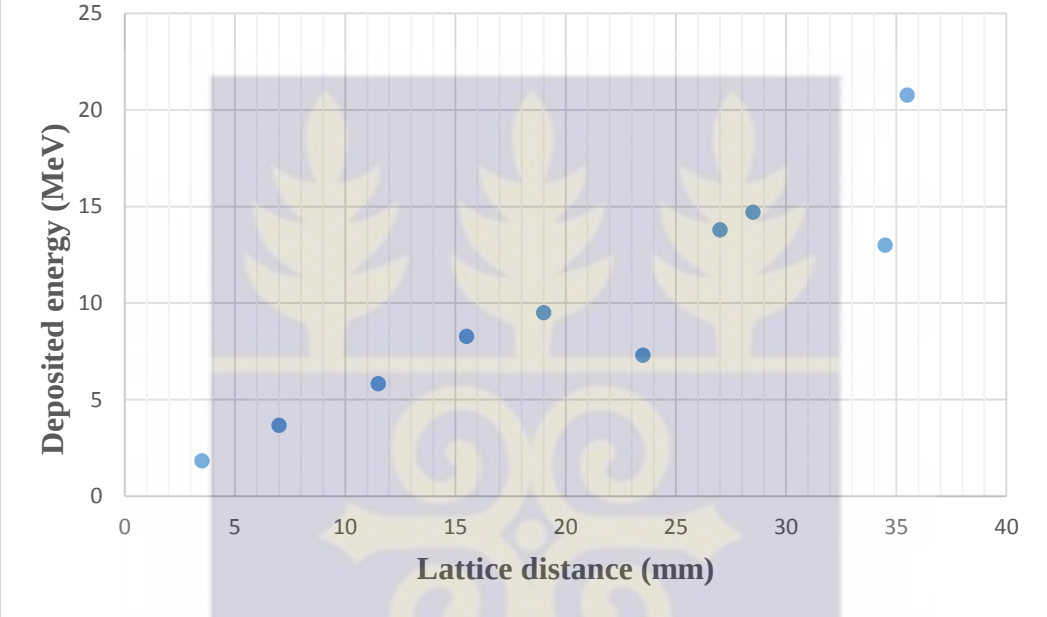

Figure 4.3: A graph of Energy deposition (MeV) Against Lattice distance (mm).

4.2 Damage Assessment by SRIM – TRIM Code

4.2.1 SRIM Calculations

The results of the projection range for all four clad materials from SRIM have been presented in this section. At the maximum energy of **10MeV** closest to the neutron energy deposited in the clad **9.871884MeV**, the projection range was taken. This is carried-out for both neutron and gamma interactions. The detailed output text files for SRIM analysis are shown in the Appendices. The results presented below are for both neutron and gamma interactions respectively.

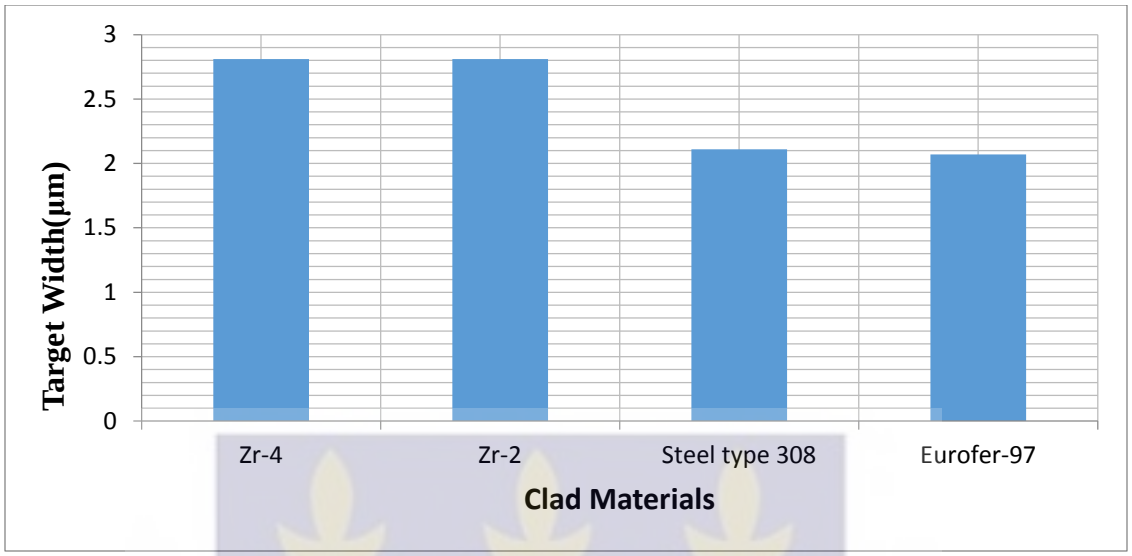

Figure 4.4: A graph of Projection Range of Clad Materials (Neutron Interaction).

For neutron interaction, both Zircaloy-4 and Zircaloy-2 have a targeted width of 2.81µm. At this width all much of the collision cascade details are reviled for both metals. Stainless steel type 308 registered 2.11 µm. Eurofer-97 had a targeted width of 2.07 µm though it has a higher density than the two zircaloy materials.

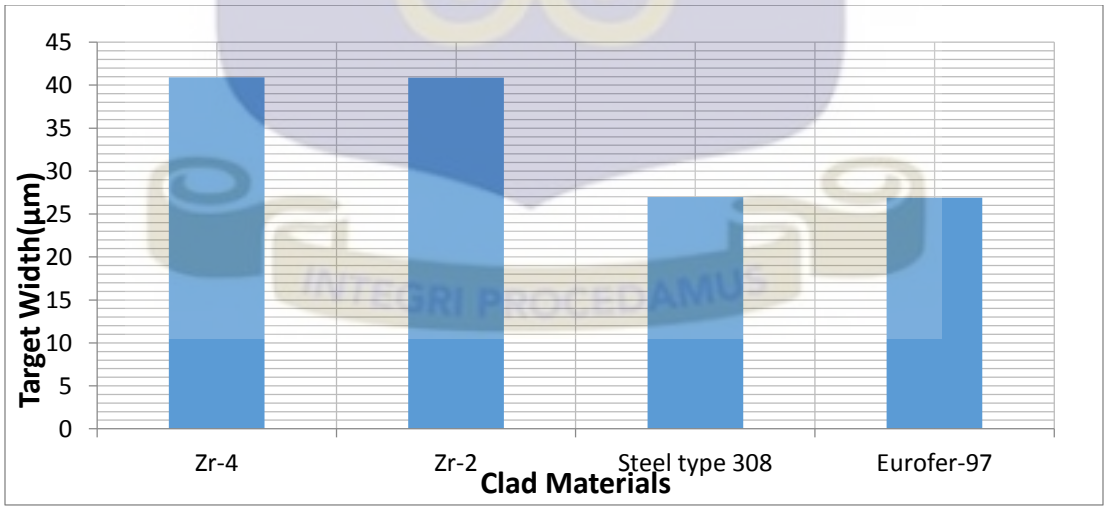

Figure 4.5: A graph of Projection Range of Clad Materials (λ-Interaction).

For Gamma interaction, similar trend of behaviour is seen this time at higher target width. Zircaloy-4 recorded the highest width at 40.9 µm and Eurofer-97 recording the least at

26.89 μm. The result is reasonable as it is known from literature gamma radiations are electromagnetic and travel long distance for interactions unlike neutrons.

4.2.2 TRIM Code Assessment

This section solely deals with the elucidations of the results from the full damage cascades calculation of the Transport of Ions in Matter (TRIM). The target width estimated for both neutron and gamma radiations are used as guide to achieving the results where collision is at its pinnacle. The simulation uses the energy deposition as determined from the MCNP5 code for the full damage cascade calculation for neutron and gamma interactions with all four clad materials. Our interest however is mainly with Zircaloy-4 clad material since it is the clad for the LEU core which has been proposed.

4.2.2.1 Full damage assessment of Zircaloy-4

The output of the damage cascade after 100 collisions of a gamma- beta particle (Co-60) with the Zircaloy-4 clad is shown below in fig. 4.6. The interaction generated 30356.2 vacancies.

Table 4.4: Percentage Energy distribution in Zircaloy-4 Target Material.

% Energy Loss	Ions (%)	Recoils (%)
Ionization	85.12	3.58
Vacancies	0.02	0.09
Phonons	0.08	10.29

The percentage of energy lost by the incoming ion to the target material is represented above in Table 4.4. This table shows the loss of energy from the ion as it interacts with the

target zircaloy-4 material. Not all vacancies created leads to primary radiation. The ions contribute 0.02% of its energy to vacancies whilst the recoil contributes 0.09%. This shows that the recoil contributes to the creation of vacancies more than the ions though only 3.58% of the energy was gained from the incoming ion. The recoil ions are therefore more susceptible to causing primary radiation.

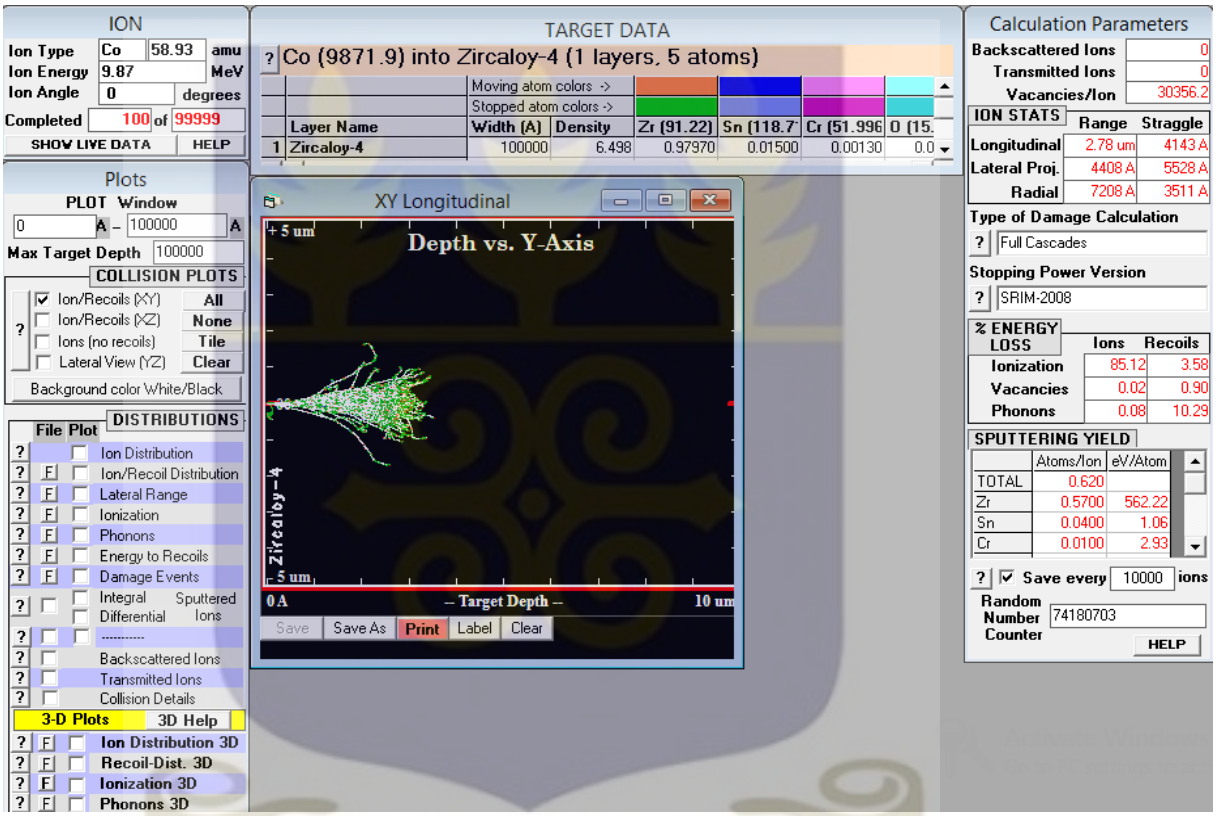

Figure 4.6: TRIM output for λ-Interaction with Zircaloy-4.

The Collision events in the figure below shows the vacancies created by virtue of the constituent atoms in the target alloy. It is clear most of the vacancies created where those of the zirconium metal which makes up about 98% of the entire material. Tin records some few vacancies with chromium and the other trace elements recording almost nil in terms of vacancies. The same trend is exhibited in sputtering.

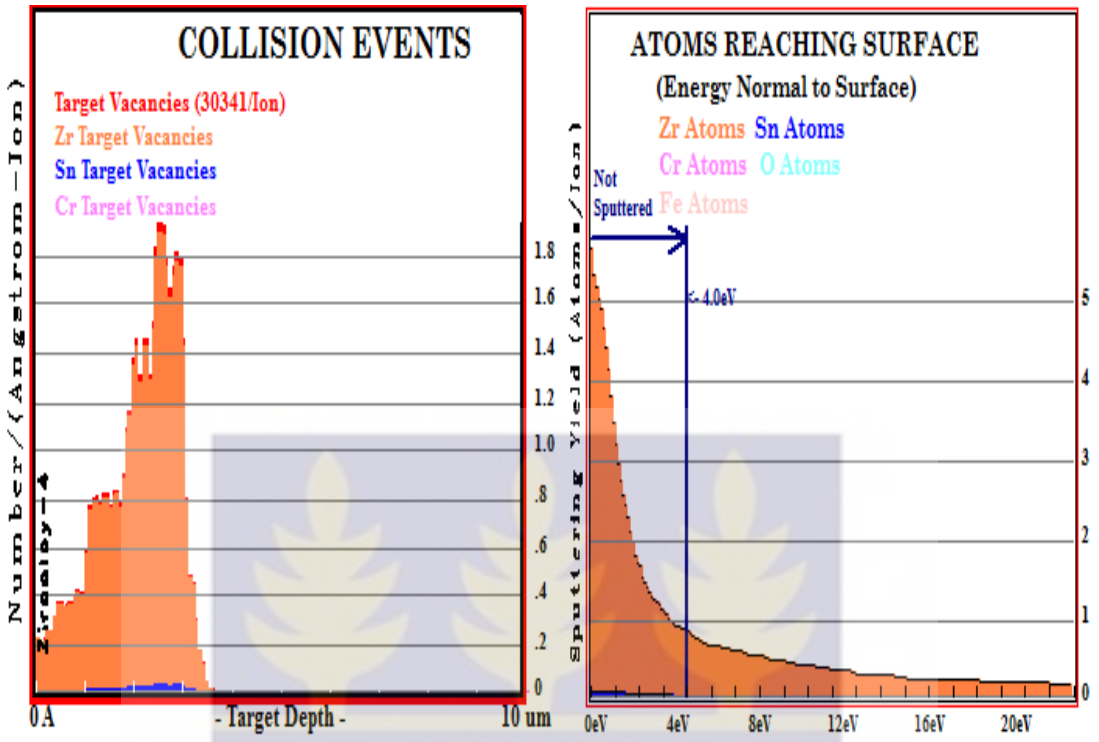

Figure 4.7: Atomic Displacement by Collision event and sputtering (Zr-4).

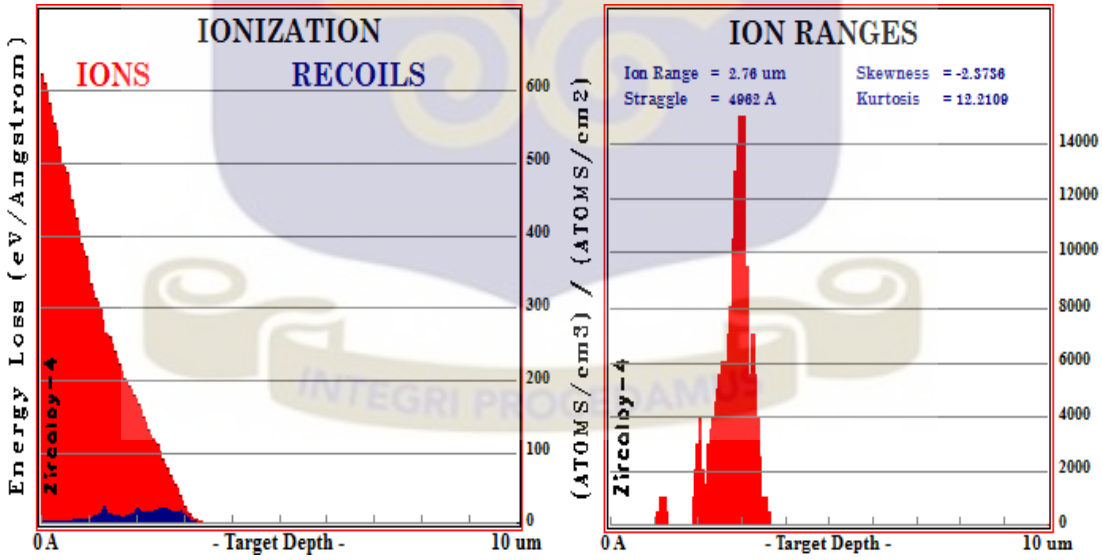

Figure 4.8: Illustration of Ionization and Ion Range in Zircaloy-4.

For the neutron interaction with zircaloy-4, a whole different behaviour ensues. The total number of vacancies recorded was 327 even after 1000 collisions. Only 0.01% of this was as a result of recoils generated.

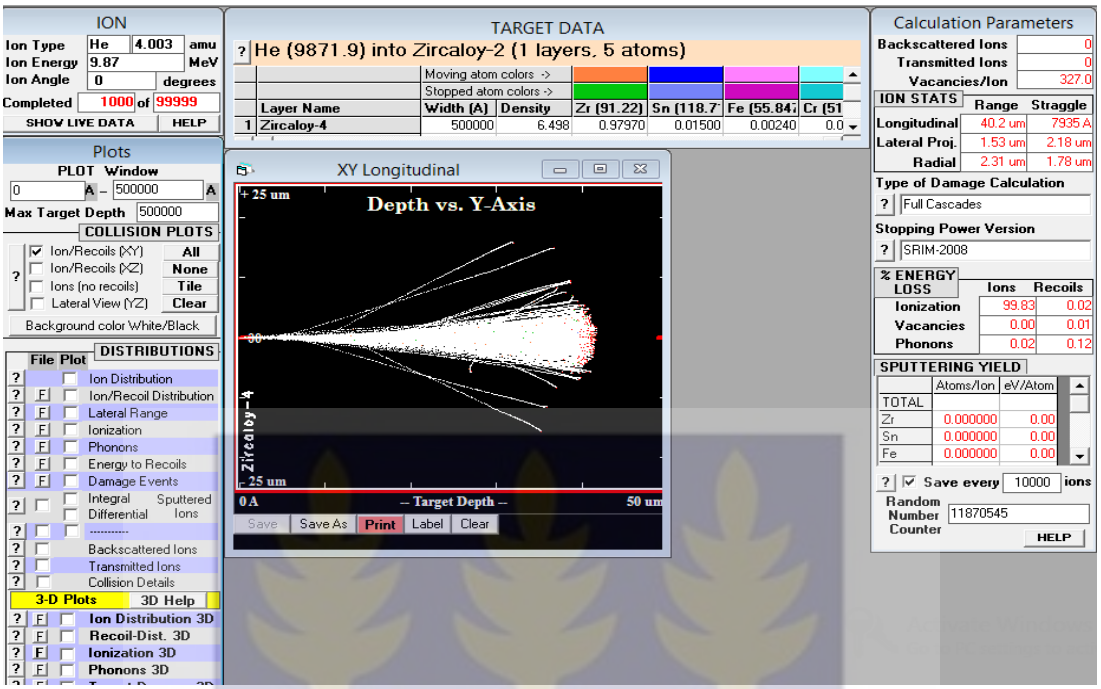

Figure 4.9: TRIM output for Neutron Interaction with Zircaloy-4.

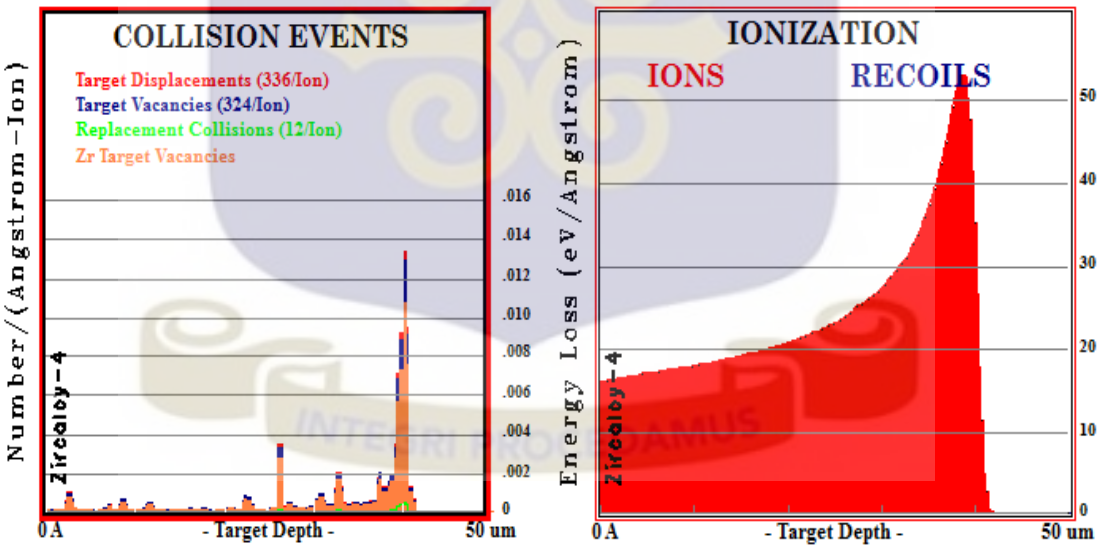

Figure 4.10: Atomic Displacement by Collision event and Ionization (Zr-4).

4.2.2.2 Full damage assessment of Zircaloy-2.

After 100 collisions of the Co-60 particles with Zircaloy-2, the results are provided below.

This table shows the contributions of ions and recoil ions in the interaction.

Table 4.5: Percentage Energy distribution in Zircaloy-2 Target Material.

% Energy Loss	Ions (%)	Recoils (%)
Ionization	84.72	3.55
Vacancies	0.02	0.94
Phonons	0.08	10.69

Zorcaloy-2 interaction with gamma generated 31569 vacancies. 0.94% of these vacancies created where as a result of recoil ions. This is greater than 0.09% recorded for zircaloy-4. This implies zircaloy-2 will generate recoils with more energy to cause vacancies that will lead to primary radiation.

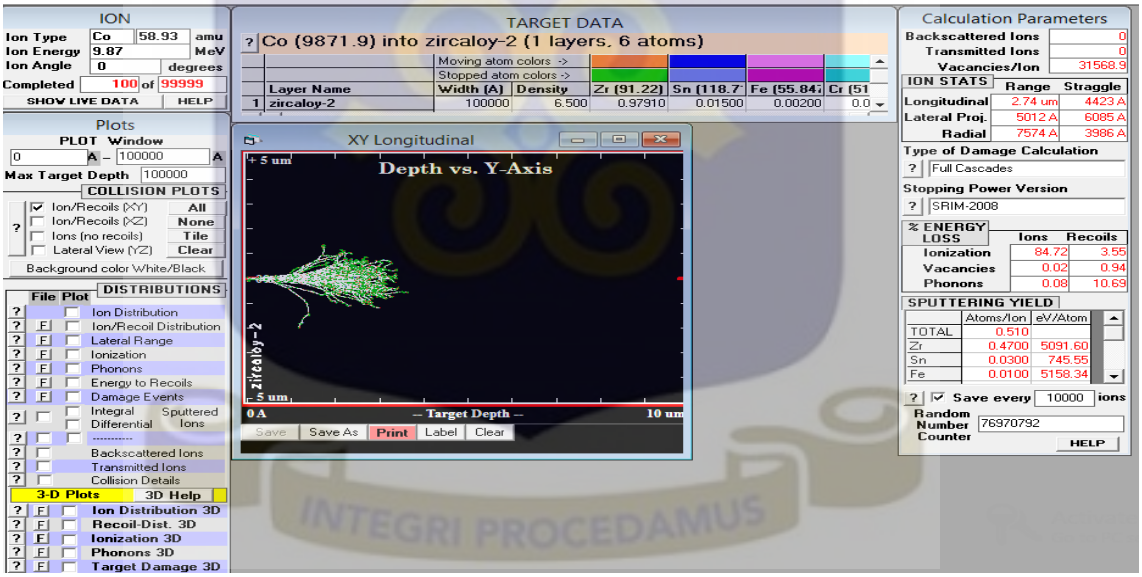

Figure 4.11: TRIM output for λ-Interaction with Zircaloy-2.

From the sputtering graph, zirconium experiences the most lost at energies between 4 - 20eV. Tin has a sputtering yield lower than 0.5. The collision event on the other hand, records 31533 vacancies and 1662 replacement collision. A 5.27% replacement collision.

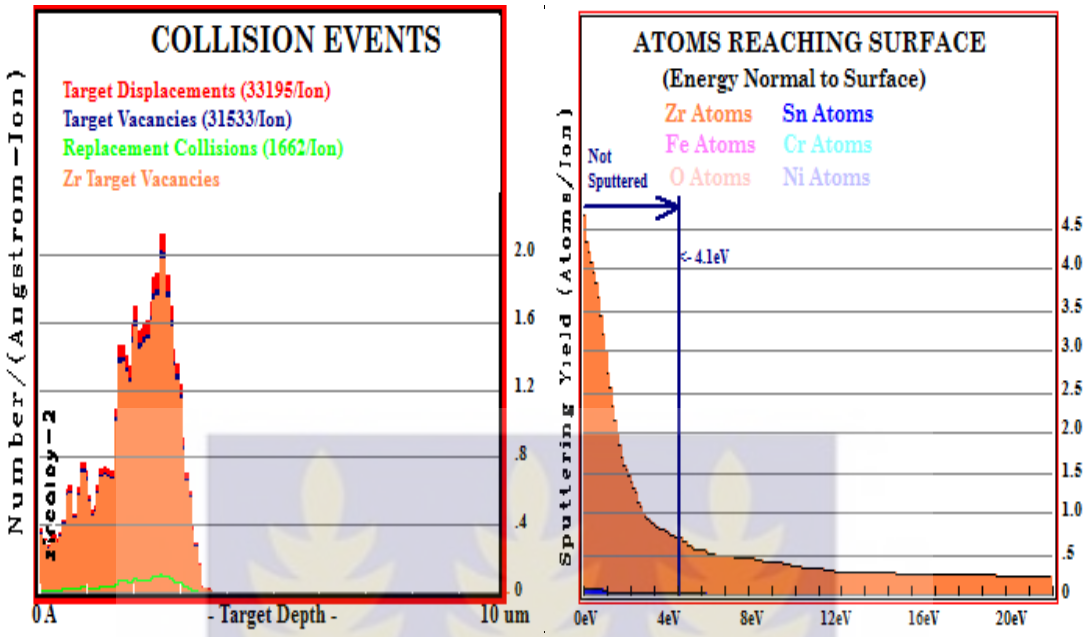

Figure 4.12: Atomic Displacement by Collision event and sputtering (Zr-2).

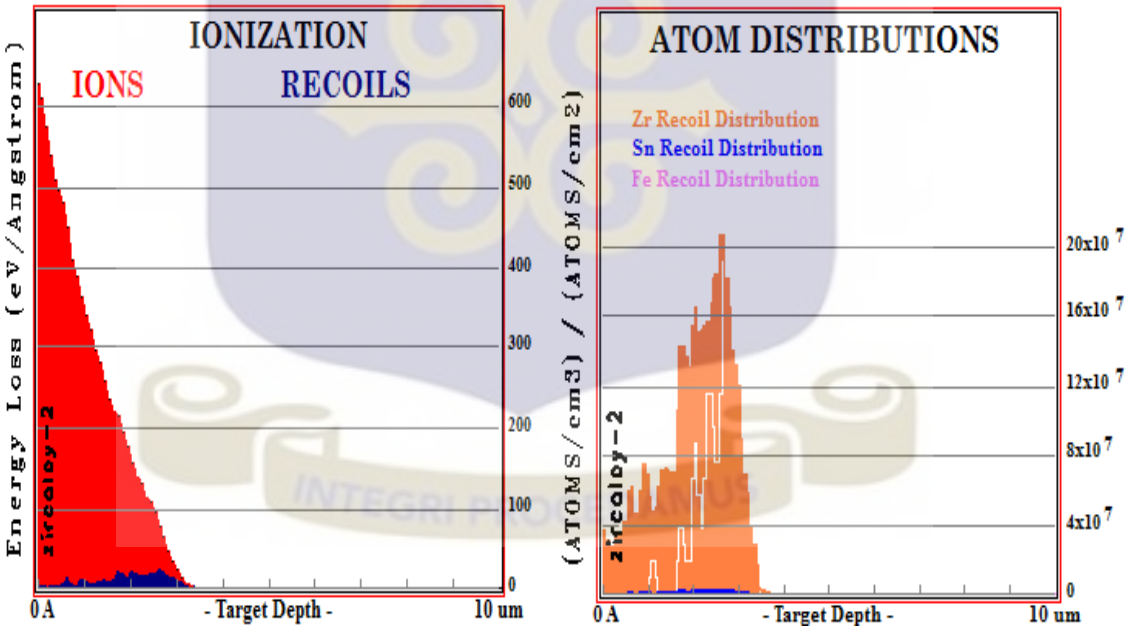

Figure 4.13: Illustration of Ionization and Ion Range in Zircaloy-2.

For neutron interaction, Zicaloy-2 experienced 348 displacements. 17 of these collisions resulted into replacement and the rest as target displacement. Below is a representation of the assessment made using the simulation for neutron interactions.

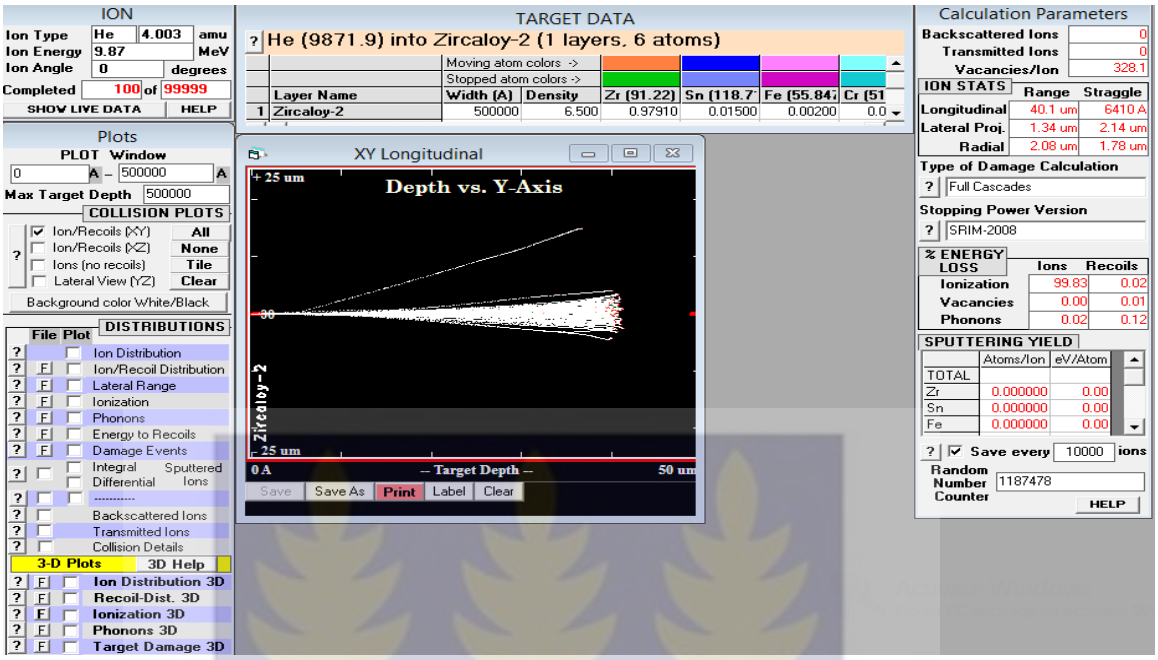

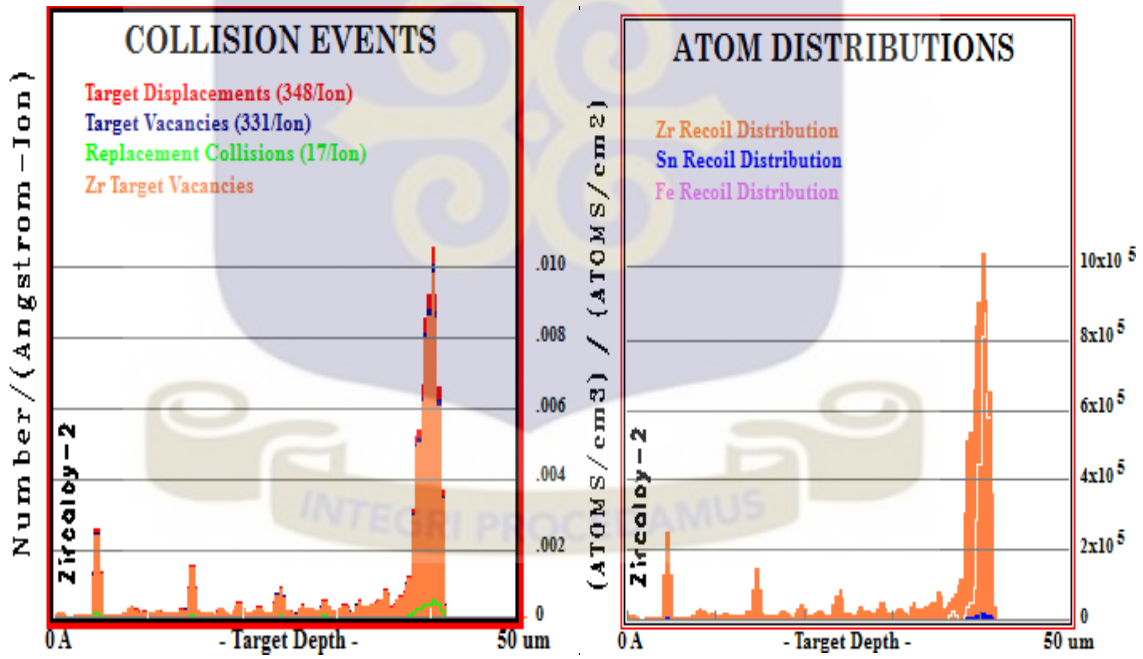

Figure 4.14: Damage Assessment by TRIM on Zircaloy-2 (Neutron Interaction).

4.2.2.3 Full damage assessment of Stainless Steel type-308

The full damage cascade results for 100 collision of the Co-60 particle with Stainless steel type 308 are given below. Table 4.6 shows the contributions of ions and recoil ions in the interaction.

Table 4.6: Percentage Energy distribution in Stainless steel type-308 Target Material.

% Energy Loss	Ions (%)	Recoils (%)
Ionization	83.71	5.38
Vacancies	0.02	0.97
Phonons	0.11	9.8

Stainless steel type-308 interaction with gamma generated 32860 vacancies. 0.97% of these vacancies created where as a result of recoil ions. This is comparatively greater than that of zircaloy-4 and zircaloy-2. Since recoil atoms are susceptible to causing primary radiation, a great deal of vacancies, interstitials and other defects are created in Stainless steel type 308 than will be created in zircaloy 2 and 4. They also recorded higher number of vacancies than zircaloy 2 and 4.

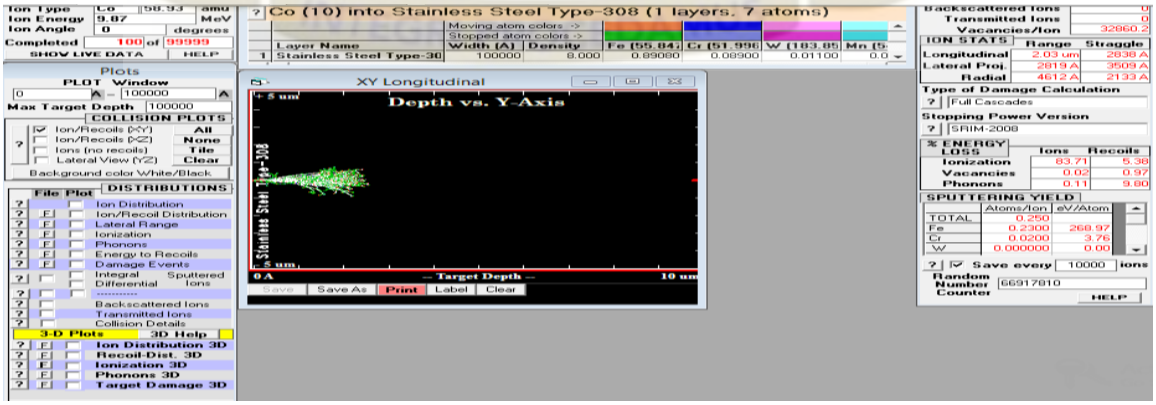

Figure 4.15: TRIM output for λ-Interaction with Stainless steel type-308.

From the collision event, 34637 displacements were recorded in the steel. Almost the same for vacancies created with about 1890 replacement collisions ensuing. As much as 5.77% of the vacancies recorded resulted into replacement which means more defect generation. The sputtering of Iron and Chromium was relatively very high. This means reduction in material thickness.

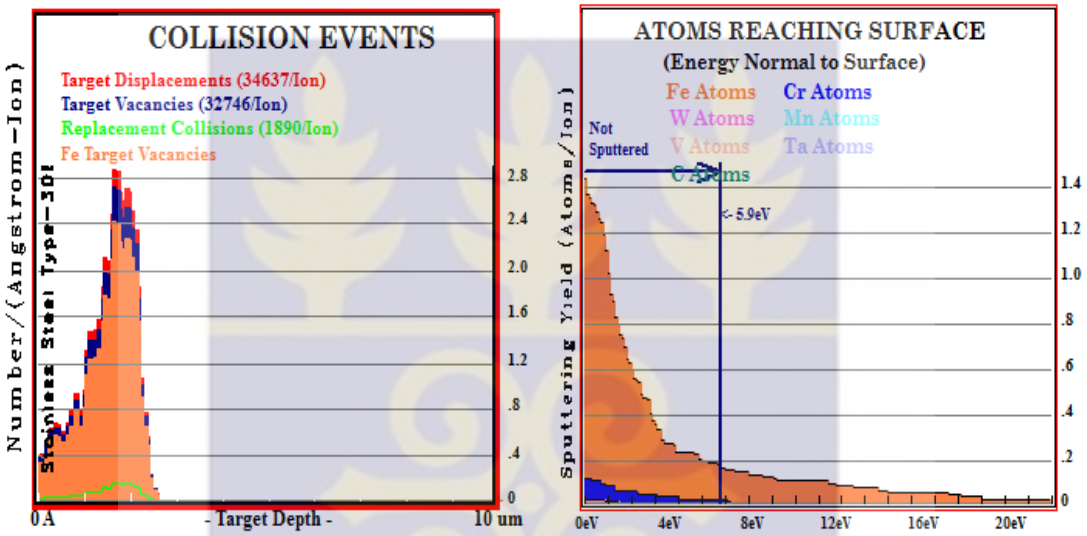

Figure 4.16: Atomic Displacement by Collision event and Sputtering (Steel type-308).

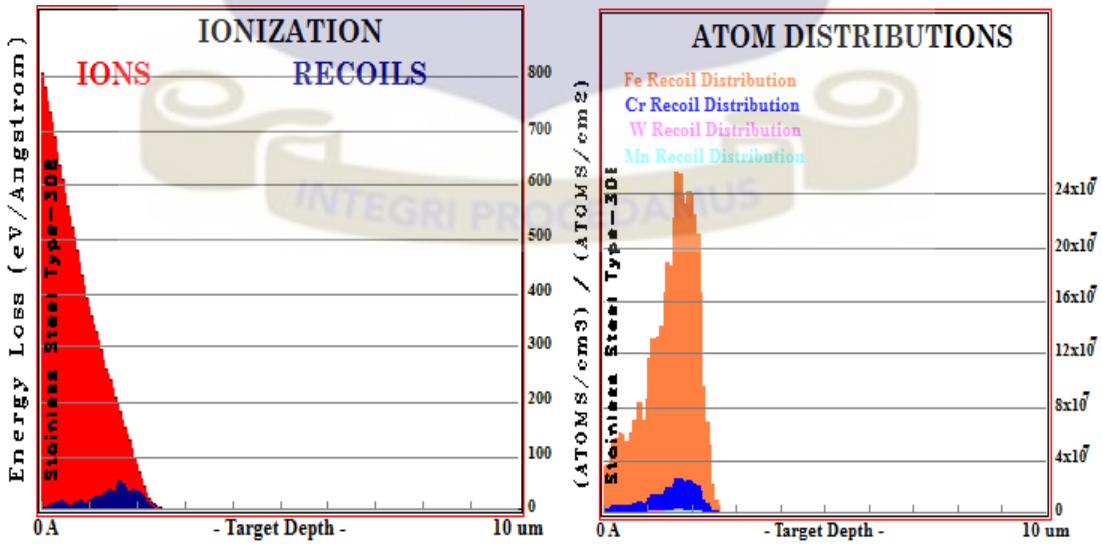

Figure 4.17: Illustration of Ionization and Atom distribution (Steel type-308).

For neutron interaction, a total of 415 vacancies were created. This is much lower than that recorded for gamma interaction. In comparison to that recorded for neutron interaction with zircaloy 2 and 4, this number of vacancies far exceeds those of zircaloy 2 and 4. After 1000 collisions, only 327 vacancies were recorded in zircaloy-4 which is still lower than 415 vacancies created in Stainless steel type 308 after only 100 collisions. Below are the exhibitions of the results obtained.

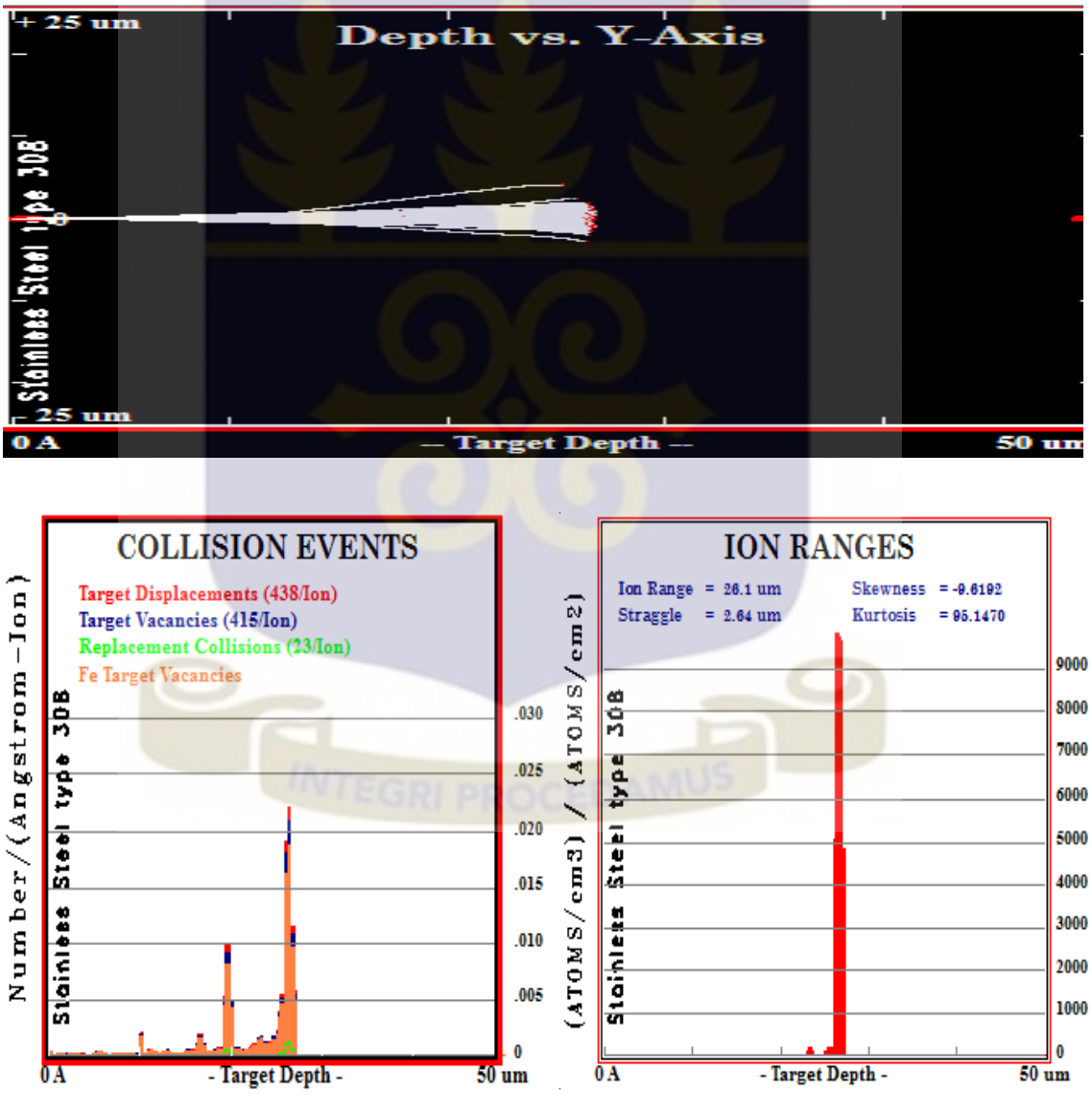

Figure 4.18: Damage Assessment by TRIM on Steel type-308 (Neutron Interaction).

4.2.2.4 Full damage assessment of Eurofer 97

After 100 collisions the results of the Co-60 gamma particle interaction with Eurofer 97 is almost similar to that of Stainless steel type-308 with gamma. Below is an illustration of the percentage energy lost during the interaction.

Table 4.7: Percentage Energy distribution in Eurofer 97 Target Material.

% Energy Loss	Ions (%)	Recoils (%)
Ionization	83.55	5.49
Vacancies	0.02	0.96
Phonons	0.11	9.87

Eurofer 97 interaction with gamma generated 33647 vacancies. 5.49% of the ionization taking place was as a result of the recoil. This is 0.11% more than that recorded for Stainless steel type 308. Both Iron carbide alloy recorded about the same recoil ions causing the primary radiation. The behaviour of Eurofer in this simulation showed similar traits as Stainless steel type 308 with a slightly higher outcome. This is eminent in fig. 4.28 below.

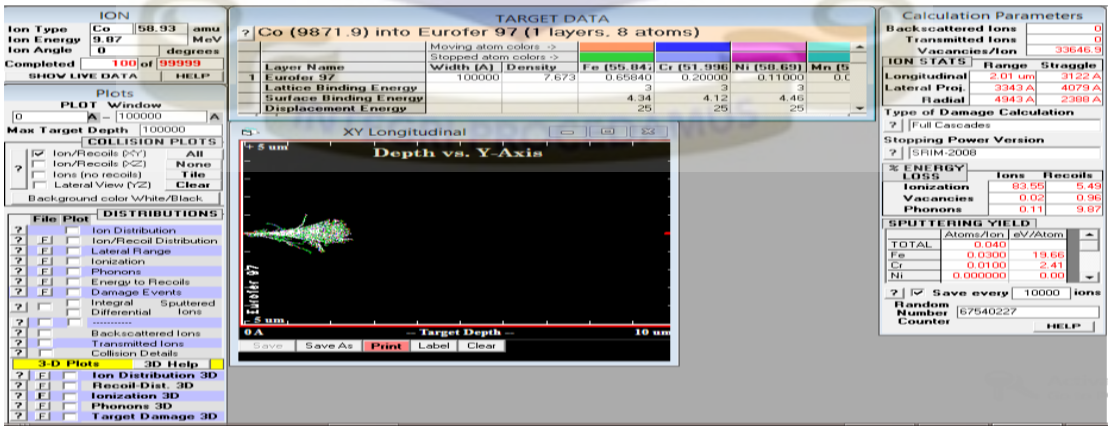

Figure 4.19: TRIM output for λ-Interaction with Eurofer 97.

A record high of 34739 displacements occurred in the collision event. Out of which 1137 lead to replacement of ions in the target lattice positions. This represents 3.27% as against 5.77% recorded for Stainless steel type 308. The trend remain the same for sputtering with Iron, Chromium and Nickel as the highest victims.

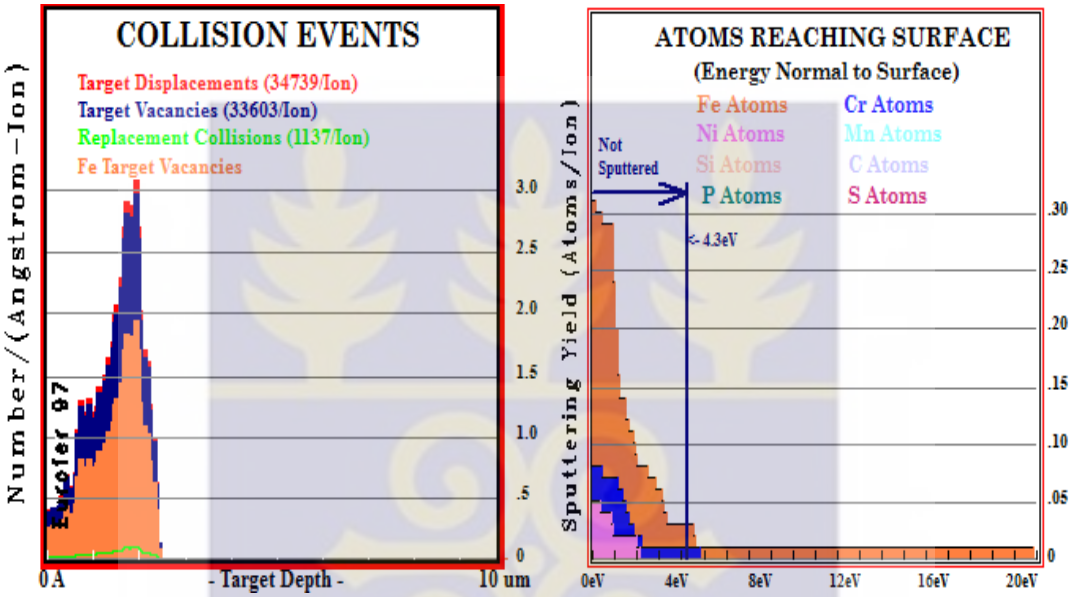

Figure 4.20: Atomic Displacement by Collision event and Sputtering (Eurofer 97).

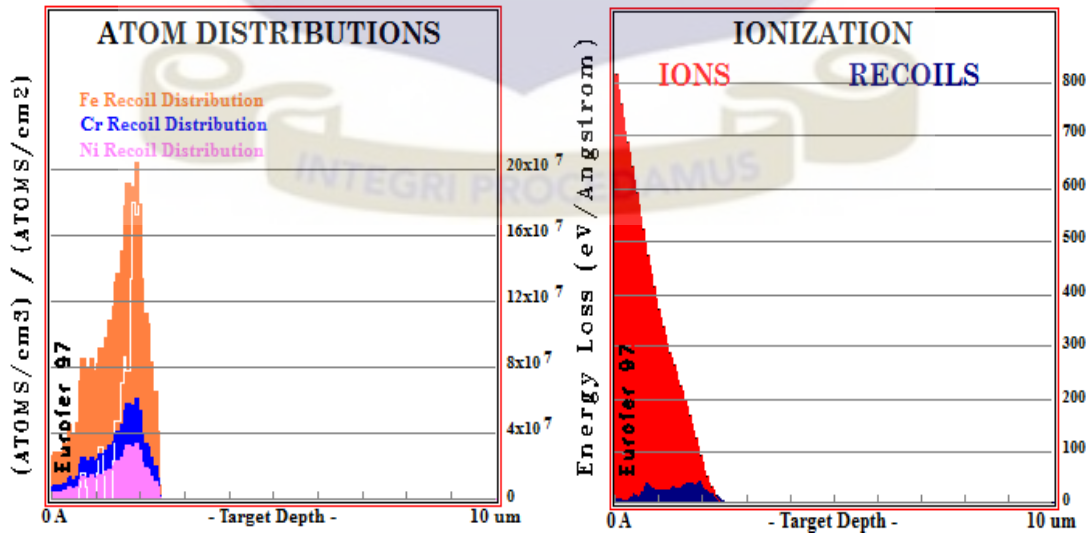

Figure 4.21: Illustration of Atom Distribution and Ionization (Eurofer 97).

For neutron interaction, a total of 366 vacancies were created. This is much lower than that recorded for neutron interaction in Eurofer 97. For 379 target displacement only 13 resulted into replacement collision. Below are the exhibitions of the results obtained.

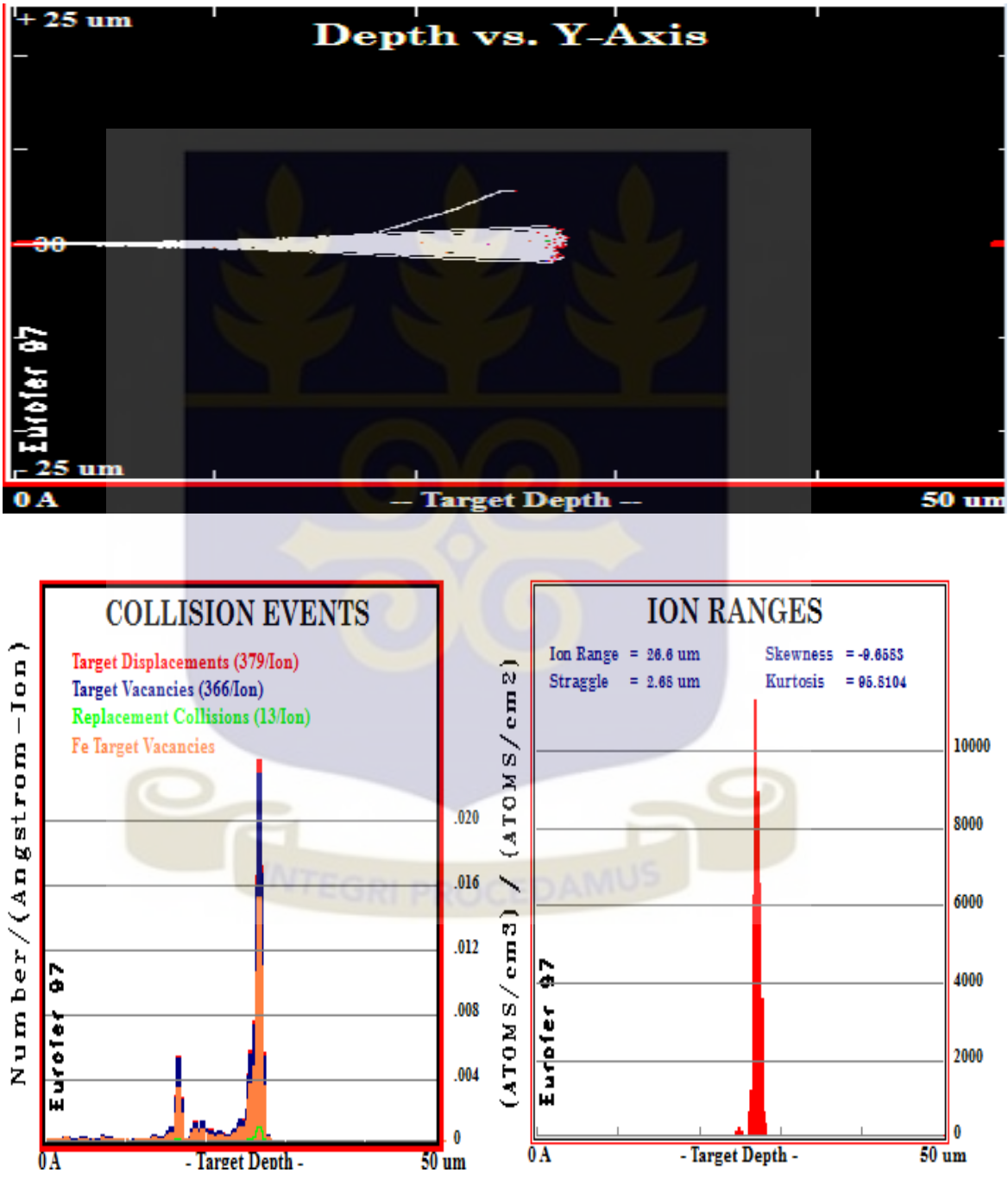

Figure 4.22: Damage Assessment by TRIM on Eurofer 97 (Neutron Interaction).

From the TRIM simulation, it has become crystal clear that zircaloy-4 sustained the least number of vacancies resulting from the collision. Zircaloy-4 also records the least percentage of energy for recoil ions which essentially contribute to the creation of primary radiation. The trend shown from the simulation agrees with the fact that the Iron chromium carbide (Fe-Cr-C) alloys have more vacancies ensuing from the collisions with Eurofer 97 having the highest vacancies of **33647**. However, Stainless steel type 308 recorded the highest percentage of recoil contributing to the creation of vacancies as well as the highest replacement collision of **1890**. The table below summarizes the outcome.

Table 4.8: Vacancy Assessment on clad materials.

Clad Materials	Vacancies	% Recoil Energy	Replacement Collision
Zircaloy-4	30356	0.09	147
Zircaloy-2	31569	0.94	1162
Stainless Steel type 308	32860	0.97	1890
Eurofer 97	33647	0.96	1137

Based on the findings from the SRIM-TRIM simulation, the analytical determination of the radiation damage using the radiation models will be carried-out on **zircaloy-4**. This is because it has shown to be a much better clad material than the other three cladding materials. Also, it suits this research work to ascertain the radiation damage of zircaloy-4 since it is used as the LEU clad material.

CHAPTER FIVE: CONCLUSIONS AND RECOMMENDATIONS

5.1 Conclusion

The MCNP5 simulation results for neutron (particle) flux and energy deposition on the Zircaloy-4 cladding material of the proposed LEU core at a Kcode specification of **500000 1.004 30 830** showed good trend of values for the three energy groups under study. TRIM data file was generated for the actual radiation damage assessment on the clad materials.

The neutron flux distribution over the zircaloy-4 cladding material of all 344 fuel pins sectioned into **4 7710 7720 7730 7740 7750 7760 7780 7790 -3** recorded an average fast neutron flux which was evaluated from the simulation as 5.29667E+11n/cm^2.s. The average thermal and epithermal flux gave 4.0896E+11 and 9.02759E+11 respectively. The average fast neutron flux in each of the ten concentric rings was **7.46E+13n/cm^2.s**.

The calculated average neutron energy deposition was **9.871884 MeV** as was evaluated from the F7 tally card using the MCNP5 simulation code.

The TRIM simulation established zircaloy-4 cladding material as the best since it sustained the least amount of vacancies of 30356 as against 31569, 32860 and 33647 from zircaloy-2, stainless steel type-308 and Eurofer 97 respectively. It registered the least energy for the recoil which was directly responsible for creating defects. Zircaloy-4 also showed little susceptibility to replacement collision.

The analytical calculation of radiation damage on zircaloy-4 cladding material using both the Kinchin-Pease model and the Norgett –Robinson Torrens model gave **0.00173** and **0.00138 dpa** respectively for only 30 minutes of clad exposure. The displacement per atom (dpa) for each neutron collision gave **4291.**

5.2 Recommendation

First of all, it is highly recommended to have a more in-depth analysis on the radiation damage assessment at the atomistic level using molecular dynamics code LAMMPS. LAMMPS will afford us the opportunity to ascertain the DPA of the clad material and the overall outlook or behaviour before and after collision from the VMD.

Also, it is recommended that another approach is used for the determination of energy deposition by both neutron and gamma particles using MCNPX to compare the findings.

REFERENCES

Akaho E.H., Maakuu B.T., Anim - Sampong, Emi - Reynolds, Boadu H.O., Osae E.K., Akoto - Bamford and Dodoo - Amoo D.N.A. (2003). *GHARR-1 Safety Analysis Report.* Ghana: GAEC.

American National Standards Institute (ANSI). (2007). *Standard practice for characterizing neutron exposures in Iron and low alloy Steels in terms of (DPA).* Retrieved from http://webstore.ansi.org/ansidocstore/product.asp?sku=ASTM+E693-01

Amuasi J.H., Schandorf C. and Yeboah J.,. (2005). *Safety of Ghana Research Reactor (GHARR-1).* Ghana: GAEC.

Argonne National Laboratory. (2016, March). MCNP5 Simulation of LEU for GHARR-1. USA.

Arthur E.D., Young P.G., Smith A.B. and Philis C.A. (1981). New tungsten Isotope evaluation for neutron energies between 0.1 and 20 MeV. *Trans. Am. Nucl., Soc. 39*, pp. 793.

Bacon D.J., Diaz de la Rubia T. (1994). Molecular Dynamics computer simulations of Displacement cascade in metal. *Journal of Nuclear Materials, volume 216*, pp. 275 -290.

Barett K., Bragg - Sitton, Galicki S.D. (2012). Advanced LWR Nuclear fuel cladding systems development trade - off study. *Idaho National Laboratory*.

Binnewies M., Glaum, Schmidt R. and Schmidt M.P. (2013). Chemical vapor transport reaction: A historical review. *Zeitschrift fur anorganische und allgemeine chemie*, vol. 693, pp 219 - 229.

Birikorang S.A. and Nyarko B.J.B. (2014). *Radiation detection.* University of Ghana, Legon., Department of Nuclear Engineering . Accra: Department of Nuclear Engineering.

Booth E. Thomas. (1992). Monte carlo variance reduction approaches for non-Boltzman tallies. *Los Alamos National laboratory report*, LA - 12433.

Bouffioux P. (EDF R&D) and Cheng B. (2001). Review of degradation phenomenon affecting fuel rod cladding. *Light water reactor fuel perfomance.*

Brian Linn. (2013). Radiation damage effects in materials. *Damage formation models*. MANE 6960.

Brookhaven National Laboratory. (2006). Evaluated Nuclear data file VI. ENDF - VI.

Cai W., Li J. and Yip S. (2012). Molecular dynamics in: Konings R.J.M., (ed) comprehensive nuclear materials. *Elsievier, Volume 1*, pp. 249 - 265.

Carter L.L. and Cashwell E.D. (1975). Particle transport simulation with the Monte carlo method. *ERDH critical review series TID - 26607*.

Chung H.M. and Kassner T.F. (1998). Cladding metallurgy and fracture behaviour during reactivity - initiated accidents at high burnup. *186*(3).

Crepin J., Bretheau T., Caldemaison D. (1995). Plastic deformation mechanisms of Beta - treated Zirconium. *Acta Metall Mater, Volume 43*(10), pp. 3709 - 3719.

Darko J.,. (2013). *Computation of thermal stresses in GHARR-1 vessel due to unsteady flow of reactor coolant using the finite element method.* MPhil Thesis, University of Ghana,Legon, Department of Nuclear Engineering, Accra.

Diaz dela Rubia T., Averback R.S., Hsieh Horngming. and Benedek R. (1989). Molecular dynamics simulation of displacement cascade in Cu and Ni: Thermal spike behavior. *Journal of Materials Research, volume 4*, pp. 579 - 586.

Donald Olander and Arthur Motta. (2006). Light water reactor materials. *volume 1*, pp. 3 - 4.

Donald R. Olander. (1975). *Fundamentals aspect of nuclear reactor element.*

Donald R. Olander. (1976). *Fundament aspects of nuclear reactor fuel elements.* Energy Research and Development Administration.

Donald R. Olander. (1976). *Radiation damage: Fundamental aspects of nuclear reactor elements.* University of California, Department of Nuclear Engineering, Berkeley.

Douglass, D. (1971). *The metallurrgy of Zirconium.* Atomic energy review supplement.

Festus f. Appiah - Ofori. (2014). *Assessment of Gamma irradiation heating and damage of Miniature Neutron Source Reactor vessel using computaional methods and SRIM - TRIM Code.* MPhil Thesis, University of Ghana, legon, Department of Nuclear Engineering, Accra. Retrieved March 2014

Foster R.A. (1991). A new method of assessing the statistical convergence of Monte carlo solutions. *Trans.Am.Nucl.soc, volume 64*, pp. 305.

Gibbs G.B. and Hales R. (1977). *The influence of metal lattice vacancies on the oxidation of high temperature materials* (Vol. 17). Corrsion Science.

Greenwood L.R. and Smither R.K. (1985). SPECTER: Neutron damage calculations for materials irradiations. *ANL/FPP/TM - 197*.

Hannien H. (1990). Phenomena of material degradation with relevance to reactor pressure vessel. *NEA/CSNI Workshop on Safety assessment of reactor pressure vessels, volume 1*, p. pp. 13. Espoo, Finland.

Heinish H.J., and Singh B.N. (1993). On the structure of irradiation induced collision cascades in metals as a function of recoil energy and crystal structure. *Philosophy magazine, volume 67*, pp. 407 - 424.

Hocking W.H., Verrall R.A. and Muir I.J. (2001). Migration behaviour of Iodine in nuclear fuel. *Journal of Nuclear Materials, volume 294*, pp. 45 - 52.

Hoppe G., Damaschun F. and Wappler G. (1987). An appreciation of Martin Heinrich Klaproth as a mineral chemist. *Pharmazie, 44*(4), pp. 266 - 7.

International Atomic Energy Agency. (2009). Intergrity of reactor pressure vessels in nuclear power plant. *Assessment of irradiation embrittlement effects in reactor pressure vessels steels.* Vienna: IAEA Nuclear Energy Series No.NP-T-3.11.

International Atomic Energy Agency. (n.d.). *Development of radiation resistance reactor core structural materials*. Retrieved from google: http://www.iaea.org/About/Policy/GC/GC51/GC51InfDocuments/English/gc51inf-3-att7_en.pdf

Knoll G.F. (1989). Radiation detection and measurements. New York: John Wiley & Sons.

Korean Atomic Energy Research Institute. (2013). *Table of nuclides.* Retrieved February 1st, 2014, from http://atom.kaeri.re.kr/

Krebs R. (1998). *The history and use of our earth's chemical elements.* (Westport, Ed.) Connecticut: Greenwood Press.

Kroll W. (1940). The production of ductile Titanium. *Transactions of the electrochemical society, volume 78*, pp. 35 - 47.

Lee J.G. (2005). *Computational materials science: An introduction.* New York, USA: 1st Edition.

Liu H., Chen Y., Tang Y., Wei S. and Niu G,. (2007). The microstructure, tensile properties and creep behaviour of As - cast Mg - (1 - 10)% Sn alloys. *Journal of alloys and compounds, volume 448*, pp. 123 - 4.

MacFarlane R.E., Muir D.W. and Boicourt R.M. (1982). The NJOY Nuclear data processing system. *Los Alamos National Laboratory, volume I*(ENDF-324).

Maisonnier D. (2006). DEMO and fusion power plant conceptual studies in Europe. *Fusion Engineering and Design, volume 81*, pp. 1123.

Mansur L.K. and Farell K. (1997). Mechanisms of radiation - induced degradation of reactor vessel materials. *Journal of Nuclear Materials, volume 244*, pp. 213.

Matzke H.J. (1992). Radiation damage in nuclear materials. *Nuclear Instruments and methods in Physics Research B, volume 65*, pp. 30 - 39.

Matzke H.J. and Turos A. (1992). Ion implantation studies of UO_2 and UN. *Journal of Nuclear Materials, volume 188*, pp. 285 - 292.

Matzke H.J., Turos A. and Linker G. (1994). Polygonization of single crystals of the flourite - type oxide UO_2 due to dose ion implantation. *Nuclear Instruments and Methods in Physics Research B, volume 91*, pp. 294 - 300.

McElroy R.J. (2004). Low temperature embrittlement of LWR PRV support structures. *NEA/CSNI Workshop on safety assessment of reactor pressure vessels, volume 2*, p. 311. Espoo, Finland.

Meldrum A., Zinkle S.J., Boatner L.A and Ewing R.C. (1998). A transient liquid - like phase in the displacement cascades of Zircon. *Hafnon and Thorite, volume 395*, pp. 56 - 58.

Nastasi M., Mayer J. and Hirvonen J.K. (2004). Ion - Solid interactions: Fundamentals and Applications. *Cambridge University Press*.

Norgett M.J., Robinson M.T. and Torren I.M. (1975). A proposed method for calculating displacement dose rates. *Nuclear Engineering and Design, volume 33*, pp. 50 - 54.

Nuclear regulatory commission. (2013). Pressurized Water Reactors. Retrieved January 22, 2014, from http://www.nrc.gov/reactors/pwers.html.

Nyarko B.J.B. and Deborah S. (2012). *Types of reactors.* University of Ghana,Legon, Department of Nuclear Engineering. Accra: Department of Nuclear Engineering.

Oak Ridge National Laboratory (ORNL). (n.d.). Application to fusion and generation IV fusion reactors. *Workshop on Advanced computational materials science*(ORNL/TM - 2004/132). Retrieved June 2004

Odoi H.C., Akaho E.H.K. and Anim - Sampong. (2011). Investigative studies on effect of reflector thickness on the performance of low enriched uranium-fueled Miniature Neutron Source Reactors. (N. E. Design, Ed.) *Elsevier, volume 241*, pp. 2909 - 2915.

Olander, D. R. (2006). *Radiation damage and neutron irradiation* (Vol. section 9). Fundamental aspects of nuclear reactor fuel elements.

Parkin D.M., Coulter C.A. (1981). Total and net displacement functions for polyatomic materials. *Journal of Nuclear Materials, volume 101*, pp. 261 - 276.

Quaye C.R. (2012). *Finite element modelling of transient heat conduction of fuel element of Ghana research reactor - 1.* School of Nuclear and Allied Sciences, Department of Nuclear Engineering. Accra: University of Ghana.

Ragheb M. (2013). Loss of coolant accidents (LOCA). Retrieved January 9th, 2014, from http://mragheb.com

Robert W.C. and Haasen P. (1996). *Physical metallurgy.* PhD Thesis, Technical University Darmstadt, Department of materials science.

Robinson, Mark, Torrens and Ian. (1974). Computer simulation of atomic - displacement cascade in solids in the binary - collision approximation. *Physical review, B9*(12), 5008.

Roger E. Stoller. (2011). Radiation damage fundamentals: Primary damage production. *Materials science and technology division, Oak Ridge National Laboratory, Joint EFRC Summer school*.

Rose P.F. (1991). ENDF - 201, ENDF/B - VI, Compiler and Editor, Summary documentation. Brookhaven National Laboratory.

Sandvik special metal corporation (1989). (1989). Zirconium alloy fuel clad tubing. *Engineering guide, 1st Edition*.

Schaeublin R., Leguey T., Spatig P., Baluc N. and Victoria M. (2002). Microstructure and mechanical properties of two ODS ferritic/martensitic steels. *Journal of Nuclear Materials* , pp. 307 - 311.

Schweitzer P. (2003). Zirconium and Zirconium alloy metallic materials. *Physical, mechanical and corrosion properties*, pp. 647 - 666.

Sekpe H. and Sekpe I. (1986). The history of Physiologic chemistry in the first years of its existence at the Berlin University: Contributions of the chemist M.H. Klaproth and others. *Zeitschrift fur die gesamte Hygiene und ihre Grenzgebiete, volume 32*(8), pp. 504 - 6.

Sika Boafo. (2012). *Determination of neutron parameters in the GHARR-1 reactor using MCNP and TRIM codes.* School of Nuclear and Allied Sciences, Department of Nuclear Engineering. Accra: University of Ghana.

Stanislav Golubov and Roger Stoller. (2004). Materials and technical division. *Oak Ridge National Laboratory* .

Todreas N. and Kazimi M. (2011). Nuclear systems: 2nd Edition. *Taylor & Francis, volume I: Thermal hydraulic fundamentals*, pp. 20 - 22, 33 - 34.

Tritt T. (2004). Thermal conductivity: Theory, properties and Applications. *Physics of solids and liquid, Springer - Verlag*, pp. 41 - 47.

Tsegay H. (2011). *Measurement of energy of Gamma radiation.* M.Sc Thesis, Addis Ababa University, Department of Physics, Addis Ababa.

Van Dam H., Van der Hagen T.H.J.J. and Hoogenboom J.E. (2005). *Nuclear reactor physics.* Delft University of Technology, Department of Nuclear Engineering.

Verlet L. (1968). Computer experiments on classical fluid II: Equilibrium correlation functions. *Phys.Rev., volume 165*, pp. 201 - 214.

Was G.S. (2007). Fundamentals of radiation materials science metal and alloys. *Journal of Materials Science*.

Weinberg A.M. (1994). *The first nuclear era: The life and times of technological fixers.* New York: AIP Press.

William D. Callister Jr. (2005). *Materials science and Engineering.* Book, University of Utah, Department of Metallurgical Engineering.

X - 5 Monte carlo team. (2003). MCNP - A General Monte carlo N - Particle transport code version 5. *Los Alamos National Laboratory, volume I: Overview & Theory*, pp. 1 - 11.

Yuri Osetsky. (2008). Introduction to radiation damage. *Oak Ridge National Laboratory*.

Zenngliang Y. and Liangdeng Y. (2006). Introduction to Ion beam biotechnology. *Springer*.

Ziegler J.F., Ziegler M.D and Biersack J.P. (2010). SRIM - The stopping and range of Ions in matter. *Pergamum Press*.

Zircaloy heat capacity. (1997). Retrieved from International Nuclear Safety centre: http://www.insc.anl.gov/matprop/zircalov/zirccp/fmt html.pdf

APPENDIX I: Data from MCNP5 Simulation of Neutron Parameters for all 344 Fuel Pins and 4 Tie rods Clads (Argonne National Laboratory).

Clad	Thermal	Epithermal	Fast flux	Total flux
7	4.449E+11	1.09E+12	6.51E+11	2.18E+12
9	4.474E+11	1.09E+12	6.50E+11	2.18E+12
11	4.444E+11	1.09E+12	6.49E+11	2.18E+12
13	4.437E+11	1.08E+12	6.50E+11	2.18E+12
15	4.414E+11	1.09E+12	6.47E+11	2.18E+12
17	4.445E+11	1.09E+12	6.48E+11	2.19E+12
19	4.532E+11	1.08E+12	6.50E+11	2.18E+12
21	4.553E+11	1.08E+12	6.5E+11	2.18E+12
23	4.538E+11	1.08E+12	6.50E+11	2.18E+12
25	4.554E+11	1.08E+12	6.50E+11	2.19E+12
27	4.505E+11	1.08E+12	6.48E+11	2.18E+12
29	4.459E+11	1.08E+12	6.49E+11	2.18E+12
31	4.447E+11	1.09E+12	6.48E+11	2.18E+12
33	4.441E+11	1.08E+12	6.47E+11	2.18E+12
35	4.377E+11	1.08E+12	6.48E+11	2.17E+12
37	4.433E+11	1.08E+12	6.49E+11	2.17E+12
39	4.402E+11	1.08E+12	6.49E+11	2.17E+12
41	4.487E+11	1.08E+12	6.49E+11	2.18E+12
43	4.506E+11	1.06E+12	6.42E+11	2.16E+12
45	4.507E+11	1.06E+12	6.40E+11	2.15E+12
47	4.494E+11	1.07E+12	6.40E+11	2.16E+12
49	4.534E+11	1.07E+12	6.40E+11	2.16E+12
51	4.544E+11	1.06E+12	6.44E+11	2.16E+12
53	4.495E+11	1.07E+12	6.38E+11	2.15E+12
55	4.490E+11	1.06E+12	6.37E+11	2.15E+12

57	4.517E+11	1.06E+12	6.40E+11	2.16E+12
59	4.376E+11	1.06E+12	6.43E+11	2.14E+12
61	4.287E+11	1.07E+12	6.49E+11	2.14E+12
63	4.229E+11	1.07E+12	6.45E+11	2.13E+12
65	4.248E+11	1.07E+12	6.43E+11	2.13E+12
67	4.239E+11	1.07E+12	6.42E+11	2.13E+12
69	4.227E+11	1.07E+12	6.42E+11	2.13E+12
71	4.243E+11	1.07E+12	6.44E+11	2.13E+12
73	4.238E+11	1.07E+12	6.43E+11	2.14E+12
75	4.269E+11	1.07E+12	6.46E+11	2.14E+12
77	4.314E+11	1.06E+12	6.42E+11	2.14E+12
79	4.387E+11	1.06E+12	6.45E+11	2.15E+12
81	4.394E+11	1.04E+12	6.25E+11	2.10E+12
83	4.424E+11	1.04E+12	6.21E+11	2.1E+12
85	4.389E+11	1.03E+12	6.27E+11	2.09E+12
87	4.409E+11	1.04E+12	6.23E+11	2.09E+12
89	4.43E+11	1.04E+12	6.28E+11	2.11E+12
91	4.437E+11	1.04E+12	6.27E+11	2.11E+12
93	4.419E+11	1.04E+12	6.27E+11	2.11E+12
95	4.400E+11	1.04E+12	6.28E+11	2.11E+12
97	4.447E+11	1.03E+12	6.25E+11	2.11E+12
99	4.424E+11	1.04E+12	6.26E+11	2.11E+12
101	4.396E+11	1.04E+12	6.24E+11	2.1E+12
103	4.27E+11	1.04E+12	6.27E+11	2.09E+12
105	4.16E+11	1.04E+12	6.3E+11	2.09E+12
107	4.126E+11	1.03E+12	6.29E+11	2.08E+12
109	4.108E+11	1.04E+12	6.31E+11	2.08E+12
111	4.118E+11	1.04E+12	6.29E+11	2.08E+12

113	4.124E+11	1.04E+12	6.28E+11	2.08E+12
115	4.114E+11	1.04E+12	6.27E+11	2.08E+12
117	4.108E+11	1.04E+12	6.28E+11	2.08E+12
119	4.131E+11	1.04E+12	6.28E+11	2.08E+12
121	4.106E+11	1.04E+12	6.27E+11	2.08E+12
123	4.131E+11	1.04E+12	6.30E+11	2.08E+12
125	4.134E+11	1.04E+12	6.3E+11	2.08E+12
127	4.131E+11	1.04E+12	6.28E+11	2.08E+12
129	4.188E+11	1.04E+12	6.31E+11	2.09E+12
131	4.27E+11	1.04E+12	6.29E+11	2.09E+12
133	4.235E+11	1.00E+12	6.06E+11	2.03E+12
135	4.229E+11	9.99E+11	6.09E+11	2.03E+12
137	4.239E+11	1.00E+12	6.04E+11	2.03E+12
139	4.214E+11	9.98E+11	6.07E+11	2.03E+12
141	4.227E+11	9.99E+11	6.09E+11	2.03E+12
143	4.248E+11	1.00E+12	6.07E+11	2.03E+12
145	4.259E+11	1.00E+12	6.06E+11	2.04E+12
147	4.255E+11	1.00E+12	6.07E+11	2.04E+12
149	4.232E+11	9.99E+11	6.09E+11	2.03E+12
151	4.244E+11	1.00E+12	6.05E+11	2.03E+12
153	4.226E+11	1.00E+12	6.08E+11	2.04E+12
155	4.205E+11	1.00E+12	6.07E+11	2.03E+12
157	4.213E+11	1.01E+12	6.06E+11	2.03E+12
159	4.202E+11	1.00E+12	6.05E+11	2.03E+12
161	4.203E+11	1.00E+12	6.08E+11	2.03E+12
163	4.158E+11	1.01E+12	6.06E+11	2.03E+12
165	4.148E+11	1.01E+12	6.06E+11	2.03E+12
167	4.075E+11	1.01E+12	6.07E+11	2.02E+12

169	4.073E+11	1.01E+12	6.05E+11	2.02E+12
171	4.069E+11	1.01E+12	6.06E+11	2.02E+12
173	4.06E+11	1.01E+12	6.05E+11	2.02E+12
175	4.07E+11	1.01E+12	6.04E+11	2.02E+12
177	4.085E+11	1.01E+12	6.05E+11	2.03E+12
179	4.063E+11	1.01E+12	6.04E+11	2.02E+12
181	4.082E+11	1.01E+12	6.08E+11	2.02E+12
183	4.077E+11	1.01E+12	6.04E+11	2.02E+12
185	4.082E+11	1.01E+12	6.07E+11	2.02E+12
187	4.081E+11	1.01E+12	6.07E+11	2.02E+12
189	4.076E+11	1.01E+12	6.07E+11	2.02E+12
191	4.103E+11	1.00E+12	6.08E+11	2.02E+12
193	4.114E+11	1.01E+12	6.09E+11	2.03E+12
195	4.153E+11	1.00E+12	6.08E+11	2.03E+12
197	4.108E+11	9.62E+11	5.82E+11	1.95E+12
199	4.088E+11	9.63E+11	5.80E+11	1.95E+12
201	4.070E+11	9.59E+11	5.79E+11	1.95E+12
203	4.06E+11	9.63E+11	5.79E+11	1.95E+12
205	4.061E+11	9.57E+11	5.79E+11	1.94E+12
207	4.071E+11	9.59E+11	5.80E+11	1.95E+12
209	4.092E+11	9.66E+11	5.82E+11	1.96E+12
211	4.1E+11	9.64E+11	5.83E+11	1.96E+12
213	4.111E+11	9.59E+11	5.82E+11	1.95E+12
215	4.111E+11	9.59E+11	5.80E+11	1.95E+12
217	4.109E+11	9.59E+11	5.80E+11	1.95E+12
219	4.051E+11	9.55E+11	5.80E+11	1.94E+12
221	4.052E+11	9.64E+11	5.81E+11	1.95E+12
223	4.076E+11	9.63E+11	5.8E+11	1.95E+12

225	4.074E+11	9.66E+11	5.79E+11	1.95E+12
227	4.047E+11	9.63E+11	5.79E+11	1.95E+12
229	4.067E+11	9.60E+11	5.79E+11	1.95E+12
231	4.072E+11	9.65E+11	5.79E+11	1.95E+12
233	4.06E+11	9.65E+11	5.81E+11	1.95E+12
235	3.991E+11	9.63E+11	5.81E+11	1.94E+12
237	3.945E+11	9.64E+11	5.82E+11	1.94E+12
239	3.969E+11	9.63E+11	5.78E+11	1.94E+12
241	3.958E+11	9.65E+11	5.80E+11	1.94E+12
243	3.936E+11	9.66E+11	5.79E+11	1.94E+12
245	3.962E+11	9.63E+11	5.79E+11	1.94E+12
247	3.946E+11	9.65E+11	5.82E+11	1.94E+12
249	3.959E+11	9.63E+11	5.79E+11	1.94E+12
251	3.961E+11	9.63E+11	5.81E+11	1.94E+12
253	3.981E+11	9.66E+11	5.81E+11	1.95E+12
255	3.968E+11	9.65E+11	5.81E+11	1.94E+12
257	3.945E+11	9.65E+11	5.79E+11	1.94E+12
259	3.967E+11	9.64E+11	5.81E+11	1.94E+12
261	3.946E+11	9.66E+11	5.79E+11	1.94E+12
263	3.934E+11	9.60E+11	5.81E+11	1.94E+12
265	3.966E+11	9.66E+11	5.79E+11	1.94E+12
267	3.949E+11	9.69E+11	5.82E+11	1.95E+12
269	3.952E+11	9.63E+11	5.79E+11	1.94E+12
271	3.983E+11	9.62E+11	5.81E+11	1.94E+12
273	4.068E+11	9.61E+11	5.81E+11	1.95E+12
275	4.006E+11	9.13E+11	5.48E+11	1.86E+12
277	3.918E+11	9.12E+11	5.46E+11	1.85E+12
279	3.921E+11	9.15E+11	5.50E+11	1.86E+12

281	3.907E+11	9.16E+11	5.49E+11	1.86E+12
283	3.902E+11	9.13E+11	5.49E+11	1.85E+12
285	3.927E+11	9.14E+11	5.49E+11	1.86E+12
287	3.944E+11	9.14E+11	5.49E+11	1.86E+12
289	3.939E+11	9.15E+11	5.51E+11	1.86E+12
291	3.967E+11	9.14E+11	5.48E+11	1.86E+12
293	4.023E+11	9.15E+11	5.47E+11	1.86E+12
295	4.129E+11	9.14E+11	5.46E+11	1.87E+12
297	4.015E+11	9.17E+11	5.48E+11	1.87E+12
299	3.945E+11	9.13E+11	5.48E+11	1.86E+12
301	3.927E+11	9.15E+11	5.48E+11	1.86E+12
303	3.951E+11	9.16E+11	5.50E+11	1.86E+12
305	3.923E+11	9.15E+11	5.48E+11	1.86E+12
307	3.931E+11	9.16E+11	5.51E+11	1.86E+12
309	3.939E+11	9.14E+11	5.51E+11	1.86E+12
311	3.917E+11	9.14E+11	5.49E+11	1.86E+12
313	3.948E+11	9.15E+11	5.51E+11	1.86E+12
315	4.008E+11	9.16E+11	5.45E+11	1.86E+12
317	4.077E+11	9.14E+11	5.45E+11	1.87E+12
319	3.929E+11	9.14E+11	5.46E+11	1.85E+12
321	3.85E+11	9.16E+11	5.51E+11	1.85E+12
323	3.854E+11	9.16E+11	5.48E+11	1.85E+12
325	3.83E+11	9.18E+11	5.47E+11	1.85E+12
327	3.825E+11	9.21E+11	5.48E+11	1.85E+12
329	3.828E+11	9.19E+11	5.49E+11	1.85E+12
331	3.830E+11	9.18E+11	5.46E+11	1.85E+12
333	3.831E+11	9.19E+11	5.49E+11	1.85E+12
335	3.852E+11	9.19E+11	5.48E+11	1.85E+12

337	3.895E+11	9.19E+11	5.51E+11	1.86E+12
339	3.985E+11	9.16E+11	5.49E+11	1.86E+12
341	4.015E+11	9.11E+11	5.47E+11	1.86E+12
343	3.871E+11	9.2E+11	5.49E+11	1.86E+12
345	3.84E+11	9.19E+11	5.47E+11	1.85E+12
347	3.811E+11	9.22E+11	5.47E+11	1.85E+12
349	3.828E+11	9.21E+11	5.50E+11	1.85E+12
351	3.832E+11	9.19E+11	5.52E+11	1.85E+12
353	3.818E+11	9.17E+11	5.50E+11	1.85E+12
355	3.819E+11	9.19E+11	5.48E+11	1.85E+12
357	3.840E+11	9.16E+11	5.49E+11	1.85E+12
359	3.856E+11	9.17E+11	5.49E+11	1.85E+12
361	3.946E+11	9.18E+11	5.49E+11	1.86E+12
363	4.094E+11	9.12E+11	5.44E+11	1.87E+12
365	4.035E+11	8.61E+11	5.08E+11	1.77E+12
367	3.833E+11	8.66E+11	5.14E+11	1.76E+12
369	3.770E+11	8.65E+11	5.13E+11	1.76E+12
371	3.763E+11	8.64E+11	5.14E+11	1.75E+12
373	3.791E+11	8.62E+11	5.14E+11	1.76E+12
375	3.799E+11	8.62E+11	5.14E+11	1.76E+12
377	3.762E+11	8.67E+11	5.13E+11	1.76E+12
379	3.770E+11	8.63E+11	5.13E+11	1.75E+12
381	3.782E+11	8.66E+11	5.16E+11	1.76E+12
383	3.835E+11	8.67E+11	5.14E+11	1.77E+12
385	3.863E+11	8.64E+11	5.14E+11	1.76E+12
387	4.034E+11	8.61E+11	5.11E+11	1.78E+12
390	3.981E+11	8.63E+11	5.09E+11	1.77E+12
392	3.857E+11	8.63E+11	5.12E+11	1.76E+12

394	3.771E+11	8.6E+11	5.11E+11	1.75E+12
396	3.787E+11	8.66E+11	5.13E+11	1.76E+12
398	3.787E+11	8.66E+11	5.13E+11	1.76E+12
400	3.773E+11	8.65E+11	5.12E+11	1.75E+12
402	3.823E+11	8.69E+11	5.13E+11	1.77E+12
404	3.824E+11	8.64E+11	5.15E+11	1.76E+12
406	3.792E+11	8.64E+11	5.12E+11	1.76E+12
408	3.766E+11	8.64E+11	5.11E+11	1.75E+12
410	3.844E+11	8.61E+11	5.13E+11	1.76E+12
412	4.012E+11	8.63E+11	5.09E+11	1.77E+12
415	3.967E+11	8.63E+11	5.06E+11	1.77E+12
417	3.776E+11	8.67E+11	5.12E+11	1.76E+12
419	3.769E+11	8.64E+11	5.09E+11	1.75E+12
421	3.767E+11	8.66E+11	5.10E+11	1.75E+12
423	3.743E+11	8.69E+11	5.12E+11	1.76E+12
425	3.739E+11	8.72E+11	5.11E+11	1.76E+12
427	3.743E+11	8.68E+11	5.12E+11	1.75E+12
429	3.75E+11	8.69E+11	5.12E+11	1.76E+12
431	3.752E+11	8.69E+11	5.12E+11	1.76E+12
433	3.781E+11	8.69E+11	5.13E+11	1.76E+12
435	3.801E+11	8.68E+11	5.15E+11	1.76E+12
437	3.971E+11	8.68E+11	5.07E+11	1.77E+12
440	3.966E+11	8.64E+11	5.08E+11	1.79E+12
442	3.788E+11	8.69E+11	5.15E+11	1.76E+12
444	3.739E+11	8.68E+11	5.16E+11	1.76E+12
446	3.748E+11	8.69E+11	5.14E+11	1.76E+12
448	3.756E+11	8.64E+11	5.11E+11	1.75E+12
450	3.728E+11	8.68E+11	5.12E+11	1.75E+12

452	3.727E+11	8.67E+11	5.14E+11	1.75E+12
454	3.73E+11	8.67E+11	5.16E+11	1.76E+12
456	3.755E+11	8.68E+11	5.12E+11	1.76E+12
458	3.776E+11	8.66E+11	5.12E+11	1.76E+12
460	3.798E+11	8.64E+11	5.13E+11	1.76E+12
462	3.968E+11	8.63E+11	5.09E+11	1.77E+12
465	4.056E+11	8.04E+11	4.67E+11	1.68E+12
467	3.845E+11	8.10E+11	4.71E+11	1.67E+12
469	3.765E+11	8.13E+11	4.73E+11	1.66E+12
471	3.723E+11	8.09E+11	4.74E+11	1.66E+12
473	3.785E+11	8.13E+11	4.71E+11	1.66E+12
475	3.869E+11	8.06E+11	4.67E+11	1.66E+12
477	3.870E+11	8.07E+11	4.69E+11	1.66E+12
479	3.756E+11	8.09E+11	4.71E+11	1.66E+12
481	3.732E+11	8.09E+11	4.75E+11	1.66E+12
483	3.764E+11	8.09E+11	4.75E+11	1.66E+12
485	3.879E+11	8.10E+11	4.68E+11	1.67E+12
487	3.956E+11	8.12E+11	4.68E+11	1.68E+12
489	3.877E+11	8.09E+11	4.74E+11	1.67E+12
491	3.948E+11	8.08E+11	4.69E+11	1.67E+12
493	3.916E+11	8.07E+11	4.69E+11	1.67E+12
495	3.873E+11	8.09E+11	4.71E+11	1.67E+12
497	3.955E+11	8.05E+11	4.66E+11	1.67E+12
499	3.844E+11	8.08E+11	4.68E+11	1.66E+12
501	3.752E+11	8.13E+11	4.73E+11	1.66E+12
503	3.735E+11	8.11E+11	4.71E+11	1.66E+12
505	3.770E+11	8.11E+11	4.73E+11	1.66E+12
507	3.884E+11	8.12E+11	4.73E+11	1.67E+12

509	3.918E+11	8.08E+11	4.66E+11	1.67E+12
511	3.799E+11	8.11E+11	4.71E+11	1.66E+12
513	3.743E+11	8.09E+11	4.72E+11	1.66E+12
515	3.746E+11	8.12E+11	4.71E+11	1.66E+12
517	3.834E+11	8.10E+11	4.69E+11	1.66E+12
519	4.026E+11	8.04E+11	4.66E+11	1.67E+12
521	4.021E+11	8.06E+11	4.68E+11	1.68E+12
523	3.822E+11	8.08E+11	4.71E+11	1.66E+12
525	3.769E+11	8.14E+11	4.70E+11	1.66E+12
527	3.768E+11	8.11E+11	4.72E+11	1.66E+12
529	3.877E+11	8.1E+11	4.70E+11	1.67E+12
531	3.88E+11	8.15E+11	4.71E+11	1.67E+12
533	3.722E+11	8.14E+11	4.72E+11	1.66E+12
535	3.711E+11	8.17E+11	4.72E+11	1.66E+12
537	3.732E+11	8.11E+11	4.70E+11	1.65E+12
539	3.828E+11	8.13E+11	4.69E+11	1.67E+12
541	3.896E+11	8.12E+11	4.67E+11	1.67E+12
543	3.73E+11	8.14E+11	4.69E+11	1.66E+12
545	3.697E+11	8.14E+11	4.71E+11	1.66E+12
547	3.791E+11	8.13E+11	4.68E+11	1.66E+12
549	3.973E+11	8.08E+11	4.68E+11	1.67E+12
551	4.103E+11	8.10E+11	4.69E+11	1.69E+12
553	3.864E+11	8.11E+11	4.73E+11	1.67E+12
555	3.733E+11	8.14E+11	4.73E+11	1.66E+12
557	3.734E+11	8.17E+11	4.73E+11	1.66E+12
559	3.753E+11	8.12E+11	4.72E+11	1.66E+12
561	3.902E+11	8.11E+11	4.69E+11	1.67E+12
563	3.817E+11	8.09E+11	4.72E+11	1.66E+12

565	3.725E+11	8.13E+11	4.74E+11	1.66E+12
567	3.727E+11	8.08E+11	4.68E+11	1.65E+12
569	3.738E+11	8.12E+11	4.71E+11	1.66E+12
571	3.859E+11	8.11E+11	4.66E+11	1.66E+12
573	3.875E+11	8.11E+11	4.71E+11	1.67E+12
575	3.813E+11	8.12E+11	4.74E+11	1.67E+12
577	3.88E+11	8.11E+11	4.70E+11	1.67E+12
579	4.045E+11	8.11E+11	4.68E+11	1.68E+12
581	5.505E+11	7.19E+11	3.05E+11	1.57E+12
583	4.256E+11	7.52E+11	4.13E+11	1.59E+12
585	4.052E+11	7.58E+11	4.21E+11	1.58E+12
587	4.007E+11	7.55E+11	4.19E+11	1.57E+12
589	4.021E+11	7.57E+11	4.19E+11	1.58E+12
591	4.2E+11	7.52E+11	4.14E+11	1.59E+12
593	5.416E+11	7.21E+11	3.06E+11	1.57E+12
595	4.190E+11	7.56E+11	4.16E+11	1.59E+12
597	4.05E+11	7.54E+11	4.19E+11	1.58E+12
3598	4.041E+11	7.55E+11	4.23E+11	1.58E+12
600	4.054E+11	7.56E+11	4.19E+11	1.58E+12
602	4.239E+11	7.57E+11	4.16E+11	1.59E+12
604	5.488E+11	7.26E+11	3.04E+11	1.58E+12
606	4.273E+11	7.54E+11	4.16E+11	1.59E+12
608	4.099E+11	7.56E+11	4.19E+11	1.59E+12
610	4.071E+11	7.54E+11	4.23E+11	1.59E+12
612	4.076E+11	7.49E+11	4.19E+11	1.58E+12
614	4.243E+11	7.49E+11	4.16E+11	1.59E+12
616	5.435E+11	7.19E+11	3.04E+11	1.57E+12
3617	4.213E+11	7.51E+11	4.14E+11	1.59E+12

619	4.061E+11	7.57E+11	4.2E+11	1.58E+12
621	4.027E+11	7.56E+11	4.22E+11	1.58E+12
623	4.057E+11	7.56E+11	4.21E+11	1.58E+12
625	4.242E+11	7.57E+11	4.15E+11	1.59E+12
627	5.509E+11	7.25E+11	3.04E+11	1.58E+12
629	4.261E+11	7.55E+11	4.18E+11	1.59E+12
631	4.064E+11	7.54E+11	4.22E+11	1.58E+12
633	4.011E+11	7.55E+11	4.22E+11	1.58E+12
635	4.074E+11	7.56E+11	4.19E+11	1.58E+12
3636	4.217E+11	7.50E+11	4.15E+11	1.59E+12
638	5.457E+11	7.19E+11	3.06E+11	1.57E+12
640	4.205E+11	7.46E+11	4.13E+11	1.58E+12
642	4.02E+11	7.54E+11	4.18E+11	1.57E+12
644	3.988E+11	7.58E+11	4.20E+11	1.58E+12
646	4.004E+11	7.55E+11	4.20E+11	1.58E+12
648	4.191E+11	7.57E+11	4.16E+11	1.59E+12
650	5.407E+11	7.26E+11	3.06E+11	1.57E+12
652	4.212E+11	7.57E+11	4.18E+11	1.59E+12
654	4.026E+11	7.57E+11	4.22E+11	1.58E+12
3655	4.017E+11	7.59E+11	4.21E+11	1.58E+12
657	4.03E+11	7.58E+11	4.22E+11	1.58E+12
659	4.197E+11	7.57E+11	4.15E+11	1.59E+12
661	5.361E+11	7.26E+11	3.05E+11	1.57E+12
663	4.161E+11	7.54E+11	4.17E+11	1.59E+12
665	3.996E+11	7.59E+11	4.19E+11	1.58E+12
667	3.969E+11	7.57E+11	4.18E+11	1.57E+12
669	4.035E+11	7.56E+11	4.21E+11	1.58E+12
671	4.235E+11	7.57E+11	4.17E+11	1.59E+12

673	5.448E+11	7.28E+11	3.07E+11	1.58E+12
3674	4.215E+11	7.55E+11	4.16E+11	1.59E+12
676	4.037E+11	7.59E+11	4.23E+11	1.59E+12
678	3.992E+11	7.60E+11	4.23E+11	1.58E+12
680	4.007E+11	7.57E+11	4.22E+11	1.58E+12
682	4.180E+11	7.54E+11	4.17E+11	1.59E+12
684	5.412E+11	7.27E+11	3.08E+11	1.58E+12
686	4.176E+11	7.55E+11	4.15E+11	1.59E+12
688	4.0E+11	7.58E+11	4.22E+11	1.58E+12
690	3.971E+11	7.58E+11	4.19E+11	1.57E+12
692	4.005E+11	7.56E+11	4.21E+11	1.58E+12
3693	4.177E+11	7.53E+11	4.14E+11	1.58E+12
695	5.421E+11	7.24E+11	3.05E+11	1.57E+12
697	4.220E+11	7.54E+11	4.15E+11	1.59E+12
699	4.071E+11	7.54E+11	4.21E+11	1.58E+12
701	4.074E+11	7.57E+11	4.19E+11	1.58E+12

APPENDIX II: Data from Stopping Range of Ion in Matter (SRIM) on Target Width

APPENDIX II **(**a**)**: SRIM Outputs\Cobalt in Cr-Fe- C-Mn- W- V-Ta.

Ion = Cobalt [27], Mass = 58.93 amu

Target Density = 7.9331E+00 g/cm3 = 8.3775E+22 atoms/cm3

Target Composition

Atom Name	Atom Number	Atomic Percent	Mass Percent
Cr	24	008.90	008.12
Fe	26	089.08	087.24
C	6	000.11	000.02
Mn	25	000.47	000.45
W	74	001.10	003.55
V	23	000.20	000.18
Ta	73	000.14	000.44

Ion Energy	dE/dx Elec.	dE/dx Nuclear	Projected Range	Longitudinal Straggling	Lateral Straggling
10.00 keV	1.169E-01	2.108E+00	51 A	30 A	22 A
11.00 keV	1.226E-01	2.156E+00	55 A	32 A	23 A
12.00 keV	1.281E-01	2.198E+00	58 A	34 A	24 A
13.00 keV	1.333E-01	2.236E+00	61 A	35 A	26 A
14.00 keV	1.383E-01	2.271E+00	65 A	37 A	27 A
15.00 keV	1.432E-01	2.302E+00	68 A	39 A	28 A
16.00 keV	1.479E-01	2.331E+00	71 A	40 A	29 A
17.00 keV	1.524E-01	2.357E+00	74 A	42 A	30 A
18.00 keV	1.568E-01	2.381E+00	78 A	44 A	32 A
20.00 keV	1.653E-01	2.423E+00	84 A	47 A	34 A
22.50 keV	1.753E-01	2.467E+00	92 A	50 A	36 A
25.00 keV	1.848E-01	2.504E+00	99 A	54 A	39 A
27.50 keV	1.938E-01	2.535E+00	107 A	58 A	42 A
30.00 keV	2.025E-01	2.560E+00	115 A	61 A	44 A
32.50 keV	2.107E-01	2.581E+00	122 A	65 A	47 A
35.00 keV	2.187E-01	2.599E+00	130 A	68 A	49 A
37.50 keV	2.264E-01	2.614E+00	137 A	72 A	52 A
40.00 keV	2.338E-01	2.626E+00	144 A	75 A	54 A
45.00 keV	2.480E-01	2.645E+00	159 A	82 A	59 A
50.00 keV	2.614E-01	2.657E+00	174 A	89 A	64 A
55.00 keV	2.741E-01	2.664E+00	189 A	96 A	68 A

60.00 keV	2.863E-01	2.667E+00	204 A	102 A	73 A
65.00 keV	2.980E-01	2.666E+00	218 A	109 A	77 A
70.00 keV	3.093E-01	2.663E+00	233 A	116 A	82 A
80.00 keV	3.306E-01	2.652E+00	263 A	129 A	91 A
90.00 keV	3.507E-01	2.635E+00	293 A	142 A	99 A
100.00 keV	3.696E-01	2.614E+00	323 A	154 A	108 A
110.00 keV	3.877E-01	2.591E+00	354 A	167 A	117 A
120.00 keV	4.098E-01	2.566E+00	384 A	180 A	125 A
130.00 keV	4.394E-01	2.540E+00	415 A	193 A	134 A
140.00 keV	4.575E-01	2.514E+00	446 A	205 A	142 A
150.00 keV	4.687E-01	2.487E+00	478 A	218 A	151 A
160.00 keV	4.762E-01	2.460E+00	509 A	231 A	160 A
170.00 keV	4.828E-01	2.433E+00	541 A	244 A	168 A
180.00 keV	4.905E-01	2.406E+00	574 A	256 A	177 A
200.00 keV	5.115E-01	2.353E+00	640 A	282 A	194 A
225.00 keV	5.456E-01	2.290E+00	723 A	314 A	215 A
250.00 keV	5.838E-01	2.229E+00	808 A	346 A	237 A
275.00 keV	6.243E-01	2.171E+00	895 A	377 A	260 A
300.00 keV	6.665E-01	2.116E+00	982 A	408 A	282 A
325.00 keV	7.102E-01	2.065E+00	1070 A	439 A	305 A
350.00 keV	7.549E-01	2.015E+00	1158 A	469 A	327 A
375.00 keV	8.003E-01	1.969E+00	1247 A	499 A	350 A
400.00 keV	8.460E-01	1.924E+00	1337 A	528 A	373 A
450.00 keV	9.370E-01	1.842E+00	1516 A	585 A	419 A
500.00 keV	1.026E+00	1.768E+00	1696 A	640 A	465 A
550.00 keV	1.111E+00	1.700E+00	1877 A	693 A	510 A
600.00 keV	1.193E+00	1.639E+00	2057 A	745 A	555 A
650.00 keV	1.271E+00	1.582E+00	2238 A	794 A	600 A
700.00 keV	1.346E+00	1.530E+00	2417 A	842 A	644 A
800.00 keV	1.484E+00	1.436E+00	2776 A	934 A	729 A
900.00 keV	1.611E+00	1.356E+00	3133 A	1021 A	813 A
1.00 MeV	1.730E+00	1.285E+00	3488 A	1102 A	893 A
1.10 MeV	1.842E+00	1.222E+00	3839 A	1179 A	971 A
1.20 MeV	1.950E+00	1.166E+00	4188 A	1251 A	1046 A
1.30 MeV	2.055E+00	1.116E+00	4532 A	1320 A	1119 A
1.40 MeV	2.157E+00	1.071E+00	4873 A	1385 A	1190 A
1.50 MeV	2.259E+00	1.030E+00	5210 A	1447 A	1258 A
1.60 MeV	2.360E+00	9.919E-01	5542 A	1505 A	1324 A
1.70 MeV	2.462E+00	9.572E-01	5869 A	1561 A	1388 A
1.80 MeV	2.563E+00	9.253E-01	6192 A	1613 A	1449 A
2.00 MeV	2.768E+00	8.683E-01	6821 A	1711 A	1566 A
2.25 MeV	3.028E+00	8.076E-01	7577 A	1819 A	1702 A
2.50 MeV	3.292E+00	7.558E-01	8300 A	1915 A	1825 A
2.75 MeV	3.561E+00	7.111E-01	8989 A	1998 A	1939 A
3.00 MeV	3.834E+00	6.721E-01	9647 A	2072 A	2042 A
3.25 MeV	4.109E+00	6.377E-01	1.03 um	2138 A	2137 A
3.50 MeV	4.385E+00	6.071E-01	1.09 um	2196 A	2224 A

3.75 MeV	4.661E+00	5.796E-01	1.14 um	2248 A	2304 A
4.00 MeV	4.937E+00	5.549E-01	1.20 um	2295 A	2378 A
4.50 MeV	5.483E+00	5.119E-01	1.30 um	2377 A	2509 A
5.00 MeV	6.019E+00	4.758E-01	1.40 um	2444 A	2622 A
5.50 MeV	6.540E+00	4.450E-01	1.49 um	2501 A	2721 A
6.00 MeV	7.045E+00	4.183E-01	1.57 um	2549 A	2807 A
6.50 MeV	7.533E+00	3.951E-01	1.65 um	2590 A	2884 A
7.00 MeV	8.003E+00	3.745E-01	1.72 um	2626 A	2952 A
8.00 MeV	8.888E+00	3.398E-01	1.86 um	2689 A	3069 A
9.00 MeV	9.703E+00	3.116E-01	1.99 um	2739 A	3167 A
10.00 MeV	**1.045E+01**	**2.881E-01**	**2.11 um**	**2781 A**	**3249 A**

APPENDIX II (b): SRIM Outputs\He in Zr-Sn-Fe-Cr-O.

Ion = Helium [2], Mass = 4.003 amu

Target Density = 6.4980E+00 g/cm3 = 4.2824E+22 atoms/cm3

Atom Name	Atom Number	Atomic Percent	Mass Percent
Zr	40	097.97	097.80
Sn	50	001.50	001.95
Fe	26	000.24	000.15
Cr	24	000.13	000.07
O	8	000.16	000.03

Ion Energy	dE/dx Elec.	dE/dx Nuclear	Projected Range	Longitudinal Straggling	Lateral Straggling
10.00 keV	1.103E-01	1.643E-02	506 A	505 A	389 A
11.00 keV	1.164E-01	1.606E-02	554 A	536 A	415 A
12.00 keV	1.224E-01	1.570E-02	602 A	566 A	440 A
13.00 keV	1.281E-01	1.536E-02	650 A	595 A	465 A
14.00 keV	1.337E-01	1.503E-02	697 A	622 A	488 A
15.00 keV	1.391E-01	1.472E-02	744 A	649 A	511 A
16.00 keV	1.444E-01	1.442E-02	791 A	674 A	533 A
17.00 keV	1.495E-01	1.413E-02	837 A	698 A	554 A
18.00 keV	1.545E-01	1.386E-02	884 A	722 A	575 A
20.00 keV	1.641E-01	1.334E-02	976 A	766 A	614 A
22.50 keV	1.756E-01	1.276E-02	1089 A	817 A	661 A
25.00 keV	1.866E-01	1.223E-02	1201 A	864 A	705 A

27.50 keV	1.971E-01	1.175E-02	1310 A	908 A	747 A
30.00 keV	2.073E-01	1.131E-02	1419 A	949 A	786 A
32.50 keV	2.170E-01	1.091E-02	1525 A	987 A	824 A
35.00 keV	2.264E-01	1.055E-02	1630 A	1022 A	859 A
37.50 keV	2.356E-01	1.021E-02	1733 A	1056 A	893 A
40.00 keV	2.445E-01	9.892E-03	1835 A	1088 A	926 A
45.00 keV	2.615E-01	9.326E-03	2034 A	1145 A	987 A
50.00 keV	2.777E-01	8.831E-03	2228 A	1198 A	1043A
55.00 keV	2.932E-01	8.394E-03	2417 A	1245 A	1096A
60.00 keV	3.080E-01	8.005E-03	2601 A	1288A	1144A
65.00 keV	3.222E-01	7.656E-03	2780 A	1328 A	1190A
70.00 keV	3.359E-01	7.341E-03	2955 A	1364A	1233A
80.00 keV	3.620E-01	6.793E-03	3294 A	1429A	1313A
90.00 keV	3.864E-01	6.332E-03	3619 A	1486A	1384A
100.00 keV	4.093E-01	5.938E-03	3931 A	1536A	1448A
110.00 keV	4.310E-01	5.597E-03	4233 A	1580A	1508A
120.00 keV	4.516E-01	5.298E-03	4525 A	1620A	1562A
130.00 keV	4.711E-01	5.033E-03	4808 A	1656A	1613A
140.00 keV	4.897E-01	4.797E-03	5083 A	1689A	1660A
150.00 keV	5.074E-01	4.585E-03	5350 A	1719A	1704A
160.00 keV	5.243E-01	4.394E-03	5611 A	1746A	1745A
170.00 keV	5.404E-01	4.219E-03	5867 A	1772A	1784A
180.00 keV	5.558E-01	4.060E-03	6116 A	1796A	1821A
200.00 keV	5.846E-01	3.779E-03	6600 A	1839A	1889A
225.00 keV	6.172E-01	3.484E-03	7181 A	1887A	1966A
250.00 keV	6.463E-01	3.237E-03	7740 A	1928A	2035A
275.00 keV	6.725E-01	3.026E-03	8279 A	1965A	2097A
300.00 keV	6.959E-01	2.844E-03	8803 A	1997A	2155A
325.00 keV	7.168E-01	2.685E-03	9313 A	2027A	2209A
350.00 keV	7.355E-01	2.545E-03	9812 A	2054A	2259A
375.00 keV	7.520E-01	2.420E-03	1.03 um	2079A	2306A
400.00 keV	7.667E-01	2.308E-03	1.08 um	2103A	2350A
450.00 keV	7.909E-01	2.115E-03	1.17 um	2146A	2432A
500.00 keV	8.092E-01	1.955E-03	1.26 um	2186A	2508A
550.00 keV	8.224E-01	1.820E-03	1.36 um	2221A	2578A
600.00 keV	8.315E-01	1.703E-03	1.45 um	2255A	2645A
650.00 keV	8.370E-01	1.603E-03	1.53 um	2285A	2707A
700.00 keV	8.395E-01	1.514E-03	1.62 um	2315A	2768A
800.00 keV	8.375E-01	1.366E-03	1.80 um	2375A	2883A
900.00 keV	8.285E-01	1.246E-03	1.98 um	2433A	2992A
1.00 MeV	8.149E-01	1.147E-03	2.17 um	2488A	3098A
1.10 MeV	7.981E-01	1.064E-03	2.35 um	2541A	3202A
1.20 MeV	7.795E-01	9.935E-04	2.55 um	2594A	3305A
1.30 MeV	7.599E-01	9.322E-04	2.74 um	2647A	3408A
1.40 MeV	7.399E-01	8.786E-04	2.94 um	2700A	3512A
1.50 MeV	7.198E-01	8.314E-04	3.15 um	2754A	3616A
1.60 MeV	7.001E-01	7.893E-04	3.37 um	2808A	3723A

1.70 MeV	6.808E-01	7.517E-04	3.59 um	2864A	3831A
1.80 MeV	6.622E-01	7.177E-04	3.81 um	2920A	3941A
2.00 MeV	6.270E-01	6.589E-04	4.29 um	3073A	4168A
2.25 MeV	5.873E-01	5.986E-04	4.91 um	3296A	4467A
2.50 MeV	5.522E-01	5.491E-04	5.58 um	3531A	4784A
2.75 MeV	5.213E-01	5.077E-04	6.29 um	3776A	5120A
3.00 MeV	4.940E-01	4.725E-04	7.04 um	4033A	5476A
3.25 MeV	4.700E-01	4.422E-04	7.83 um	4299A	5851A
3.50 MeV	4.488E-01	4.158E-04	8.67 um	4576A	6245A
3.75 MeV	4.299E-01	3.926E-04	9.53 um	4861A	6658A
4.00 MeV	4.130E-01	3.720E-04	10.44 um	5155A	7089A
4.50 MeV	3.843E-01	3.371E-04	12.36 um	6070A	8004A
5.00 MeV	3.608E-01	3.086E-04	14.41 um	6981A	8983A
5.50 MeV	3.412E-01	2.848E-04	16.59 um	7890A	1.00um
6.00 MeV	3.246E-01	2.646E-04	18.88 um	8801A	1.11 um
6.50 MeV	3.104E-01	2.473E-04	21.29 um	9714A	1.23 um
7.00 MeV	2.981E-01	2.322E-04	23.81 um	1.06 um	1.34 um
8.00 MeV	2.777E-01	2.073E-04	29.12 um	1.35 um	1.59 um
9.00 MeV	2.601E-01	1.875E-04	34.82 um	1.63 um	1.86 um
10.00 MeV	**2.436E-01**	**1.713E-04**	**40.90 um**	**1.89 um**	**2.13 um**